

# Electrical Excitation of Colloidally Synthesized Quantum Dots in Metal Oxide Structures

by

Vanessa Claire Wood

Submitted to the Department of Electrical Engineering  
in partial fulfillment of the requirements for the degree of

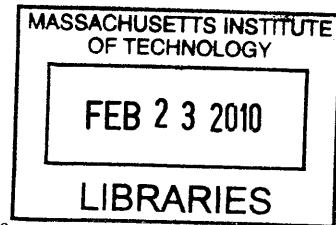
Doctor of Philosophy in Electrical Engineering

at the

MASSACHUSETTS INSTITUTE OF TECHNOLOGY


February 2010

© Massachusetts Institute of Technology 2010. All rights reserved.





**ARCHIVES**

Author .....

  
Department of Electrical Engineering

January 15, 2010

Certified by .....

   
Vladimir Bulović

Associate Professor of Electrical Engineering and Computer Science  
Thesis Supervisor

Accepted by .....

    
Professor Terry P. Orlando

Chair, Department Committee on Graduate Students



# Electrical Excitation of Colloidally Synthesized Quantum Dots in Metal Oxide Structures

by

Vanessa Claire Wood

Submitted to the Department of Electrical Engineering  
on January 15, 2010, in partial fulfillment of the  
requirements for the degree of  
Doctor of Philosophy in Electrical Engineering

## Abstract

This thesis develops methods for integrating colloidally synthesized quantum dots (QDs) and metal oxides in optoelectronic devices, presents three distinct light emitting devices (LEDs) with metal oxides surrounding a QD active layer, and uses these novel metal oxide based QD-LEDs to study mechanisms for electrical excitation of QDs. QD-LEDs have generated considerable interest for applications such as thin film displays with improved color saturation and white lighting with high color rendering index. This work demonstrates that air-stable metal oxides can be used to achieve QD-LEDs that have long shelf lives and operate at constant luminance in ambient conditions, unpackaged. Because metal oxides range from conductors to dielectrics, they can be used to develop a variety of different device architectures to explore mechanisms for electrical excitation of QDs. We report the first all-inorganic QD-LEDs with n- and p-type metal oxide charge transport layers and present design rules to enable systematic improvement of device efficiency. To shift away from direct charge injection as a means for electroluminescence (EL) in inorganic-based QD-LED structures, we develop a unipolar device architecture that presents the first evidence of field driven EL in QDs. To further explore this field driven excitation mechanism, we develop a structure that situates QDs between two insulating metal oxide layers. By eliminating the need for energy band alignment, these devices enable EL from QDs with emission peaks from 450 nm-1500 nm as well as from novel nanoparticles, such as phosphor doped-core/shell nanocrystals.

Thesis Supervisor: Vladimir Bulović

Title: Associate Professor of Electrical Engineering and Computer Science



## Acknowledgments

I am grateful to my advisor, Professor Vladimir Bulović, for making ONE Lab a place with the freedom and resources where I could develop as an independent scientist. I am indebted to many ONE Lab colleagues, in particular Dr. Matt Panzer, who has been a thoughtful collaborator, advocate, mentor, and friend. Polina Anikeeva, Alexi Arango, Scott Bradley, Jean-Michel Caruge, Gerry Chen, John Ho, Lee-Ann Kim, John Kymissis, Conor Madigan, Ivan Nausieda, and Jonathan Tischler: thank you for your help in lab, for great conversations, and for making me smile.

It is a pleasure to thank my thesis committee members, Professors Leslie Kolodziejski and Yet-Ming Chiang, for their time and encouragement, Professor Mounqi Bawendi for his scientific insights, and Professors Steven Lerman and Terry Orlando for their support and advice as I navigated the path to the Ph.D.

I acknowledge financial support from the MIT Society of Presidential Fellows, the National Defense Science and Engineering Fellowship, and the National Science Foundation Graduate Fellowship Program and thank Keith, Yulia, Sara, John, Andrew, Jonathan, Nicole, Jen, Duke, Polly, and Kate for their friendship during the Ph.D.

I should also like to thank my high school physics teacher, James Mooney, and those undergraduate science professors and research directors who inspired and encouraged me: Richard Chang, Veronique Boutou, Victor Henrich, and Rick Casten.

This thesis is dedicated to my parents who taught me to love learning and to my grandfather Pop who showed me what it means to be an engineer.



# Contents

<b>1</b>	<b>Introduction to QD-LEDs</b>	<b>25</b>
1.1	Thin-Film Light Emitting Devices and Solid State Lighting . . . . .	26
1.2	Quantum Dot LEDs . . . . .	27
<b>2</b>	<b>Colloidally Synthesized Quantum Dots</b>	<b>33</b>
2.1	Colloidal QD Synthesis . . . . .	37
2.2	QDs in an Electric Field . . . . .	42
2.3	Charge Transport in Colloidal QD Films . . . . .	46
2.4	Luminescence Quenching in Colloidal QDs . . . . .	47
<b>3</b>	<b>Metal Oxides</b>	<b>51</b>
3.1	Radio Frequency Sputter Deposition . . . . .	55
3.2	Amorphous Metal Oxides . . . . .	58
3.3	Electronic Transport in Metal Oxides . . . . .	61
3.4	Dielectric Properties of Metal Oxides . . . . .	63
<b>4</b>	<b>Characterization Techniques</b>	<b>65</b>
4.1	Thin Film Morphology . . . . .	65
4.1.1	Atomic Force Microscopy . . . . .	65
4.1.2	X-ray Diffraction . . . . .	67
4.2	Electronic Properties of Materials . . . . .	67
4.2.1	Film Conductivity . . . . .	67
4.2.2	Ultraviolet Photoelectron Spectroscopy . . . . .	69

4.3	QD-LED Characterization Techniques . . . . .	75
4.3.1	Photoluminescence Measurements . . . . .	75
4.3.2	DC Electroluminescence Characterization . . . . .	76
4.3.3	Luminance and Chromaticity Coordinates . . . . .	77
4.3.4	Combined Electroluminescence and Photoluminescence Measurements . . . . .	78
4.3.5	Time Resolved Electroluminescence . . . . .	79
<b>5</b>	<b>Diode QD-LED</b>	<b>81</b>
5.1	The first QD-LED using metal oxide based transport layers . . . . .	81
5.2	Demonstrating red, green, and blue emission . . . . .	91
5.3	Improving QD-LED efficiency . . . . .	92
<b>6</b>	<b>Unipolar QD-LEDs</b>	<b>99</b>
6.1	Design and Fabrication of Unipolar QD-LEDs . . . . .	100
6.2	Unipolar Device Operatation . . . . .	102
6.3	Investigation of Device Operating Mechanism . . . . .	109
6.4	Benefits of Unipolar Device . . . . .	118
<b>7</b>	<b>QD Thin Film Electroluminescence</b>	<b>121</b>
7.1	Field-Driven Electroluminescence from QDs . . . . .	123
7.1.1	Thin Film Electroluminescence . . . . .	123
7.1.2	Mixed QD and Insulating Polymer . . . . .	128
7.1.3	Electrical and Optical Characterization . . . . .	129
7.2	Electrical Excitation of Phosphor-doped Nanocrystals . . . . .	133
7.2.1	Synthesis of Mn-doped Nanocrystals of EL . . . . .	134
7.2.2	Device Structure . . . . .	136
7.3	Inkjet Printing of Quantum Dot Films . . . . .	142
7.3.1	QD Ink Solutions and Printing Technique . . . . .	143
7.3.2	Optical Downconversion as Proof of Concept Devices . . . . .	148
7.3.3	Enhanced Device Luminescence using Metal Oxide Thin Films . . . . .	152



7.3.4	Electrical Excitation of Inkjet Printed Active Layers . . . . .	155
<b>8</b>	<b>Conclusion</b>	<b>157</b>
8.1	Thesis Summary . . . . .	157
8.2	Future Directions . . . . .	159



# List of Figures

1-1	Schematic of a QD-LED that uses a monolayer of colloidal quantum dots sandwiched between an organic electron transport layer (ETL) and an organic hole transport layer (HTL). Photographs and spectra of the electroluminescence from five QD-LEDs that have different color emitting QDs [1]. . . . .	29
1-2	Microcontact printing of QDs enables side-by-side deposition of micron-scale red, green, and blue pixels (bottom left), or mixing of red, green, and blue QDs within a single monolayer to create a single white light emitting active layer (top left). CIE chromaticity diagram showing the spectral purity of QDs enables a color gamut larger than the HDTV standard. . . . .	31
2-1	Absorption spectra for a series of CdSe samples ranging in size from 2 nm to 12 nm in diameter. . . . .	37
2-2	The basic steps involved in a colloidal QD synthesis. . . . .	38
2-3	Schematic of the structures of ZnCdSe, CdSe/ZnS, ZnSe/CdSe/ZnS, and ZnCdS QDs and a photograph of their photoluminescence in solution. Photograph courtesy of J. Halpert. . . . .	39
2-4	a) A photograph of a vial of PbS/CdS QDs that emit in the infrared with a peak near 1500 nm. b) Photoluminescence spectra of three different PbS/CdS QD solutions. The red-side of the 1500 nm QD spectrum is clipped because of the limit in the InGaAs detector used to collect spectra. . . . .	42

2-5	Schematics of a) single QD spectrum, b) a fluorescence line narrowed ensemble QD spectrum, and c) a QD ensemble spectra. Panels b and c illustrate how the ensemble QD spectrum is a convolution of many single QD spectra that are slightly offset as a result of a finite size distribution in a given QD sample. . . . .	44
2-6	Schematic depiction Fröhlich coupling in QDs [2]. . . . .	44
2-7	Comparison of spectra for QDs under no applied electric field (black lines) and an applied electric field (red). Schematics represent a single QD spectrum (a), a fluorescence line narrowed ensemble QD spectrum (b), and an ensemble QD spectrum (c). These schematics illustrate why a QD ensemble under an applied field appears to be red-shifted and broadened. . . . .	45
2-8	Photoluminescence of single QDs on a) glass, b) $\text{WO}_3$ with a resistivity of $10 \Omega \cdot \text{cm}$ , and c) $\text{WO}_3$ with a resistivity of $0.2 \Omega \cdot \text{cm}$ . The concentration of QDs in the illuminated area is equivalent for each sample, and the excitation source is the same for each sample. . . . .	49
3-1	Photograph of growth system in the Laboratory for Organic and Nanostructured Electronics at MIT where this work was performed. . . . .	55
3-2	Cross sectional view of electrode assembly for RF sputtering. . . . .	57
3-3	Disordered Kronig Penny model (a) potential and (b) resulting wavefunction. . . . .	58
3-4	Schematic of the density of states for an amorphous solid semiconductor at different energies. . . . .	59
3-5	Localized electron hopping model [3]. . . . .	62
4-1	a) AFM height image of PbS/CdS QD spin cast on $\text{Al}_2\text{O}_3$ from chloroform. b) AFM phase image of PbS/CdS QD spin cast on $\text{Al}_2\text{O}_3$ from chloroform. c) AFM phase image of PbS/CdS QD spin cast on $\text{Al}_2\text{O}_3$ from chlorobenzene. . . . .	66
4-2	Mask design for Van der Pauw measurements. . . . .	68

4-3	Photograph of Omicron NanoTech combined deposition and analysis system used to obtain the ultraviolet photoelectron spectroscopy results presented here. . . . .	71
4-4	Example of data obtained from ultraviolet photoelectron spectroscopy.	71
4-5	Plot of the He I ultraviolet photoelectron spectroscopy (UPS) measurements on NiO, WO <sub>3</sub> , ZTO, and ZnS thin films. . . . .	72
4-6	Process flow for preparing a QD film for UPS measurements. Atomic force microscopy (AFM) phase image of the edge of a ZnCdSe QD film stamped onto an ultra-smooth template stripped Au surface. . . . .	73
4-7	Plot of the derivative of the He I UPS spectra for several QD samples. The first minimum of these curves (indicated by the dashed lines) corresponds to the ionization energy of the sample. . . . .	74
4-8	Valence and conduction band energies from UPS and optical absorption measurements. . . . .	75
4-9	Schematic of measurement to simultaneously measure the electroluminescent (EL) and photoluminescent (PL) response of the QD-LED. This setup is used to obtain PL quenching data as well as the effect of an electric field on the PL and EL spectra (See Section 6.3). . . . .	78
5-1	Schematic of the basic QD-LED structure. . . . .	82
5-2	AFM phase images measurements showing the QDs spin cast onto the NiO (a), 10 nm of ZnO sputter-deposited on the QD film (b), and 10 nm of ZTO sputter-deposited on the QD film (c). XRD scans of ZnO (d) and ZTO (e) showing that ZnO is polycrystalline while ZTO is amorphous. . . . .	85
5-3	Photoluminescence (PL) spectra before (solid line) and after (dotted line) deposition of a 120 nm thick ZTO layer onto ZnCdSe QDs on NiO.	86
5-4	The current density vs. voltage ( $J$ - $V$ ) log log plot for a QD-LED described in the text. Three different regimes of conduction are clearly visible. . . . .	87

5-5 a) Electroluminescence (EL) spectra of the QD-LED at 6 V (0.46 A/cm<sup>2</sup>) and 9 V (1.14 A/cm<sup>2</sup>) applied bias. (b) Plot of the QD-LED external quantum efficiency (EQE) measured from the front face of the device as a function of current density. A maximum EQE of 0.09 % and a luminance of 1500 Cd/m<sup>2</sup> is reached at 13.8 V, (2.33 A/cm<sup>2</sup>). The inset shows a photograph of a bright and uniform pixel at 6 V applied bias. Significant amount of additional light is guided through the glass substrate and emitted at the four substrate edges, as evident from the photograph. Presence of the edge-emitted light is not reflected in the stated EQE measurements. . . . . 88

5-6 Plot of the modulation in QD-LED electroluminescence (EL) intensity as a function of frequency. The half-power point of the curve corresponds to the -3 dB cutoff frequency of 1.2 MHz. . . . . 90

5-7 A band diagram determined from ultraviolet photoemission spectroscopy measurements and optical absorption measurements giving the approximate ionization energies and bandgap of the QD-LED materials. . . 91

5-8 Summary of the energy band values obtained from the UPS and band gap measurements. . . . . 92

5-9 Electroluminescence spectra of blue, green, and red-emitting QDs from metal-oxide based QD-LEDs. WO<sub>3</sub> replaced NiO as the hole injection layer to enable blue and green QD EL. The spectra are taken at 18 V, 15 V, and 12 V for the blue, green, and red, respectively. . . . . 93

5-10	a) Schematics of the NiO-QD-ZTO device structures with modified n-type transport layers. In Structures 2 and 4, a 10 nm thick layer of ZnO is sputtered on top of the spin cast QD film. Structures 3 and 4 contain a 15 nm thick layer of ZnS within the ZTO. b) Current density vs. voltage ( $J$ - $V$ ) characteristics of the four structures. The addition of the ZnO layer (dashed vs. solid lines) does not increase the turn on voltage of the device. The inset plot of the external quantum efficiency (EQE) as a function of the current density shows systematic improvement across the four structures. The EQE characteristics for each structure are an average of data from five sets of devices, with each of the four structures processed in parallel for a given set. . . .	94
5-11	a) Photoluminescence spectra of QDs excited with a $\lambda = 532$ nm laser. The film of QDs is spin cast on either a 40 nm thick layer of sputter deposited ZTO (dashed line) or 10 nm of ZnO on top of 40 nm of ZTO (solid line). The addition of 10 nm of insulating ZnO doubles the PL response of the QD film. b) Schematic band diagram for Structure 3 showing that ZnS acts as a barrier to electrons in the ZTO. . . . .	96
6-1	Cross-sectional schematics of the device architectures described in this letter. Structure 1 consists of colloidal QDs sandwiched between two layers of ZTO. Structures 2A, 2B, and 2C incorporate at least one layer of ZnS within the ZTO layers, located 15 nm away from the QD film. The ZnS can be positioned in the ZTO above the QDs (Structure 2A), below the QDs (Structure 2B), or on either side of the QDs (Structure 2C). . . . .	100
6-2	Topographical (left) and phase (right) atomic force microscopy (AFM) images of red CdSe/ZnS QDs spin coated onto 40 nm of ZTO on ITO show the type of complete and ordered film necessary for efficient device operation. . . . .	102

- 6-3 a) A cross sectional scanning electron microscope (SEM) image of device Structure 2A, which is grown on a Si substrate to facilitate sample cleaving. The sample is cleaved across the top contact using a diamond blade. The cleaved surface is cross-section polished for 5 hours and SEM images are taken with an electron energy of 10 KeV and a working distance of 3 mm. The SEM reveals continuous ceramic layers and a 50 nm thick QD region. b) The optimized unipolar device structure contains a layer of ZnO on either side of the QD layer. . . . . 103
- 6-4 Plot of Structure 2A device absorption versus wavelength. The inset photograph shows the device on top of text to demonstrate the transparency of the wideband gap ceramics and thin QD layer. . . . . 103
- 6-5 a) Photograph of device Structure 2A operating at 18 V, demonstrating the uniformity of pixel illumination as well as device transparency. b) Current density vs. voltage characteristics for device Structures 1 (black line), 2A (red line), 2B (purple line), and 2C (blue line) under forward and reverse DC bias conditions. The inset schematic indicates the bias convention. c) External quantum efficiency (EQE) versus the absolute value of current density for device Structures 1 and 2A. The dotted red lines in panels b and c show the current density and EQE measurements for the optimized Structure 2A device. d) Luminance (solid symbols) and luminous efficiency (open symbols) for device Structure 1 (black) and Structure 2A (red). Data for the optimized Structure 2A is shown in red with circle symbols. . . . . 105



6-6	a) Spectra corresponding to photoluminescence (PL) of red and green QDs in a dilute solution (dashed black lines), PL of QDs in the device structure (dashed red and green lines), and electroluminescence (EL) from red and green QDs in device Structure 1 at 14 V bias (solid red and green lines). The PL of the concentrated solution of red QDs is shown by a solid black line. b) A plot of the shift in peak position of the PL spectra of device Structures 1 (squares), 2A (triangles), and 2C (diamonds) as a function of voltage applied across the device. For this measurement, biases below the turn-on voltage of the device are used in order to measure only the PL spectral response to electric field and not the combined EL and PL behavior. . . . .	106
6-7	Schematic of the zero-bias band diagram for the possible unipolar device structures shows that the ZnS layer(s) and the ZnS shells on the QDs act as electron blocking layers. . . . .	107
6-8	Schematic band diagrams of device Structures 1 (a) and 2A (b) under forward bias conditions. We note that a larger applied bias is needed to generate the same voltage drop across the QD film in Structure 2A as in Structure 1. . . . .	108
6-9	Device current (a) and external quantum efficiency (EQE) (b) for five different Structure 1 devices. The voltage pulse applied to generate the measured current and EQE is shown in panel a. . . . .	111
6-10	Photoluminescent (PL) response of QD film as a function of applied voltage across devices with 20 nm thick (circles) and 40 nm thick (squares) of ZTO. PL signal is normalized to the response with no applied voltage.	112

6-11 a) Plot of normalized photoluminescence (PL) as a function of applied voltage in forward bias for device Structures 1 (squares), 2A (upward pointing triangles), 2B (downward pointing triangles) and 2C (diamonds). In the case of device Structures 2A and 2C in forward bias, electrons injected into the ZTO encounter a ZnS layer prior to the QD film. In contrast, electrons in the ZTO in Structure 1 and 2B do not encounter a ZnS layer and accumulate at the QD film. Consequently, device Structures 2A and 2C show less PL quenching with increasing voltage than Structures 1 and 2B, indicating that accumulation of electrons at the ZnS layer instead of at the QD film reduces charging of the QD layer. The trend in PL quenching of device Structures 1 and 2B are the same but offset in voltage because of the presence of the insulating ZnS layer in Structure 2B. This plot illustrates that electron accumulation at the QD film, not electric field, determines the amount of QD charging luminescence quenching. . . . . 114

6-12 a) Electroluminescent intensity as a function of time for Structure 1 (squares) and Structure 2A (triangles) under forward and reverse bias conditions. The bias voltages are chosen such that both devices exhibit the same intensity EL after 5 s. b) Plot of the time constants associated with the EL at different voltages. . . . . 115

6-13 Plot of the electroluminescent response as a function of frequency of the applied bias. . . . . 116

6-14 a) Plot of the midpoints of the red and blue sides and peak position of the combined EL and PL spectra (open symbols) and EL spectra only (solid symbols). Data for Structures 1 (squares), 2A (upward pointing triangles), 2B (downward pointing triangles), and 2C (diamonds) are shown. b) EL spectra of device Structure 2A at 17V, 18V, and 19V. 117

- 6-15 a) Plot of luminosity (top, left axis) and voltage (bottom, right axis) as a function of time for device Structure 2A operated in forward bias at a constant current of  $30 \text{ mA/cm}^2$ . The device was unpackaged and operated in air. Voltage and luminescence data were recorded every 5 s for 20 consecutive hours and then binned and averaged into one minute intervals. b) Scatter plot of luminosity versus voltage using all of the data in panel a shows that despite fluctuations in the voltage and luminosity over time, the luminosity at a given voltage is constant, indicating that these fluctuations do not correspond to changes in the device performance with time. For example, the voltage and luminosity at 1 hour 50 minutes ( $\alpha$ ) and 10 hours ( $\beta$ ) are comparable. . . . . 120
- 7-1 a) Schematic band diagram of an AC TFEL device showing some of the key operating principles. Electrons trapped at interfaces between the insulating and phosphor layers are injected into the conduction band of the phosphor, where they are accelerated by the field (1). These high energy electrons can excite the luminescent dopant centers in the phosphor layer via impact excitation and ionization mechanisms. The luminescent center can then radiatively or non-radiatively relax (2). The electrons are transported to the other interface where they become trapped (3). b) Photograph of a Planar Inc. transparent AC TFEL display. . . . . 122
- 7-2 a) Schematic of a TFEL device incorporating a QD layer. b) Photograph of a completed TFEL structure (containing red-emitting QDs) that uses ITO for both the top and bottom contacts. The device is placed on top of a sheet of paper with black lettering to highlight the transparency of the device. c) Photograph of completed device structures containing red, green, and blue QD active layers under UV illumination. . . . . 124

7-3	a) Photoluminescence (dashed lines) and electroluminescence (solid lines) spectra for blue, green, red, and infrared emitting QDs in a TFEL device structure. b) Photographs of the red, green, and blue devices operating at 30 kHz and 110 $V_{p-p}$ , 130 $V_{p-p}$ , and 145 $V_{p-p}$ , respectively.	126
7-4	Schematic band diagram for TFEL device under 80 $V_{p-p}$ applied bias.	127
7-5	Plot of the light output as a function of the voltage drop across the QD layer. . . . .	128
7-6	Fluorescence microscope images of tested and untested pads in TFEL devices with a QD active layer (a) and with a QD-PIB composite active layer (b). The tested pad in panel a exhibits quenched QD luminescence, which can be attributed to loss of QD ligands. . . . .	129
7-7	Schematic of test setup used to measure the current through the QD layer as a function of time. . . . .	130
7-8	Plots of the voltage across the device, the current through the QD layer, and the electroluminescence of the device recorded by the photodetector for applied bias frequencies of a) 1 kHz, b) 10 kHz, and c) 100 kHz. .	132
7-9	Schematic of a ZnSe/ZnS:Mn/ZnS nanocrystal. . . . .	134
7-10	a) The absorption (black line) and photoluminescence (orange line) spectra of the ZnSe/ZnS:Mn/ZnS nanocrystals in solution show a large (235 nm) Stokes shift. b) Photographs of a vial of ZnSe/ZnS:Mn/ZnS nanocrystals in chloroform under room lighting (left) and under UV illumination (right) provide visual confirmation of the spectra shown in panel a, which indicate that these orange-emitting nanocrystals exhibit no absorption in the visible wavelength regime. . . . .	135
7-11	a) A schematic of the doped nanocrystal-based AC-TFEL device structure. Atomic force microscopy topographic and phase images show: b) the first layer of nanocrystals spin cast on ZnS, and c) a subsequent layer of ZnS sputtered on top of the nanocrystals. Comparison of the phase images in panels b and c shows that the nanocrystals are completely covered by the 12 nm layer of ZnS. . . . .	137

7-12 Plot of the electroluminescent (EL) intensity versus the number of layers of ZnS in the device structure. We find that for a given bias condition (here,  $100 V_{p-p}$  at 30 kHz), devices with four layers of ZnS (and three 30 nm thick layers of nanocrystals) give the largest EL response. 138

7-13 a) A photograph of a  $12.7 \text{ mm} \times 12.7 \text{ mm}$  glass substrate containing ten  $1 \text{ mm} \times 2 \text{ mm}$  AC-TFEL devices, with no bias applied. The substrate is pictured on top of printed text to demonstrate the transparency of the AC-TFEL device architecture. The inset shows the uniformity of pixel illumination (in the dark) with the device operating at  $170 V_{p-p}$  and 30 kHz. b) Plots of the EL response as a function of drive voltage and frequency. Values are normalized with respect to the EL response at  $170 V_{p-p}$  and 30 kHz. . . . . 140

7-14 The EL spectra for devices with  $\text{Al}_2\text{O}_3$  and  $\text{HfO}_2$  insulating layers are presented by the solid and dashed orange curves, respectively. The bias conditions are  $170 V_{p-p}$  and 30 kHz. A photoluminescence (PL) spectrum of an incomplete device structure ( $\text{ITO}/\text{Al}_2\text{O}_3/\text{ZnS}/30 \text{ nm}$  nanocrystals) (solid black curve) matches solution PL spectrum of the nanocrystals in chloroform (solid gray curve). The PL spectrum of a more complete device (consisting of  $\text{ITO}/\text{Al}_2\text{O}_3/\text{ZnS}/30 \text{ nm}$  nanocrystals/ $\text{ZnS}$ ) in which ZnS has been sputtered onto the nanocrystals is shown with the dashed black line. . . . . 141

7-15 a) Photograph of the Hewlett Packard Thermal Inkjet Pico-fluidic dispensing System (TIPS) printhead. Courtesy of HP. b) Photograph of print station setup including the precision movable stage under the fixed TIPS system. . . . . 143

7-16 QD and polyisobutylene (PIB) ink solutions under UV illumination. . 144

7-17 Fluorescence microscope images of an inkjet printed line using solutions of (a) QDs in hexane/octane (9:1) and (b) QDs and PIB in hexane/octane (9:1). Identical inkjet printing settings were used for both solutions. . . . . 145

7-18 Photographs (top) and optical microscope images (bottom) of printed QD-PIB composites from inks with hexane to octane ratios of (a) 1 to 9 and (b) 1 to 1, and from an ink with a 9 to 1 hexane/octane ratio (c) without and (d) with substrate heating. All patterns were deposited with identical printhead settings. . . . . 146

7-19 a) 1 mm profilometry scan of the edge of a green rectangular pixel measuring  $3\text{ mm} \times 5\text{ mm}$  demonstrates the edge definition and top surface uniformity of an average pixel. The inset is a photograph of a multicolor QD-PIB pattern inkjet printed on  $25.4\text{ mm} \times 25.4\text{ mm}$  indium tin oxide (ITO) coated glass and illuminated with  $\lambda = 365\text{ nm}$  light. b) Luminescence microscope photograph of a series of parallel lines printed to be  $100\text{ m}$  wide at  $250\text{ m}$  pitch demonstrates the feasibility of printing high-resolution patterns. c) Photograph of the MIT seal printed in QDs. . . . . 147

7-20 Absorption and photoluminescence spectra of spin coated thin films of red and green quantum dots (QDs) and the electroluminescence spectrum of the blue phosphor paste powered by  $50\text{ kHz}$  AC excitation demonstrate the spectral overlaps needed to achieve optical down-conversion of phosphor emission to QD film luminescence. The inset schematic depicts the cross section of an AC powder EL device structure with QD-PIB pixels. . . . . 149

- 7-21 a, b) Electroluminescence spectra and photographs of red, green, and blue 80 mm<sup>2</sup> pixels. c) Device CIE coordinates plotted on a chromaticity diagram show that the optical downconversion devices subtend a color triangle (solid black line) comparable to that of the International Telecommunication Union HDTV standard (dotted black line). The dotted white lines indicate two examples of possible ranges of color that can be obtained by simply varying the thickness of the printed QD-PIB layer made with a single QD ink solution. The numbers written next to the white data points indicate the number of layers of the QD-PIB ink used to achieve the designated color. . . . . 151
- 7-22 a) Photograph of a completed device on a flexible substrate under  $\lambda = 365$  nm wavelength illumination. The ruler pattern printed with red QD-PIB ink is to scale. b) Photographs of the photoluminescence devices with three, six, and nine layers of inkjet printed QD-PIB, under  $\lambda = 365$  nm wavelength illumination, provide a visual indication of the color purity. The plot shows luminance versus applied rms voltage for a blue (ZnS:Cu phosphor only) pixel, as well as the red and green pixels with three, six, and nine layers of QD-PIB. . . . . 152
- 7-23 a) Data are taken from devices with 50 nm thick ZnO layers and variable thickness Al<sub>2</sub>O<sub>3</sub> transparent metal oxide layers, positioned as shown with the inset schematic. The plot shows measured (data points) and modeled (black line) device luminance as a function of Al<sub>2</sub>O<sub>3</sub> layer thickness. The data follow the oscillatory trend predicted by the model described in the text. b) The electroluminescence spectra for devices with and without a 20 nm ZnO layer indicate that the ZnO contributes to waveguiding of the phosphor electroluminescence in the plane of the substrate which facilitates an improved color purity of the emission. The inset schematic shows the placement of the ZnO layer in the device structure. . . . . 154

7-24 a) Schematic diagram of a thin film EL device using an inkjet printed  
QD-polymer active layer. b) A photograph of a TFEL device biased  
at  $130 V_{p-p}$  and 30 kHz. . . . . 156



# Chapter 1

## Introduction to QD-LEDs

The goals of this thesis are three-fold: to investigate methods for integrating colloidally synthesized quantum dots (QDs) and metal oxides; to develop QD light emitting devices (QD-LEDs) with metal oxide-based structures; and to use these QD-LEDs to study the electrical excitation of QDs. In addition to having immediate application in improving display technology and solid state lighting, these metal oxide-based QD-LEDs also provide a platform for studying physical processes in QDs, which is necessary to enable systematic design of QD optoelectronic devices.

Chapter 1 outlines the main challenges facing LEDs in displays and solid state lighting, summarizes the state of the art in QD-LED technology, and outlines the benefits that QDs offer for other optoelectronic devices. Chapters 2 and 3 introduce the QD and metal oxide material systems and their physical properties relevant to this work. Chapter 4 presents the tools and techniques needed to study the individual materials and characterize completed QD-LEDs. Chapters 5, 6, and 7 present three novel metal oxide based QD-LED architectures, as well as their benefits for display technology and for understanding electrical excitation in QDs.

## 1.1 Thin-Film Light Emitting Devices and Solid State Lighting

The International Energy Agency reports that in 2005, 240 billion dollars were spent on electricity for lighting in the United States alone. Grid-based lighting accounts for 19 % of global electricity consumption, and the CO<sub>2</sub> emissions from this electricity production are equivalent to that of 70 % of automobiles worldwide. It is predicted that the global demand for lighting will increase 80 % by 2030, putting immense strain on global resources should new, more efficient technologies not find wide-spread acceptance. Currently, approximately 50 % of residential lighting in the United States relies on inefficient incandescent lamps that convert only 5 % of the energy they consume into useful light. The remaining lighting needs are largely satisfied by fluorescent fixtures, which while more efficient, raise environmental concerns during manufacture and upon disposal due to the mercury vapor they contain [4]. These economic and environmental considerations make a clear case for the need for development and wide-scale implementation of energy efficient lighting technologies.

Solid state lighting solutions in the form of white LEDs (WLEDs) have emerged as attractive alternatives [4]. A major challenge in developing white light sources is that red, green, and blue-emitting (RGB) thin film semiconductors comprise different material systems and can have luminous efficiencies that differ by an order of magnitude. An ideal white light source would have a color rendering index of 100, which means that it illuminates colors in the same way as sunlight. Multichip red, green, and blue WLEDs provide relatively good color rendering, but are high cost due to the driving circuits that must continuously balance the different color emitters that age at different rates [5]. Lower cost solutions such as single chip InGaN WLEDs suffer from poor color rendering because their emission is composed of only yellow phosphor and blue InGaN [5]. Organic LEDs (OLEDs) enable efficient, flat panel white lighting with color rendering near 90 [6]. Because they are composed of amorphous thin films, OLEDs simplify to some degree the manufacturing challenges presented by single crystal, inorganic semiconductors; however, the sensitivity of the organic

materials to atmospheric oxygen and water vapor and the possibility of self-induced photo-degradation raise questions about the possibility for long lifetimes in OLED panel lighting.

Many of the challenges in the development of WLEDs are analogous to those facing the creation of more energy efficient displays since both applications necessitate high brightness and multicolor emitters. Displays further require high resolution, high color purity pixels that are individually addressable. OLEDs are seen as an attractive technology for flat panel displays because of their low energy consumption and wide-viewing angle in comparison to back-lit liquid crystal displays (LCDs). However, finding low cost methods for side-by-side deposition of red, green, and blue organic emitters remains an active area of current research and development [7, 8].

## 1.2 Quantum Dot LEDs

Colloidally synthesized nanoparticles, such as quantum dots (QDs), offer a possible solution to some of the challenges currently facing the design and manufacture of LEDs for lighting and display applications. The electronic structure of colloidal QDs, which range from 3 nm to 12 nm in diameter, is dominated by quantum size effects [9]. This gives colloidal QDs their signature narrow band emission that can be spectrally positioned by controlling the nanocrystal size during synthesis. CdSe QDs of different sizes provide emission from the blue through the red, while QDs made of a smaller band gap material such as PbSe, PbS, or CdTe offer spectral tunability in the near-infrared. These inorganic nanocrystals are more robust than organic materials and dyes. Because colloidal nanoparticles are synthesized from organometallic precursors and retain a passivating layer of organic ligands, they are also solution processable, which facilitates a variety of low cost, large area deposition techniques such as spin casting, inkjet printing, and microcontact printing as well as integration with flexible substrates.

The first QD-LEDs incorporated CdSe QDs and polymers between a transparent indium tin oxide (ITO) anode and a metal cathode. A layered CdSe QD and p-

paraphenylene vinylene (PPV) architecture was used in [10], and QDs were dispersed in polyvinylcarbazole and an oxadiazole derivative in [11]. Both these initial efforts yielded QD-LEDs with low turn on voltages and substantial electroluminescence (EL) from the polymers as well as the QDs. In 2002, S. Coe and colleagues developed a phase separation technique that enabled formation of a close-packed monolayer of QDs on a small molecule organic hole transport layer (N,N'-diphenyl-N,N'-bis(3-methylphenyl)-N,N'-bis(phenyl)benzidine (TPD)) from a single spin cast step [12]. The device was completed with a thermally evaporated electron transporting organic molecule layer and exhibited minimal emission from the organic layers, a low turn on voltage, and an external quantum efficiency (EQE) of 0.52%. Since then, QD-LEDs incorporating a monolayer of QDs between an organic electron transport layer (ETL) and an organic hole transport layer (HTL), as shown schematically in Figure 1-1, have continuously held the record for QD-LED efficiency with numerous studies devoted to improving their performance and understanding the mechanism behind their operation.

Experimental data and numerical modeling has confirmed that the high efficiency of these organic-based QD-LEDs can be attributed to the concomitant excitation of the luminescent QD film via Förster energy transfer and direct charge injection [13]. In the former method for generating QD electroluminescence, an exciton forms on the wide band gap organic thin film, non-radiatively energy transfers to a QD, and radiatively recombines. In the latter, an electron and a hole are injected into the QD, form an exciton, and radiatively recombine. Careful material selection to optimize these two excitation methods enabled electroluminescence from blue, cyan, green, orange, and red QD monolayers sandwiched between the same two organic layers (hole-transporting spiro-N,N'-diphenyl-N,N'-bis(3-methylphenyl)-(1,1'-biphenyl)-4,4'-diamine (spiroTPD) and electron-transporting 2,2',2''-(1,3,5-benzenetriyl)-tris(L-phenyl-l-H-benzimidazole) (TPBi)) [1]. The peak EQE for these devices (shown in Figure 1-1) is 2.7% in the red, 2.6% in the green, and 0.4% in the blue. At the Materials Research Society Fall Meeting in December 2008, QD Vision, Inc. reported a red QD-LED with an EQE of 7.5% [14], which is competitive with the efficiency of

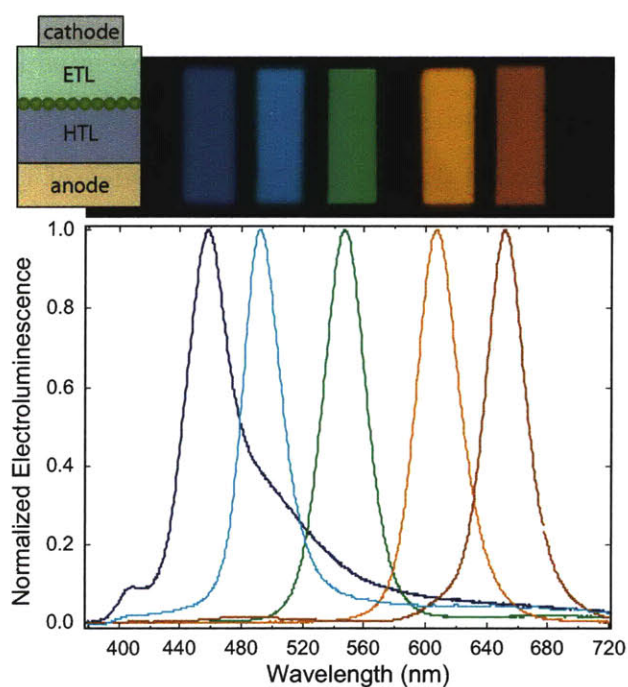


Figure 1-1: Schematic of a QD-LED that uses a monolayer of colloidal quantum dots sandwiched between an organic electron transport layer (ETL) and an organic hole transport layer (HTL). Photographs and spectra of the electroluminescence from five QD-LEDs that have different color emitting QDs [1].

commercially available OLEDs.

These high efficiency and multicolor QD-LEDs were made possible by the development of QD contact printing, in which single monolayers of QDs can be transferred, solvent-free, from a parylene-C coated poly(dimethylsiloxane) (PDMS) stamp onto an organic charge transport layer [15]. The inset photograph in the bottom left of Figure 1-2 shows a display with side-by-side  $25\ \mu\text{m} \times 25\ \mu\text{m}$  RGB pixels, which was created in only two contact printing steps. First lines of red QDs with  $25\ \mu\text{m}$  pitch were printed followed by orthogonal lines of green QDs. The blue emission comes from the organic hole transport layer, TPD.

To illustrate the benefit of the QD-LEDs, we introduce the Commission International de l'Eclairage (CIE) chromaticity diagram, which maps color in terms of hue and saturation (See Figure 1-2). The boundary of the CIE diagram is defined by the different hues that can be perceived by the human eye and which range from 400 nm

to 700 nm. The purer the color, the closer to the boundary it is mapped. The calculation of the chromaticity coordinates,  $x$  and  $y$ , will be presented in Chapter 4; here, it is sufficient to understand that the color gamut enabled by a display with red, green, and blue pixels, is the triangle defined by the coordinates of the individual pixels. In Figure 1-2, we see that the triangle defining the color gamut for a display using red, green, and blue emitting QDs (solid black line) is larger than that of the International Telecommunication Union HDTV standard (dotted black line), highlighting the benefit of using QD emitters.

Unlike most white light sources that require stacking of different color pixels or down-conversion schemes, the work of Anikeeva *et al.* [16] demonstrates that it is possible to fabricate a white LED by incorporating a monolayer of mixed red, green, and blue QDs between organic hole and electron transporting layers. Figure 1-2 also presents a photograph of this white QD-LED which has an EQE of 0.36% at 10 V applied bias and a color rendering index of 87. With seven different color QDs in a monolayer, a white-emitting QD-LED with a color rendering index of 95 could be achieved (Figure 1-2).

While these results clearly illustrate the promise of QD-LEDs for displays and large area lighting; one principle limitation to these QD-LEDs with organic transport layers is that, like OLEDs, they require environmental packaging to prevent degradation of the organic transport layers in the presence of atmospheric  $O_2$  or water vapor. Device lifetimes can be improved with packaging in an inert atmosphere, but packaging increases complexity and cost in manufacturing. Environmental packaging is particularly challenging for conformal displays which might utilize flexible plastic substrates that are porous by design. A primary goal of this thesis was therefore to investigate whether replacing the organic charge transport layer with inorganic charge transport layers, would enable air-stable devices that do not require packaging.

When this work was started in 2005, previous efforts at building air-stable colloidal QD-LEDs with inorganic charge transport layers had demonstrated only limited QD electroluminescent efficiencies. The most promising work used n- and p-type doped GaN transport layers surrounding colloidal QDs and reported external quantum effi-

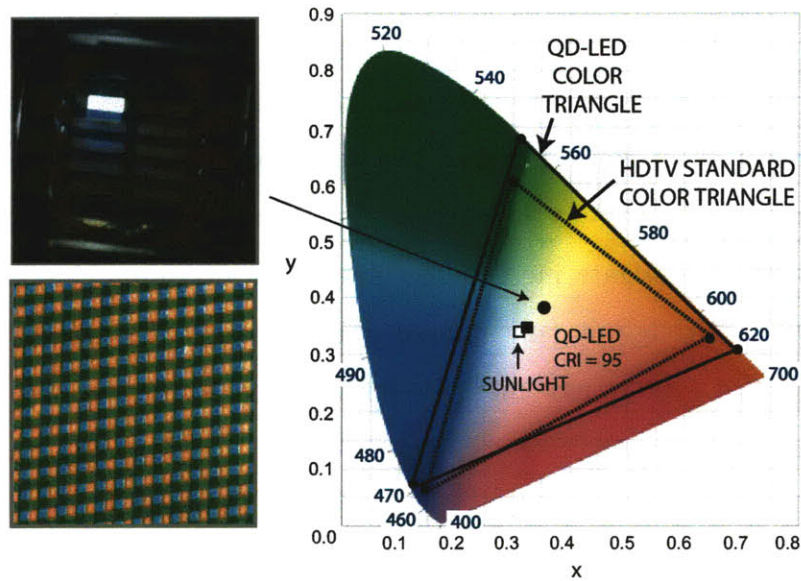


Figure 1-2: Microcontact printing of QDs enables side-by-side deposition of micron-scale red, green, and blue pixels (bottom left), or mixing of red, green, and blue QDs within a single monolayer to create a single white light emitting active layer (top left). CIE chromaticity diagram showing the spectral purity of QDs enables a color gamut larger than the HDTV standard.

efficiencies of 0.001 % to 0.01 %, although much of the observed EL was from the GaN [17] and fabrication required the specialized deposition technique of energy neutral atomic beam lithography/epitaxy (ENABLE). One explanation for this low efficiency is that this structure, unlike QD-LEDs with organic based charge transport layers, cannot benefit from Förster energy transfer of an exciton from a wide band gap organic layer to a QD; in this inorganic QD-LED, only direct charge injection plays a role in QD excitation. Indeed, subsequent work from the Klimov group at Los Alamos National Laboratory focused on using InGaN/GaN quantum well structures in close proximity to the QD layer to enable both energy transfer and carrier injection as means for exciting QDs in an all inorganic structure [18].

Since then, other efforts have been launched to build air-stable QD-LEDs; however, all these focused on hybrid QD-LEDs with both inorganic and organic transport layers. For example, a solution-deposited ZnO nanocrystal-based electron transport layer was successfully implemented in work by Stowdam *et al.* [19]. Another group

explored cross-linking of the QD layer followed by spin-cast deposition of a sol-gel  $\text{TiO}_2$  electron transport layer using DuPont precursor tyzol BTP [20]. By retaining one organic layer, these devices benefit from the dual excitation mechanisms of Förster energy transfer and direct charge injection while gaining stability from the one ceramic transport layer.

This thesis will investigate methods for systematically improving the efficiency in QD-LEDs with entirely inorganic charge transport layers that operate via direct charge injection and explore new methods for electrical excitation of colloidal QDs within inorganic structures.



## Chapter 2

# Colloidally Synthesized Quantum Dots

In this Chapter, we begin by introducing quantum dots (QD) and explaining how the quantum size effect in semiconductors causes many of the unique optical properties of QDs. The syntheses of the colloidal QDs used in this work are detailed in Section 2.1. Since the device architectures presented in this thesis all involve application of a voltage across the QD layer, Sections 2.2, 2.3, and 2.4 discuss the effects of an electric field on QD ensembles, the physics of current flow through a QD film, and Coulomb processes in QDs. Recognizing the signature of electrical field, current flow, and charging in QD systems is key to understanding the QD-LED behavior presented in Chapters 5-7.

While this thesis focuses exclusively on the use of colloidally synthesized QDs for light emitting devices, it is important to mention that there are in fact two types of QDs: epitaxial and colloidal. Colloidal QDs are synthesized from organometallic precursors injected into an organic solvent at high temperature. The temperature activates nucleation of small crystallites, which continue to grow from the unreacted precursors until stopped by cooling. This procedure allows for fine control over QD size and results in a highly monodisperse sample. The synthesis also leaves colloidal QDs coated in organic ligands so that the QDs can be made soluble in a diverse set of solvents including chloroform, hexane, ethanol, and even water. Colloidal QDs are

therefore solution processable and can be patterned on substrates using large scale techniques such as spin coating, microcontact-printing, and inkjet deposition.

Epitaxial QDs, often known as self-assembled QDs (SAQDs), form when a semi-conducting material is deposited, generally through molecular beam epitaxy (MBE), on a substrate having a different lattice constant or at a very high rate. Strain causes the top material to buckle and form QDs, in what is referred to as Stranski-Krastanow growth. MBE can then be used to deposit a capping layer and the top charge injection layer. Thus, as grown SAQDs are already integrated into a monolithic semiconductor structure making them an obvious choice for a robust and stable all-inorganic LED structure.

However, colloidal QDs possess properties that make them superior to epitaxial QDs for many optoelectronic applications. Epitaxial QDs do not offer the monodispersity, the high photoluminescence intensities, or the large area fabrication advantages of colloidally synthesized QDs. Furthermore, the size of an epitaxial QD is determined by the material set available. This prevents integration of more than one color QD into the device structure, making it difficult to realize RGB pixels or white light from epitaxial QDs. This thesis focuses on the development of LEDs with colloidal QDs sandwiched between inorganic charge transport layers.

Reference [21] provides the basic mathematical framework to show how the absorption and emission properties of a QD are governed by the quantum size effect. The material of a QD is structurally identical to that of the bulk crystal, but, in a QD, the electron and hole pairs are confined by boundaries of the QD. This confinement leads to quantization of the bulk energy levels, resulting in atomic-like absorption and emission spectra for QDs. These quantum size effects become important when the size of the QD is less than the Bohr radius:  $a_B = \epsilon \frac{m}{m^*} a_0$ , where  $\epsilon$  is the dielectric constant of the material,  $m^*$  is the effective mass of the particle (electron or hole), and  $m$  is the rest mass of the electron, and  $a_0$  is the Bohr radius of the hydrogen atom. When the radius of a QD is smaller than the Bohr radius of the hole, electron, and exciton, we can approximate the energy levels of a QD using the particle in a sphere model. That is, electrons and holes can be considered to be in a hollow sphere

enclosed by an infinite potential. The energy of a particle in this potential is given by

$$E_{n,l} = \frac{\hbar^2 k_{n,l}^2}{2m_0} = \frac{\hbar^2 \alpha_{n,l}^2}{2m_0 a^2}, \quad (2.1)$$

where  $\alpha_{n,l}^2$  is the  $n$ th zero of the  $l$ th-order spherical Bessel function. These energies resemble the kinetic energy of a free particle, except that in this case the wave vector,  $k_{n,l}$ , is quantized. From Equation 2.1, it follows that as the confinement increases ( $a$  decreases), the energy of the electron or hole wavefunctions is increased, and an electron-hole pair recombination event will release more energy. Therefore, as CdSe QDs are reduced in size, the emission peak shifts to bluer wavelengths.

In bulk crystalline semiconductor theory, it is assumed that every particle in the solid experiences some average potential that is periodic, such that its wavefunctions can be described by Bloch functions:

$$\Psi_{n,k}(\vec{r}) = u_{n,k}(\vec{r}) \exp(\vec{k} \cdot \vec{r})$$

where  $u_{n,l}(\vec{r})$  has the same periodicity as the crystal potential and  $\exp(\vec{k} \cdot \vec{r})$  describes the wavefunction phase shift between the atoms of the crystal. The wavefunctions are indexed by the wavevector  $k$  and the band index  $n$ . Furthermore, the effective mass approximation considers the conduction and valence bands of the semiconductor to be parabolic and uses the effective mass to account for the complexities of the band structure. If the QD diameter is larger than the lattice constant of the QD material, it is possible to use the effective mass approximation and write the single particle wave function as a linear combination of Bloch functions:

$$\Psi_{sp}(\vec{r}) = \sum_k C_{n,l} u_{n,l}(\vec{r}) \exp(\vec{k} \cdot \vec{r}) \quad (2.2)$$

By separating terms with strong and weak  $k$  dependence, Eqn.2.2 becomes

$$\Psi_{sp}(\vec{r}) = u_{n,0}(\vec{r}) \sum_k C_{n,l} \exp(\vec{k} \cdot \vec{r}) = u_{n,0}(\vec{r}) f_{sp}(\vec{r}),$$

where  $f_{sp}(\bar{r})$  is the envelope wavefunction and  $u_{n,0}(\bar{r})$  can be determined from the tight-binding approximation by summing over the atomic wavefunctions,  $\varphi_{n,k}$ . With these approximations, it is possible to write the energy of the electron-hole pair states as

$$E = E_g + \frac{\hbar^2}{2a^2} \left( \frac{\varphi_{n_h, k_h}^2}{m_h^*} + \frac{\varphi_{n_e, k_e}^2}{m_e^*} \right) - \frac{1.8e^2}{\epsilon a}, \quad (2.3)$$

where  $\frac{1.8e^2}{\epsilon a}$  is the first order Coulombic correction factor that accounts for the attraction between the electron and the hole in the QD. Equation 2.3 highlights that the emission from a QD due to radiative recombination of an electron-hole pair is dependent on the bandgap of the bulk semiconductor and the size of the QD. In Section 2.1, we discuss how both chemistry and size can be used to make highly luminescent QDs with narrowband emission anywhere in the visible and near-infrared wavelength region.

The absorption spectrum,  $\alpha(\omega)$ , is also dependent on the size of the QD. It is derived as for the bulk crystal case:

$$\alpha(\omega) = \frac{\pi q^2 c \mu_0}{m_0^2 \omega n} |p_{cv}|^2 \rho(\hbar\omega - E_g) \quad (2.4)$$

where the overlap of the electron and hole wavefunctions is given by the dipole matrix element

$$p_{cv} = \langle u_c | \hat{e} \cdot \bar{p} | u_v \rangle$$

and is related to the probability that an electronic transition will occur.  $\rho$  is the density of states, which are  $\delta$ -functions in the case of the zero-dimensional QD. We therefore expect a size-dependent absorption spectrum with a narrow peak marking the onset of absorption. Both of these features are seen in the absorption spectra in Figure 2-1; however, the first absorption peak is widened due to inhomogeneous broadening. Further discussion of inhomogeneous broadening stemming from size variations within a QD sample will follow in Section 2.2.

While this simplistic particle in a sphere model explains the basic absorption and emission properties of QDs, it does not account for the complexity of the valence band,

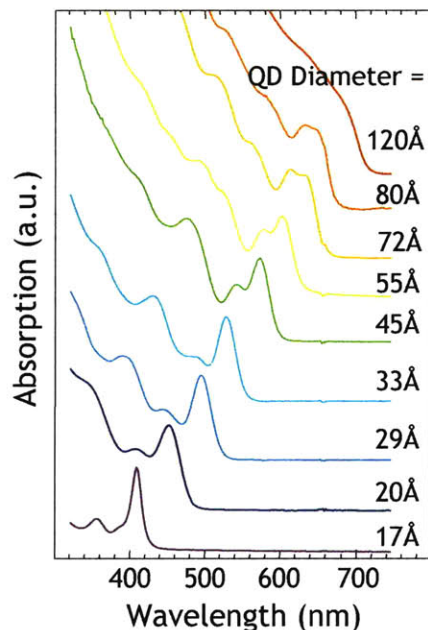


Figure 2-1: Absorption spectra for a series of CdSe samples ranging in size from 2 nm to 12 nm in diameter.

the mixing of the three valence subbands, or the electron-hole exchange interaction. Much theoretical work has been done developing more advanced models that take into account these effects; however, they are not critical to understanding the results presented in this thesis.

## 2.1 Colloidal QD Synthesis

The first examples of colloidal QDs were CdSe, CdS, and CdTe nanocrystals [9]. Figure 2-2 shows the basic steps of colloidal QD synthesis. A reaction vessel containing a coordinating solvent for colloidal dispersion and ligands for surface passivation is preheated to 300°C and then removed from the heat. Organometallic precursors are then injected into the reaction vessel which results in homogeneous nucleation of nanocrystals. This nucleation reaction causes the temperature of the vessel to drop to approximately 180°C. The reaction vessel is then gradually reheated to approximately 300°C to allow for slow growth and annealing of the QDs. The absorption spectrum of the reaction solution is monitored and the growth temperature modu-

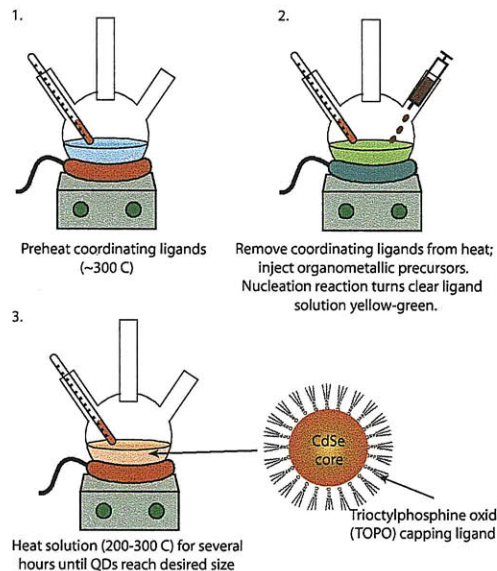


Figure 2-2: The basic steps involved in a colloidal QD synthesis.

lated to precisely control the size of the QDs. Less than 5 % deviation in QD size is typically obtained. The QDs are precipitated and centrifuged dry to separate them from the reaction byproducts. They are then redispersed in the solvent of choice. Hines [22] and Dabbousi *et al.* [23] presented methods overcoating CdSe core QDs with ZnS shells and demonstrated that the stability and efficiency of QDs can be enhanced by overcoating.

Narrow-spectrum light emission across the entire visible spectrum can be generated with the standard CdSe or CdSe/ZnS QDs; however, the luminescent efficiency of even the core/shell structures varies greatly between different wavelengths. For example, while orange-emitting CdSe/ZnS QDs exhibit record quantum yields, CdSe/ZnS QDs are not efficient in the deep red or blue parts of the spectrum. The following paragraphs summarize the different chemistries and synthetic procedures implemented by Jonathan Halpert [24] in the group of Professor Mounqi Bawendi at MIT to generate QDs with high quantum yields across the visible spectrum. This thesis makes use of these in-house synthesized QDs as well as commercial CdSe/ZnS QDs from Evident Technologies and QD Vision, Inc.

Red QDs used in this thesis are either CdSe/Zns core-shell QDs or ZnCdSe alloyed

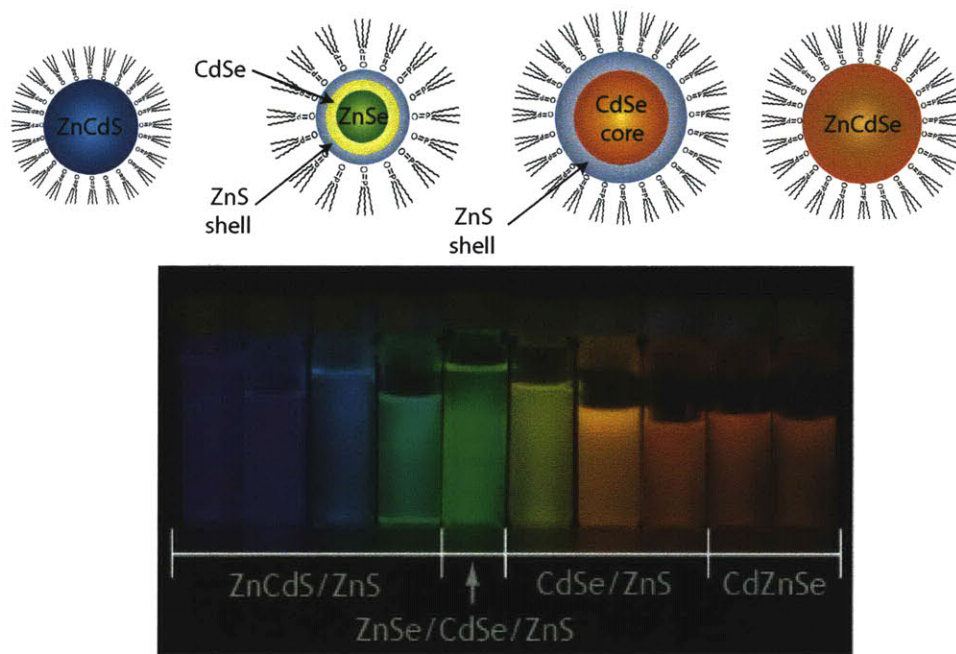


Figure 2-3: Schematic of the structures of ZnCdSe, CdSe/ZnS, ZnSe/CdSe/ZnS, and ZnCdS QDs and a photograph of their photoluminescence in solution. Photograph courtesy of J. Halpert.

QDs, shown schematically in Figure 2-3. The CdSe/ZnS QDs are provided by QD Vision, Inc. and are synthesized following the method of Dabbousi *et al.* [23]. In this method, CdSe cores are synthesized as depicted in Figure 2-2. These CdSe cores, capped with trioctylphosphine oxide (TOPO), are placed in a reaction vessel, which is heated to a temperature between 200 °C and 300 °C. The organometallic precursors (diethyl zinc and hexamethyldisilathiane) for the ZnS shell are slowly injected into the vessel and stirred. The solution is cooled to 90 °C and left stirring for several hours. The QY of CdSe/ZnS QDs in solution is 95 %. Alloyed ZnCdSe QDs are synthesized following the work of Zhong *et al.* [25] in which trioctylphosphine selenide (TOP-Se) is injected into a flask of ZnO, CdO, oleic acid, and 1-octadecene at 310 °C.

The green QDs used in Chapters 5 and 6 of this work are ZnSe/CdSe/ZnS core/double-shell structures (See Figure2-3) synthesized based of the work of Ivanov *et al.* [26] and Steckel *et al.* [27]. ZnSe cores are prepared by injecting a solution of diethyl zinc, trioctylphosphine selenide (TOP-Se) and TOP into a flask of hexadecylamine (HDA) at 310 °C. The cores are then grown at 270 °C for 2 hours. The solution is cooled to 150 °C and then injected into a degassed solution of TOPO and hexylphosphonic acid (HPA) while a solution of dimethyl cadmium, TOP-Se and TOP is added dropwise. The solution is heated at 150 °C for 19 hours. These cores, made of ZnSe and CdSe, are separated from their growth byproducts and placed in a reaction vessel at 150 °C. Two solutions, one of dimethyl cadmium, diethyl zinc and TOP, the other of bis(trimethylsilyl) sulfide (TMS<sub>2</sub>-S) and TOP are added slowly to the vessel after which the solution is cooled to room temperature. The QY of the ZnSe/CdSe/ZnS QDs is 65 % in solution. Green CdSe/ZnS QDs are purchased from Evident Technologies.

Blue emitting QDs used in Chapter 5 are ZnCdS alloyed structures (See Figure 2-3) and are prepared in a fashion similar to that reported in [28]. A degassed solution of oleylamine and elemental sulfur is injected into a flask under argon, which contained a solution of CdO and ZnO dissolved into oleic acid and octadecene at 310 °C. The QY for these ZnCdS QDs is 48 % in solution. These ZnCdS shells can be overcoated with ZnS for increased stability and higher QYs; however, these ZnCdS/ZnS QDs were not



used in this thesis because of band alignment considerations, which will be described in detail in Chapters 4 and 5. Blue CdSe/ZnS QDs in Chapter 7 are purchased from Evident Technologies.

Infrared emitting QDs use smaller bandgap semiconductors such as PbSe or PbS; however, these lead chalcogenide-based QDs are unstable and prone to oxidation. Pietryga *et al.* demonstrated a partial cation-exchange method to controllably overcoat lead chalcogenide core materials to form more stable, infrared-emitting core/shell structures such as PbSe/CdSe, PbS/CdS, and PbSe/CdSe/ZnS [29]. Rather than use conventional methods to synthesize a shell around core QDs in which the organometallic precursors to form the shell are injected into a flask with cores, the partial cation-exchange method relies on the lability of Pb ions, which are susceptible to exchange with Cd ions when immersed in a highly concentrated solution of cadmium oleate. Scott Geyer in the Bawendi Group used this technique to synthesize stable PbS/CdS QDs with photoluminescent quantum yields in solution of  $35 \pm 5\%$  and emission peaks from 1.0  $\mu\text{m}$  to 1.5  $\mu\text{m}$ . Three representative photoluminescence spectra for these PbS/CdS QDs are shown in Figure 2-4 along with a photograph of a vial of the 1.5  $\mu\text{m}$ -emitting QD solution. Chapter 7 presents a method for obtaining electroluminescence from these PbS/CdS QDs.

Removal of excess ligands from the growth solution is a key step to making QD films that are suitable for electrical excitation. Typically we precipitate the QDs at least two times. For QDs with oleic acid capping ligands, we precipitate the QDs from the growth solution using acetone, redisperse in hexane, precipitate a second time using methanol and butanol, and finally redisperse the QDs in chloroform. For QDs with TOP or TOPO ligands, we precipitate them two times from hexane using methanol and butanol before redispersing the QDs in chloroform. Prior to each precipitation step, the dispersion is passed through a 0.2  $\mu\text{m}$  filter. The precipitation is accelerated by centrifuging the solution at 3500 RPM for 5 minutes.

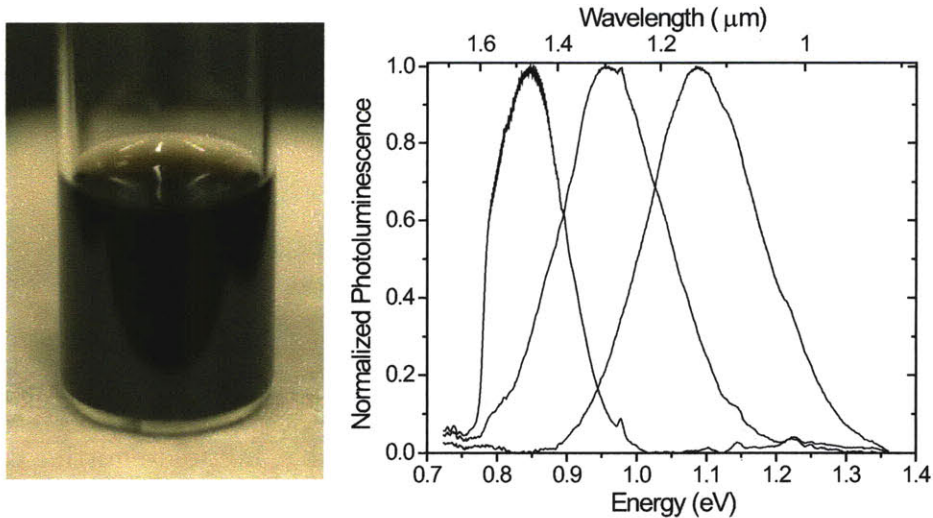


Figure 2-4: a) A photograph of a vial of PbS/CdS QDs that emit in the infrared with a peak near 1500 nm. b) Photoluminescence spectra of three different PbS/CdS QD solutions. The red-side of the 1500 nm QD spectrum is clipped because of the limit in the InGaAs detector used to collect spectra.

## 2.2 QDs in an Electric Field

In Chapter 6, we explain how changes in spectral shape of QD photoluminescence and electroluminescence in response to an applied electric field can be used to understand the operating mechanisms of the device structure under investigation. The effect of an external electric field on colloidal QDs has been the subject of intense investigation [2, 30, 31, 32, 33] and this section seeks to summarize the relevant findings in these works.

The shifting in the bound state energies in a quantum confined solid in response to an applied electric field is known as the Quantum Confined Stark Effect (QCSE). This shifting in energy levels causes a change in the effective band gap of the material, which can be observed physically as a change in the absorption spectrum or a shift in the position of the luminescence peak position as a function of applied field. If we assume that the interaction between the bound state energies and the electric field is smaller than the energy difference between the excited states, we can describe the QCSE with second order perturbation theory. The shift in the effective bandgap of a QD in the presence of an electric field,  $\bar{F}$ , is given by

$$E_n^f - E_n = \langle \Psi_n | e\vec{r} \cdot \vec{F} | \Psi_n \rangle + \frac{\sum_{i \neq n} |\langle \Psi_n | e\vec{r} \cdot \vec{F} | \Psi_i \rangle|^2}{E_n - E_i}. \quad (2.5)$$

The first term is the dot product of the dipole moment ( $e\vec{r}$ ) of the QD and the electric field, which means that this term can range from negative to positive values depending on whether the dipole moment of the QD is anti-aligned or aligned with the electric field. The second term is related to the polarizability of the QD, in other words the extent to which the electron cloud can move in response to an electric field. To see the dependence on field more clearly [32], we rewrite 2.5 as

$$\Delta E = \mu F + \frac{1}{2}\alpha F^2, \quad (2.6)$$

where  $\mu$  is the projection of the dipole moment in the direction of the electric field and  $\alpha$  is the polarizability of QD in the direction of the electric field.

If we record the shift in the peak position of the luminescence spectrum of a single QD, we find a quadratic dependence of the shift with electric field and a superimposed linear dependence that can cause either a red shift in peak position (in the case where the QD dipole is aligned with electric field) or a blue shift in peak position (in the case where the QD dipole is anti-aligned with the electric field) [32]. In contrast, in a QD ensemble, the dipoles of the different QDs will be randomly aligned. QD with dipole contributions along the field and against the field will contribute to the broadening of the luminescence spectrum with the peak position left unchanged [32]. In such a case, the linear term in 2.6 is neglected, and the shift in the spectral emission peak is:

$$\Delta E = \frac{1}{2}\alpha F^2.$$

Such a quadratic dependence of the shift in peak position with applied field has been observed for QD ensembles where the QDs are electrically isolated from one another [32].

To better understand the details of a luminescence spectrum of a QD film under an applied electric field, we must first look at a typical single QD spectrum (See

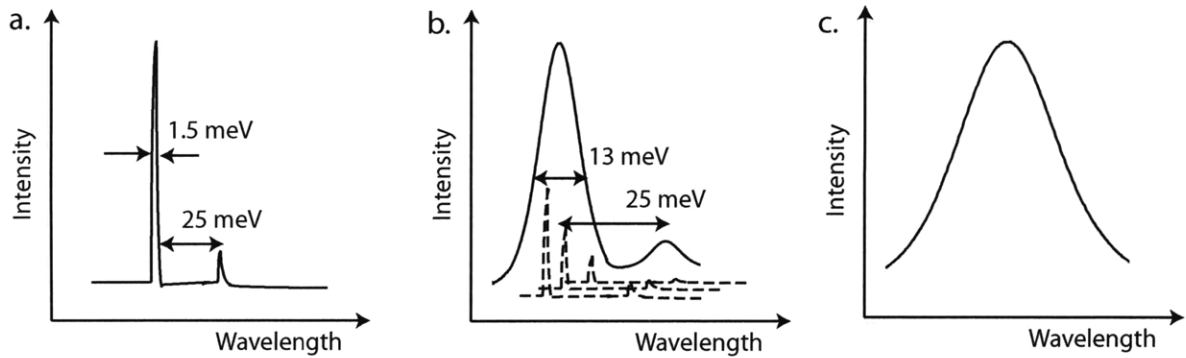


Figure 2-5: Schematics of a) single QD spectrum, b) a fluorescence line narrowed ensemble QD spectrum, and c) a QD ensemble spectra. Panels b and c illustrate how the ensemble QD spectrum is a convolution of many single QD spectra that are slightly offset as a result of a finite size distribution in a given QD sample.

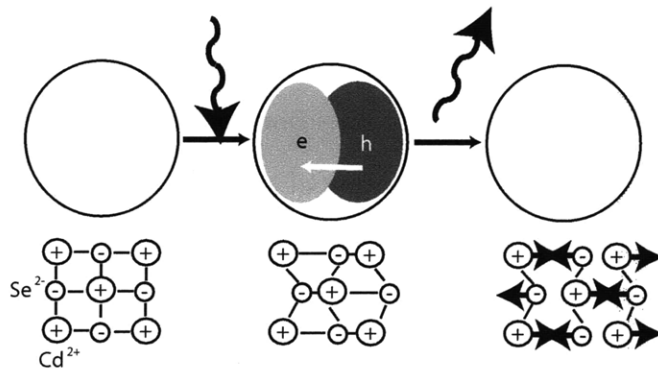


Figure 2-6: Schematic depiction Fröhlich coupling in QDs [2].

schematic in Figure 2-5a) [34]. A single QD spectrum has a main peak (the zero phonon line or ZPL) with an extremely narrow linewidth and a clearly defined longitudinal optical (LO) phonon line. The ZPL can be understood as a direct excitation of the QD while the LO phonon line is the result of the excitation of the QD and a simultaneous excitation of a phonon (See Figure 2-6). When a photon excites a QD, an exciton is formed. The exciton has a certain separation between the electron and hole wavefunctions which causes an internal electric field within the QD and distorts the lattice. When the exciton recombines, the internal field disappears and the lattice relaxes, creating phonons [2]. The first optical phonon line occurs at a well defined energy because the optical phonons are themselves quantized in a colloidal QD.

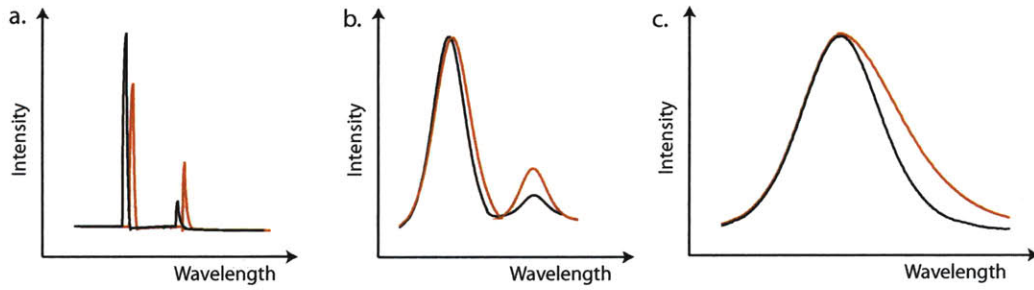


Figure 2-7: Comparison of spectra for QDs under no applied electric field (black lines) and an applied electric field (red). Schematics represent a single QD spectrum (a), a fluorescence line narrowed ensemble QD spectrum (b), and an ensemble QD spectrum (c). These schematics illustrate why a QD ensemble under an applied field appears to be red-shifted and broadened.

Figure 2-5b shows a schematic of a fluorescence line narrowed spectrum of a QD ensemble [34]. Fluorescence line narrowing is a technique to probe a QD ensemble while reducing the inhomogeneous broadening by exciting only a small portion of the QDs so that features such as the ZPL and LO phonon line can still be observed. Inhomogeneous broadening occurs as a result of the finite size distribution in QDs, and can mask many features of a QD spectrum. Practically, fluorescence line narrowing involves use of an excitation source slightly to the red in energy of the absorption onset. In addition to using fluorescence line narrowing, these schematic renditions of QD spectra assume that the QD sample is cooled to 10 K, where thermal excitation of phonons is limited. Nonetheless, the line width of the ZPL and LO phonon line are broadened due to the contribution of multiple QDs with slightly different sizes and therefore different energies or due to slightly different local dielectric environments. If fluorescence line narrowing is not used and the measurement is performed at room temperature, an ensemble spectrum such as the one in Figure 2-5c is observed.

Figure 2-7 shows what each of the spectra in Figure 2-5 can resemble under an applied electric field. The QCSE cause a red shift in the peak position with increasing electric field. Figure 2-7a also shows that the LO phonon line increases in magnitude with respect to the zero field condition. In an ensemble QD luminescence spectra, this increased phonon coupling due to an applied electric field can be seen as a broadening of the red-side of the QD emission spectrum. The QCSE and changes in the phonon

coupling in QD-LEDs are experimentally investigated in Chapter 6 to assess the device operating mechanism.

## 2.3 Charge Transport in Colloidal QD Films

In most QD-based optoelectronic devices, charge transport through the QD film is a critical parameter, as it often directly affects the efficiency of device operation. In photovoltaic applications, charge generated in the QD active layer must be extracted efficiently. In LEDs that operate based on direct charge injection, charge must be transported effectively and uniformly to a large number of QDs.

One difficulty facing electrical transport in an as-deposited film of CdSe QDs is the high resistance of nanocrystal films. Sheet resistance values are reported to be near  $10^{23} \Omega/\square$ . Multiple studies have shown that decreasing the length of the insulating ligands (e.g. from trioctylphosphine oxide to butylamine) through ligand exchange techniques or annealing the QD to remove ligands can improve conduction through QD films [35, 36]. However, ligand exchange or annealing can be detrimental to the morphology or luminescent efficiency of the QD film. If ligands are exchanged on QDs already deposited as a thin film, the resulting volume decrease in the film can cause cracks in the QD film that act as current shunts. Furthermore, if ligands are removed, surface states are left unpassivated and trap state emission can result. This problem is less pronounced for QDs that are overcoated with an inorganic shell (such as ZnS). Recent work has shown, for example, that “giant” shell QDs exhibit luminescence even after the ligands have been removed with heat [37]. Challenges surrounding the conductivity of ligands may ultimately be resolved by moving to metal chalcogenide ligands, which recently enabled QD films with relatively high mobilities [38].

However, in addition to poor conduction, charge transport in QD films is complicated by its dependence on long range Coulombic interactions between charges confined on different nanocrystals. If a constant voltage is applied across two electrodes with QDs in between, no steady state current is observed. Instead, the measured current follows a power law decay with time [35, 39]. When charge enters the QD film,

it builds up in the first layer of QDs. This space charge creates a “Coulomb glass” [40], in which localized charge in a disordered solid (i.e. the QD film) prevents further motion of electrons. Over sufficiently long time scales, the Coulomb glass can relax, once again allowing passage of charge. The relaxation is a statistical process that is correlated to temperature [39, 41] and occurs randomly at different points in the QD film.

This space charge buildup in the QD film has significant impact on QD-LED design (discussed in detail in Chapter 6). In particular, charging of the QD layer results in a drop in device current and eventual turnoff of the device if operated continuously. Furthermore, if the applied voltage is simply switched off and then on again (on the time scale of seconds or even minutes), the QD film will retain the resistivity it had when the voltage was switched off. This memory effect is consistent with the very slow relaxation dynamics of a Coulomb glass at room temperature.

## 2.4 Luminescence Quenching in Colloidal QDs

This section summarizes two contributing factors to luminescence quenching in QD-LEDs. While exact mechanisms of QD luminescence quenching are still poorly understood, an overview of current research is provided here.

In addition to affecting the transport properties of a QD film, QD charging is believed to be detrimental to luminescence. In 1996, Nirmal *et al.* reported the observation of fluorescence intermittency (blinking) in single CdSe QDs [42]. In an effort to explain this phenomenon, it was proposed that the luminescence off-state for a QD corresponded to charged QD. A charged QD could result from either Auger ejection or charge tunneling from the surrounding matrix [43]. The extra carrier on the QD could then mediate an Auger non-radiative recombination event [44]. In an Auger process, an electron-hole pair recombine transferring the resultant energy to an additional carrier. This “hot” carrier can then relax down to the band edge via phonon emission. Indeed, Auger processes are documented to be very efficient in colloidal QDs. While an exciton lifetime in a colloidal QD is 10 ns, multiexciton

lifetimes are typically on the order of tens of picoseconds [45]. However, recent work by G. Nair has demonstrated that this simple charging model for QD blinking is inconsistent with blinking dynamics of exciton and multiexciton states [46]. Namely, the Auger processes observed are too fast to be explained by the presence of only one additional charge. Instead, Nair proposes that blinking could be explained by the buildup of multiple charges on a QD, which can occur if the excitation rate is faster than the trap recombination times. Alternatively, luminescence quenching could be explained as a trap assisted recombination process [46]. In this case, when an electron-hole pair is created, one of the carriers becomes trapped. The other carrier can then non-radiatively recombine with a trapped carrier, leaving a neutral QD that does not blink.

While QDs that suppress blinking have already been reported [37, 47], further understanding the role of charging on the blinking phenomenon will be beneficial for rational design of QD systems for LEDs and lasing. Experiments in Chapters 5 and 6 of this thesis indicate the extent to which charging of the QD layer decreases the luminescence of the QD films, and demonstrate that reduction of charging in QDs can lead to higher luminance and more stable devices.

For the purposes of this thesis it is also important to understand that the external environment of the QDs substantially affects their luminescent quantum yields. For example, if QDs are located next to a film with high carrier concentrations (e.g. a smooth gold film) their luminescence will be quenched through non-radiative energy transfer [48]. In Figure 2-8, we show that progressively higher conductivity metal oxide films show increasing QD luminescence quenching. Section 5.3 explains how decreasing the conductivity of the metal oxides adjacent to a QD film can decrease the luminescence quenching and boost QD-LED efficiency.

Energy transfer between neighboring QDs or trap states on these QDs can itself be problematic. Indeed, the photoluminescence (PL) efficiency of a dilute solution of QDs is an order of magnitude greater than the PL efficiency for a thin film of the same QDs, where QDs are in close proximity and the surface states are less well passivated. It has been demonstrated that dispersing the QDs in an insulating polymer such that



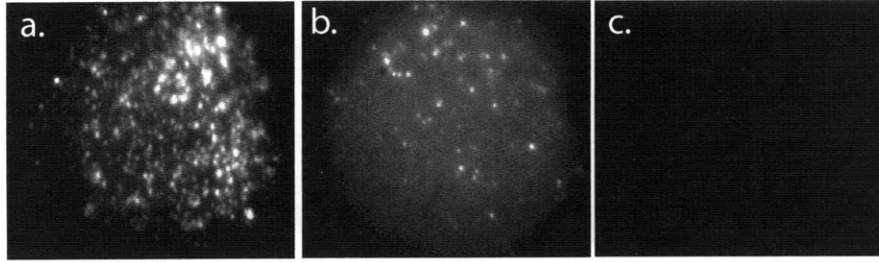


Figure 2-8: Photoluminescence of single QDs on a) glass, b)  $\text{WO}_3$  with a resistivity of  $10 \Omega \cdot \text{cm}$ , and c)  $\text{WO}_3$  with a resistivity of  $0.2 \Omega \cdot \text{cm}$ . The concentration of QDs in the illuminated area is equivalent for each sample, and the excitation source is the same for each sample.

the QDs are electrically isolated from one another is a method for retaining their PL efficiency in thin film [49, 50]. While such QD-polymer dispersions are ideal for optical excitation of QDs, they complicate electrical injection of charge into the QDs. However, Chapter 7 of this thesis presents a device geometry that allows for small clusters of QDs embedded in insulated polymers to be electrically excited.



# Chapter 3

## Metal Oxides

Metal oxides, and ceramics in general, are an attractive materials set to investigate for integration with colloidal QDs because of their range of electrical properties. Ceramics typically have the chemical formulas  $M_aX_c$  or  $M_aN_bX_c$ , where M and N are metals, and X is a nonmetallic element. They can be metallic (e.g.  $TiO_2$ ), insulating (e.g.  $SiO_2$  or  $ZnO$ ), or semiconducting (e.g. nonstoichiometric  $ZnO$  or  $NiO$ ), enabling the development of different device architectures with which to explore mechanisms for electrical excitation of QDs. This chapter discusses the variety of techniques available for depositing ceramics with a focus on radio frequency magnetron sputtering, which is the primary method for ceramic deposition used in this thesis. The physical origins of charge transport and dielectric properties in ceramics are also explained.

There are multiple techniques available for depositing ceramic materials, and, in the past several years, considerable attention has been given to demonstrating their compatibility with colloidal QDs, highlighting the widespread interest in developing functional ceramic and colloidal QD-based devices. Below we review a variety of chemical and liquid phase deposition techniques, before turning to physical vapor deposition in Section 3.1.

Molecular beam epitaxy (MBE) is an ultra-high vacuum technique which involves sublimation of pure elements that then condense on a substrate where they can react to form single crystal films with very low defect concentrations. As discussed briefly in Chapter 2, self-assembled QDs (SAQDs) are formed when a semiconduct-

ing material is deposited, generally through MBE, on a substrate having a different lattice constant or at a very high rate. Strain causes the top material to buckle and form QDs in what is referred to as Stranski-Krastanow growth. MBE can then be used to deposit a capping layer and the top charge injection layer creating an all-inorganic LED structure. However, SAQDs do not offer the monodispersity, the high photoluminescence intensities, or tunability of size and chemistry of colloidal QDs, which make the latter superior for optoelectronic applications. Efforts have therefore been made to integrate colloidal QDs into MBE grown structures. For example, one study demonstrated use of migration enhanced epitaxy (a form of MBE in which constituent elements are introduced sequentially) to deposit a ZnSe film on CdSe/ZnS core/shell colloidal QDs which were solution deposited on a MBE grown ZnSe layer [51]. The photoluminescent properties of the core/shell QDs were maintained within the epitaxial grown ZnSe.

In chemical vapor deposition (CVD) gaseous precursors react on a heated substrate. For example, silane  $\text{SiH}_4$  and oxygen can react to form  $\text{SiO}_2$  and hydrogen gas as a by-product. CVD often requires substrate heating in excess of  $600^\circ\text{C}$ , at which temperature QDs would anneal, losing their quantum confined optical properties. The first demonstration of all inorganic QD-LEDs with p- and n-type charge transport layers used a variation of CVD, energetic neutral atom beam lithography/epitaxy (ENABLE) [17]. ENABLE does not require elevated substrate temperatures and reactive precursors that destroy the luminescent properties of QDs. Instead ENABLE involves a chemical reaction on the sample surface between a beam of neutral atoms, such as nitrogen, and a metal, like gallium, that is simultaneously deposited via e-beam evaporation. Low temperature ENABLE ( $300^\circ\text{C}$ ) allows deposition of GaN on the QDs without compromising their performance; in fact, the authors report that the GaN acts as an encapsulating layer, reducing the photo-oxidation of the QDs.

Atomic layer deposition (ALD) is a variation of CVD that consists of repeated, sequential exposure of a substrate to gas phase precursors, with the reaction chamber purged before the introduction of each precursor to remove any unreacted precursor and reaction by-products. The result is a series of self-limiting chemical reactions that

form a dense, conformal thin film. ALD can be used to deposit many oxides, nitrides, and sulfides at relatively low temperatures ( $< 150^\circ\text{C}$ ). For example, trimethylaluminum ( $\text{Al}(\text{CH}_3)_3$  or TMA) and water can be used as precursors for the formation of  $\text{Al}_2\text{O}_3$ . In this case, water vapor in the air is adsorbed onto the Si substrate forming hydroxyl (OH) groups. When TMA is introduced into the chamber, it reacts with the OH on the Si, forming an Al-O bridge with two dangling methyl groups on the Al, and methane gas ( $\text{CH}_4$ ) as the reaction by-product. TMA reacts with all available OH groups and then, since it cannot react with itself, the reaction stops. The reaction chamber is purged of  $\text{CH}_4$  and excess TMA. Water vapor is then introduced into the chamber. The water reacts with the dangling methyl groups, forming more Al-O bridges with hydroxyl surface terminations and methane gas. Again, the excess methane and water vapor is pumped from the chamber. These steps are repeated until a thin film of  $\text{Al}_2\text{O}_3$  of the desired thickness is formed. Since ALD is a chemical process, proper substrate preparation is required; however, it is not incompatible with QD films. Recent work has shown that ALD-deposited ZnO (using diethyl zinc and water precursors) can infiltrate a colloidal QD film, and improve film mobility by a factor of two to three [52]. The authors reported preservation of the thin-film photoluminescence (PL) for ZnS overcoated QDs, suggesting that ALD deposited metal oxides can be used for QD-LEDs.

Liquid phase deposition of metal oxide thin films has also been investigated for their compatibility with QD devices. Sol-gel is a common liquid phase deposition technique, in which a chemical solution, such as a metal alkoxide, reacts with oxygen or water to form a network of nanoparticles within a liquid. Thermal treatments can be used to remove any remaining liquid and improve the microstructure of the film. A high brightness QD-LED display has been made using a n-type  $\text{TiO}_2$  sol-gel layer on top of QDs [20]. Similarly, a spin cast layer of pre-formed colloidal ZnO nanoparticles has also been successfully used as a n-type transport layer [19]. One important limitation in the use of liquid phase ceramic deposition on a QD film is the need to cross-link the QDs or use orthogonal solvents for the QDs and the sol-gel so that the integrity of the QD film is not compromised in subsequent deposition steps.

While all the deposition techniques described above have been successfully used in conjunction with a QD film, they require carefully designed chemical reactions, often at temperatures that may cause degradation of the QDs. In this thesis, we fabricate the ceramic thin films with a physical vapor deposition technique – radio-frequency (RF) magnetron sputtering – that does not involve a chemical reaction and that can be performed at room temperature. With RF sputtering, film conductivity can be varied by changing the O<sub>2</sub> partial pressure or extrinsically doping the material during growth. Morphology can be controlled with the growth pressure and power. Finally, RF magnetron sputtering rates are similar to those of thermal evaporation, making it a fast deposition technique compared, for example, to MBE or ALD.

The sputtering system used in this work is shown in Figure 3-1. It was custom built by PVD Products, and has three US Inc. sputtering sources with interchangeable power supplies and a variable pressure environment. Ar and O<sub>2</sub> source gases are available, and the substrate can be heated to 400 °C during growth. One DC power supply and two RF power supplies are available, making co-sputter deposition feasible. The system is connected to a transfer line, which is kept at 10<sup>-8</sup> Torr and contains a motorized train that can move substrates between deposition systems connected to the line. The other systems include two thermal evaporators, which were used for deposition of metal films and small molecule organics. The load lock of the transfer line (which can be pumped to high vacuum in under 5 minutes for rapid sample transfer) opens to a pair of N<sub>2</sub> filled glove boxes, one of which is dedicated to solution deposition of polymers and QDs. This setup enables complete fabrication of a QD-LED in an inert environment. While this system was designed for fabrication of optoelectronic devices containing small molecule organics that are air sensitive and our devices are comparatively robust in the presence of O<sub>2</sub> or water vapor, an inert environment is useful for eliminating concerns about the role of interfaces during the device development stages. Furthermore, the transfer line enables rapid switching of shadow masks or transfer of the sample in and out of the deposition chambers without breaking vacuum on the chamber itself.

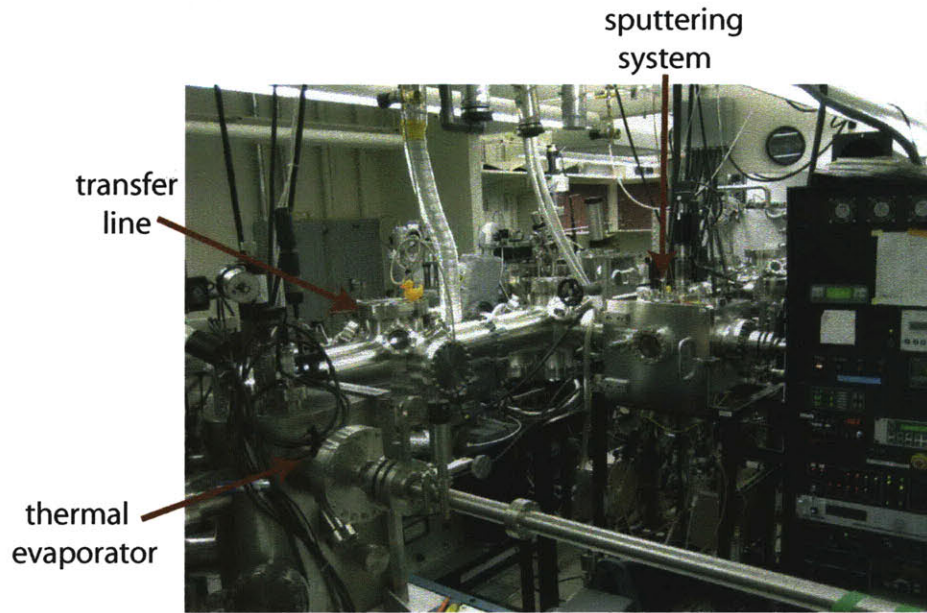
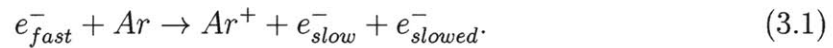


Figure 3-1: Photograph of growth system in the Laboratory for Organic and Nanostructured Electronics at MIT where this work was performed.

### 3.1 Radio Frequency Sputter Deposition

In the sputtering process, energetic ions bombard a target, causing atoms to be ejected from the target and land on a substrate, which, in our system, is located above the target. The ions are provided by a plasma, which is generated by flowing gas, typically argon, between two electrodes. An electron ( $e_{fast}^-$ ), accelerated by the potential between the electrodes, collides with an argon atom resulting in an argon ion ( $Ar^+$ ), a free electron ( $e_{slow}^-$ ), and the now much slower original electron ( $e_{slowed}^-$ ). Symbolically, this reaction, can be summarized by



$e_{slowed}^-$  and  $e_{slow}^-$  are accelerated by the field between the electrodes. When these electrons attain 15.76 eV of energy, which is the ionization energy of Ar, they can each cause the reaction of Equation 3.1. The creation of Ar ions is therefore an avalanche process [53].

To understand RF sputtering, it is useful to review the mechanism for gas discharge in DC sputtering. In DC sputtering, a voltage is applied between an anode and a cathode, and ions are attracted to the cathode while electrons are repelled. This surplus of ions screens the negative charge of the cathode, causing most of the voltage to be dropped across an area close to the cathode, which is known as Crookes dark space. In this space, electrons are accelerated away from the cathode to ionize Ar atoms as described previously. Meanwhile, this voltage drop accelerates ions toward the cathode. The cathode is also the sputtering target, so ions etch microscopic bits of material from target. In this work, we consider relatively low energy sputtering so the process can be modeled as momentum transfer through elastic collisions. The maximum energy transferred in a collision between the ion (with mass  $M_1$  and energy  $E$ ) and a target atom (with mass  $M_2$ ) is

$$\frac{4M_1M_2}{(M_1 + M_2)^2}E.$$

This corresponds to a sputtering yield

$$S \propto \frac{1}{\lambda(E) \cos \theta} \frac{M_1M_2}{(M_1 + M_2)^2}E,$$

where  $\theta$  is the angle between the target surface normal and the incident ions and  $\lambda(E)$  is the mean free path for ions near the target surface [54]. These calculations indicate that sputtered atoms leave the target with kinetic energies of 3 – 10 eV. Our RF-sputtering is done at pressures of 4 – 6 mTorr, and the sputtered atoms undergo collisions with gas atoms in the chamber. When they arrive at the substrate, which is located 12 – 16 cm from the target, the atoms have approximately 1 – 2 eV of energy.

The process described above is DC sputtering; in RF sputtering, the anode and cathode are reversed at radio-frequencies. In our chamber, the polarity is alternated at a standard 13.65 MHz. RF sputtering gives a greater range of material choices than DC sputtering. In DC sputtering, if a target made of an electrically insulating oxide were placed at the cathode, positive charge would accumulate on the target during the ion bombardment. This would neutralize the cathode voltage, gradually impeding



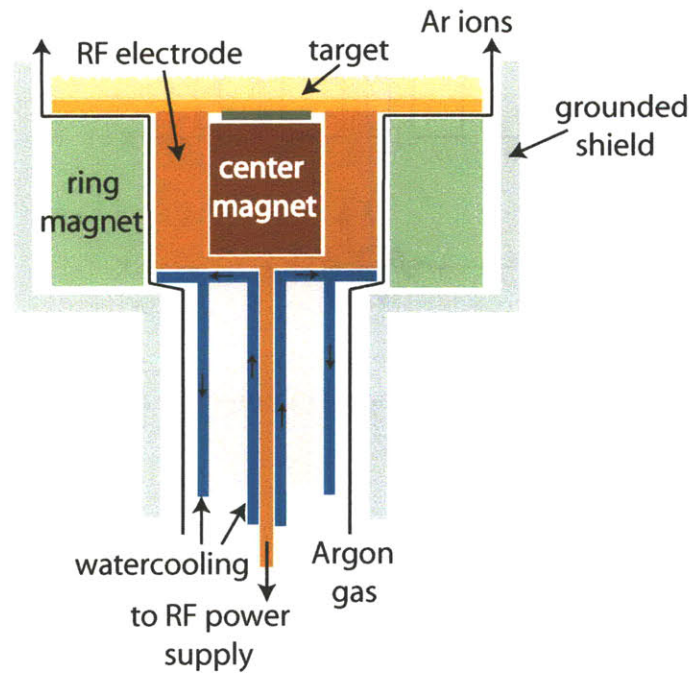


Figure 3-2: Cross sectional view of electrode assembly for RF sputtering.

the acceleration of the electrons and the subsequent ionizing collisions, and prevent DC sputtering. In contrast, with RF sputtering, the anode and cathode are reversed during each cycle, and the target is alternately bombarded with ions and electrons. The electrons neutralize the positive charge. Electron mobility is several orders of magnitude larger than ion mobility so the target will self-bias itself negatively with respect to the plasma. This negative bias attracts ions and causes the formation of the Crookes dark space as described previously in the case of DC sputtering. The choice of the 13.56 MHz frequency is important; if the polarity switching is too slow, not enough ions will reach the cathode area to form the dark space. Alternatively, if the switching frequency is increased, the negative-self bias will become larger and the sputtering rate will grow [55].

Magnetron sputtering refers to superimposing a static magnetic field on the electrode to confine the electrons to the plasma where they have a higher probability of ionizing an Ar atom [56]. This increases sputtering rates and prevents the high energy electrons from hitting the sample surface and heating the substrate. Meanwhile, the magnetic field does not significantly affect the path of the Ar gas ions, because

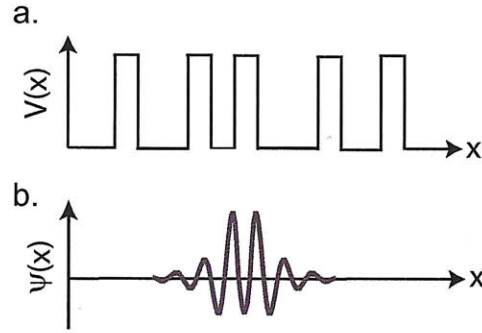


Figure 3-3: Disordered Kronig Penny model (a) potential and (b) resulting wavefunction.

their mass is orders of magnitude larger than that of the electrons. The schematic in Figure 3-2 presents a cross sectional view of the electrode in an RF magnetron sputtering system.

The structure of sputtered thin films depends on the deposition rate, the pressure of the working gas, the temperature of the substrate, and the substrate surface roughness. Optimization of these parameters for construction of an all-inorganic colloidal QD-LED will be discussed in Chapter 5.

## 3.2 Amorphous Metal Oxides

Depending on the growth process and thermal treatment of the electronic ceramic, its microstructure can range from crystalline to amorphous. In this work, we aim for amorphous ceramic charge transport layers so that charge travels through the bulk of the materials instead of along grain boundaries or defects in a crystalline or polycrystalline layers. This assures more uniform charge transport that will be immune to defects in the charge transport layers. While the band theory of (and consequently, electronic transport in) crystalline ceramics is well understood, amorphous materials lack periodic boundary conditions and long range order. In an amorphous material, the wavefunction loses phase coherence over several atomic spacings. Some understanding can be gained from modeling an amorphous material with the one-dimensional Kronig-Penny model where finite square well potentials are spaced at

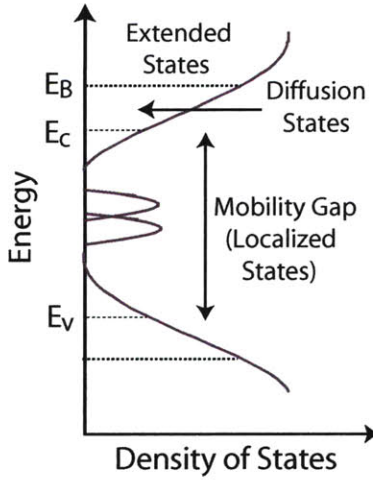


Figure 3-4: Schematic of the density of states for an amorphous solid semiconductor at different energies.

random intervals as depicted in Figure 3-3a. This potential has a wave packet solution, shown in Figure 3-3b, and given by

$$\psi \propto e^{-\gamma|x|} \sin(kx).$$

This model implies that all electronic states in an amorphous solid are localized [57]. Extending the finite square well problem to two or three dimensions however indicates that there can be both localized and extended electronic states. Figure 3-4 shows a typical electronic density of states for an amorphous solid. The extended states (or Bloch states) resemble conduction and valence bands in a crystalline material. Disorder in the solid leads to exponential band tails. Defects in the crystal result in mid-gap states. The band tail and mid-gap states are localized states and lie in a region of the band diagram known as the mobility gap.

A quantity known as the Anderson parameter quantifies the degree of electron localization of a particular state. The Anderson parameter ( $A$ ) is given by:

$$A = \frac{J}{\Delta E}.$$

$J$  is the overlap integral of periodic basis states, coupled by nearest neighbor interac-

tions. Disorder is introduced into the model by assuming that each basis state resides at a different site energy spanning a width,  $\Delta E$ :

$$J = \sum_{n \neq i} \int \psi_i^* V_n \psi_j dr^3,$$

where  $\psi_i$  electron wavefunction of the  $i$ th state,  $V_n$  is the interaction potential of the  $n$ th site. When the Anderson parameter is small (about 0.2), all states can be considered localized. In metal oxides, there is typically some critical energy,  $E_c$ , below which all states are localized. This energy is typically slightly less than  $E_B$ , the mobility edge [57].

The regimes of the band structure in an amorphous ceramic discussed above exhibit different mechanisms for charge transport. The subsequent discussion follows that of Ref.[3]. Above the mobility edge ( $E_B$ ), there is band conduction as in crystalline semiconductor, although with considerably lower mobility because of scattering events from the disorder in the lattice. Between  $E_B$  and  $E_c$ , electrons move via diffusion, and below  $E_c$  via thermally activated hopping. In the diffusion transport regime between  $E_B$  and  $E_c$ , the electronic wavefunctions are highly modulated, meaning that there are alternating regions of high and low probabilities of finding an electron. Ignoring the possible interaction of the electron and the lattice and the subsequent formation of polaron states, the mobility of an electron is  $\mu = \frac{ea^2}{kT} \nu_{el}$ , where  $a$  is the distance between the electronic wavefunction probability maxima and  $\nu_{el}$  is the frequency that an electron is found at a maximum [3].

The classical picture of the “hopping” transport mechanism is shown schematically in Figure 3-5. It assumes two localized sites, separated by energy  $\Delta E$  (Figure 3-5a). An electron localized on site 1 can polarize the lattice (Figure 3-5b). The binding energy of the electron ( $E_b$ ), which is the sum of energy required to polarize the lattice and the energy the electron gains from polarizing the lattice, is given by

$$E_b = \frac{e^2}{2r_0} \left( \frac{1}{k_\infty} - \frac{1}{k_s} \right),$$

where  $r_0$  is the radius of the electronic state, and  $k_\infty$  and  $k_s$  are the infinite-frequency and static dielectric constants, respectively. For the electron to hop to site 2, the electronic energies of the sites must be equal. Figure 3-5c schematically shows the equal energy configuration that requires least energy to achieve. This energy is referred to as the hopping activation energy and is given by

$$E_H = \frac{\Delta E}{2} + \frac{E_b}{2} + \frac{(\Delta E)^2}{8E_b}.$$

When the energy of the two sites are equal, the electron can tunnel from site 1 to site 2 with a probability,  $p = \exp(-2\alpha d)$  where  $d$  is the distance between sites and  $\alpha$  is the tunneling constant. This gives a transition rate of:

$$W = p\nu \exp\left[\frac{-E_H}{kT}\right]$$

where  $\nu$  is the phonon frequency. If two sites are close enough together, adiabatic hopping can take place, in which an electron tunnels repeatedly between site 1 and 2, aided by a resonance process. This “hopping” conduction is the primary mode of charge transport in the mid-gap defect states [3].

### 3.3 Electronic Transport in Metal Oxides

Point defects are responsible for conductivity in metal oxides. Point defects can arise from vacancies (additions) in the crystal lattice, which can be further classified into either stoichiometric or nonstoichiometric defects, or impurity dopants. Stoichiometric defects refer to situations in which the ratio of anions and cations remain the same. Such defects can result when electrically equivalent vacancies form on the cation and anion crystal sublattices (Schottky defects) or when an ion in the regular lattice migrates to an interstitial lattice location (Frenkel defect). Nonstoichiometric defects refer to situations where the composition of the crystal changes as a result of the reaction. However, in this case, as with all point defect formation, charge neutrality of the material is maintained. Ionic conductivity is largely explained by stoichiometric

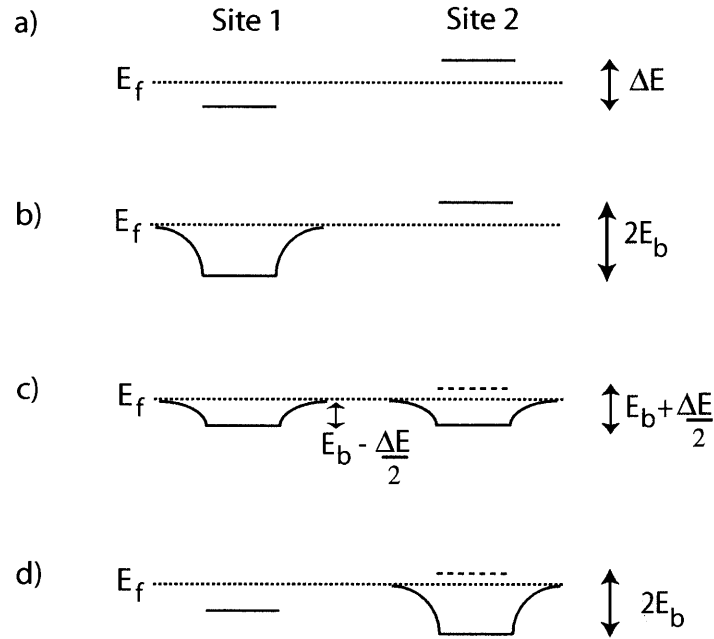
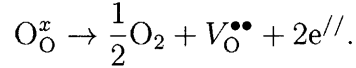


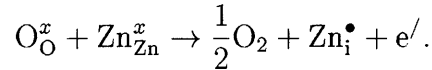
Figure 3-5: Localized electron hopping model [3].

defects, while electronic conductivity results from impurity dopants (extrinsic defects) or nonstoichiometric defects. Chapters 5 and 6 of this thesis use nonstoichiometric metal oxides as the conductive transport layer.

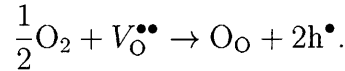
Nonstoichiometry can be controlled by tuning the oxygen partial pressure during the metal oxide growth. The extent of nonstoichiometry is determined purely by enthalpy considerations. If the Gibbs free energy associated with a perfect crystal is higher than the Gibbs free energy of the crystal containing  $n$  defects, then the crystal will contain  $n$  defects. Kröger-Vink notation is used to describe the reactions leading to nonstoichiometry. In this notation, the main symbol refers to the species involved, which can either be an element, a charge carrier (either an electron or hole), or a vacancy represented by the letter  $V$ . The subscript designates the location of the species, for which the letter  $i$  refers to an interstitial. The superscript denotes the charge ( $x$  for zero effective charge, a “/” for each negative charge, and a “•” for each positive charge). For example, at low oxygen concentrations, a material can lose oxygen and generate electrons that contribute to n-type conductivity:



This indicates that when a vacancy,  $V_\text{O}^{\bullet\bullet}$ , is created at a previously occupied oxygen site ( $\text{O}_\text{O}^x$ ), free oxygen molecules ( $\text{O}_2$ ) and two electrons ( $e^{//}$ ) result. This defect reaction leads to n-type conductivity in ZnO. Using Kröger-Vink notation, this reaction can be expressed:



In other metal oxides, high oxygen partial pressures can increase conductivity. Excess  $\text{O}_2$  can fill an oxygen vacancy, leaving two holes and contributing to p-type conduction:



This is the case for NiO, where the addition of  $\text{O}_2$  results in an increase in the p-type conductivity of NiO.

### 3.4 Dielectric Properties of Metal Oxides

In Chapter 7, we discuss devices that sandwich QDs between dielectric metal oxides such as  $\text{SiO}_2$  and  $\text{Al}_2\text{O}_3$ . The metal oxides are referred to as stoichiometric oxides, because the deviation from stoichiometry has a very weak dependence on  $\text{O}_2$  partial pressure, unlike the metal oxides described in Section 3.3. These devices with insulating metal oxides operate with high voltage, AC-drive at frequencies ranging from 1 kHz to 300 kHz. For these dielectric metal oxide layers, we are not interested in the long range motion of charge carriers (i.e. electrical conductivity), but rather in the polarization or short range displacement of bound charge in response to an electric field. Polarization of a material can result from displacement of the electron cloud relative to its nucleus (electronic polarization) or displacement of elastically bound charge relative to its equilibrium position (ionic polarization), and will depend on frequency, temperature, and the material structure. Polarization,  $P$ , can be related

to the dielectric constant of the material,  $\epsilon$ , through

$$P = (\epsilon - \epsilon_0)E.$$

Namely, the polarization is the difference between the total charge measured across a capacitor ( $\epsilon E$ ) and the charge that would be measured if the capacitor contained vacuum ( $\epsilon_0 E$ ). For all materials, the relative dielectric constant,  $\epsilon/\epsilon_0$ , decreases with increasing frequency as the ionic and electronic polarization mechanisms fail to respond to the more rapidly changing electric field. This causes some bound charge to oscillate out of phase with the applied voltage and contributes to an ac conductance in the ceramic material. The power loss in a ceramic is directly related to this AC conductance,  $\sigma_{ac}$ :

$$Power = \frac{1}{2}\sigma_{ac}E_0^2$$

where  $E_0$  is the peak electric field across the dielectric given by  $V_0/d$ . It is important to use impedance spectroscopy to measure the loss in our insulating dielectrics at different frequencies. Dielectric breakdown can result when sample dielectric losses produce more heat than can be removed from the sample. Since our QD-LEDs use relatively thin layers of metal oxides and high fields, it is also important to verify that intrinsic dielectric breakdown of these materials is not reached. Intrinsic dielectric breakdown is an avalanche process. It occurs when electrons in the conduction band of the oxide are accelerated to the point where they ionize lattice ions, resulting in more electrons in conduction band, which in turn ionize more lattice ions. Typically break down fields for sputtered metal oxides are on the order of 10 MV/cm<sup>2</sup>. In Chapter 7 we verify that these field strengths are not reached in our devices.



# Chapter 4

## Characterization Techniques

We have found that systematic and reproducible device fabrication requires careful characterization of the component materials and completed devices. In the following chapters, we will make reference to a variety of techniques. A brief description of them and their implementation is given here.

### 4.1 Thin Film Morphology

#### 4.1.1 Atomic Force Microscopy

Atomic Force Microscopy (AFM) is used to study the surface quality of the sputter-deposited metal oxides as well as the QD film thickness and quality. In AFM, a sharp Si tip, with a radius of curvature of several nanometers and attached to the end of a cantilever, is brought in close proximity with the sample surface. The cantilever is oscillated near its resonant frequency. Forces between the sample surface and the tip alter the oscillation frequency of the cantilever. Measuring this change in the oscillation frequency provides an image of the sample surface topography.

This thesis uses a Veeco Dimension series 3000 AFM. For a given sample, we typically record height and phase in  $1\ \mu\text{m} \times 1\ \mu\text{m}$  and  $10\ \mu\text{m} \times 10\ \mu\text{m}$  topography scans. These two different size scans enable us to both resolve nanometer scale features and assess the larger-area morphology of the film. The phase image, which measures the

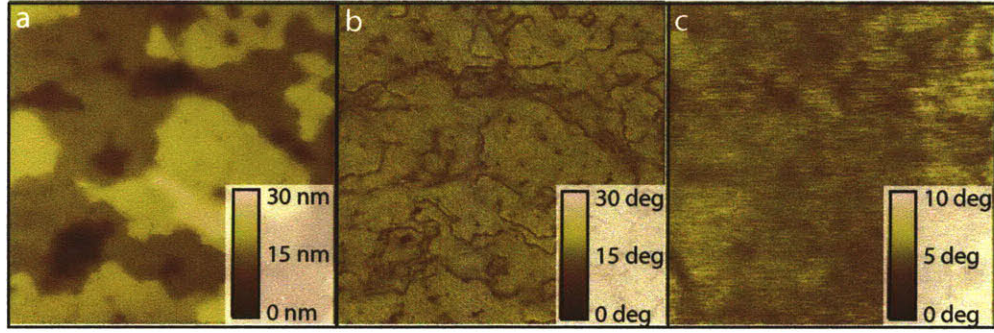


Figure 4-1: a) AFM height image of PbS/CdS QD spin cast on  $\text{Al}_2\text{O}_3$  from chloroform. b) AFM phase image of PbS/CdS QD spin cast on  $\text{Al}_2\text{O}_3$  from chloroform. c) AFM phase image of PbS/CdS QD spin cast on  $\text{Al}_2\text{O}_3$  from chlorobenzene.

lag between the set cantilever oscillation and the actual cantilever oscillation, provides excellent contrast and is sensitive to material properties such as adhesion. We also use AFM to measure the height of a spin cast QD film. To do this, we scratch the QD film and measure the step height between the metal oxide underlayer and the top of the QD film. In the case of QD and polymer composite films (See Chapter 7) that are over  $1\ \mu\text{m}$  in thickness, we use profilometry to measure step height. In profilometry, a diamond tip is lightly dragged across the surface of the sample so that variations in height can be recorded as a function of position.

To understand the relation between the properties of the thin film and the observed device behavior, it is important to characterize the thickness and surface of each layer in the device. For this, the layer of interest should be deposited with the same parameters used during the device fabrication and characterized in its actual position within the device. It is often rational to fabricate, in parallel, multiple copies of the device structure and remove one substrate after each step in the growth process to assess each layer immediately following its deposition.

Figure 4-1 highlights the importance of characterizing the QD film prior to fabricating the completed device. In this work, QDs are typically dispersed in chloroform and spin cast deposited on a metal oxide. However, while investigating a device structure that will be discussed in Chapter 7 we found that PbS/CdS QDs spin cast onto  $\text{Al}_2\text{O}_3$  from chloroform form distinct plateaus (See Figure 4-1a). While the AFM

phase image (Figure 4-1b) reveals that the QD film is complete, the height variations in the QD film on the order of 30 nm are unacceptable for efficient device operation. We explored the use of different solvents as well as different spin speeds and accelerations, and found that QDs dispersed in chlorobenzene form smooth, uniform layers on Al<sub>2</sub>O<sub>3</sub> that are suitable for use in a device (See Figure 4-1c).

### 4.1.2 X-ray Diffraction

X-Ray Power Diffraction (XRPD) can be used to analyze the crystallinity of the materials. X-rays incident on a crystal with lattice planes spaced a distance  $d$  apart are reflected off the crystal ions. The path difference between reflections from neighboring lattice planes is equal to  $2d \sin(\theta)$ . If this path difference is equal to an integer number of wavelengths, constructive interference will result. This is commonly referred to as Bragg's condition. If the material is crystalline (has good periodicity), at certain values of  $\theta$ , all the reflections will be in phase and result in discrete, sharp peaks in a collected intensity vs.  $\theta$  plot. In amorphous solids, which lack a periodic structure, these peaks are not present.

The ceramic materials used in our devices were measured using a Rigaku Powder Diffractometer, consisting of a high-powered rotating anode generator that supplies X-rays to a 250 mm Bragg-Brentano diffractometer. Some examples of these measurements are included in Section 5.1.

## 4.2 Electronic Properties of Materials

### 4.2.1 Film Conductivity

Chapters 5 and 6 discuss QD-LEDs that use conductive metal oxides to transport charge carriers. We determine the sheet resistance of our materials using the Van der Pauw technique. In this method, two characteristic sample resistances,  $R_A$  and  $R_B$ , are measured by applying a DC current ( $I$ ) between two contacts and measuring the

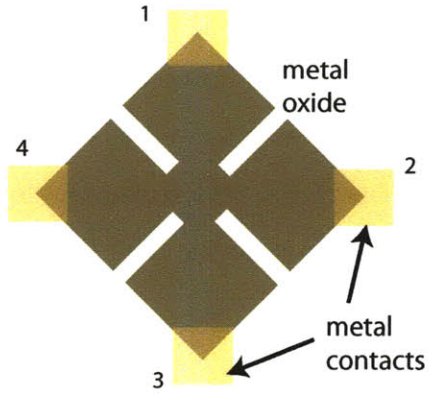


Figure 4-2: Mask design for Van der Pauw measurements.

voltage across the other two. Mathematically, this can be expressed as

$$R_A = \frac{V_{43}}{I_{12}}$$

and

$$R_B = \frac{V_{14}}{I_{23}}.$$

$R_A$  and  $R_B$  can be used to solve for the sheet resistance,  $R_s$ , with the Van der Pauw equation:

$$\exp\left(\frac{-\pi R_A}{R_s}\right) + \exp\left(\frac{-\pi R_B}{R_s}\right) = 1.$$

If the thickness,  $d$ , of a sample is known, the bulk electrical resistivity,  $\rho$ , can be calculated using  $\rho = R_s d$ . To facilitate this measurement, we designed a mask to enable metal oxide deposition in the standard clover leaf-pattern used for Van der Pauw measurements (See Figure 4-2). A second mask is then used to deposit metal on each four corners of the clover leaf pattern to make ohmic contacts with the metal oxides.

In metal oxides that do not exhibit magnetic properties, it is possible to determine the metal oxide mobility from the Hall Effect. When a conducting material carrying a constant current  $i$  is placed in a magnetic field,  $B$ , electrons (or holes) will follow a curved trajectory according to the Lorentz force,  $F_M = qv \times B$ , and pile up on one side of the resulting material. Uncompensated electrical charge will be left on the

other side of the material, resulting in the buildup of an electrical field,  $E$ . Quickly equilibrium will be reached such that the force of the electric field  $F_E = qE$  on a carrier completely counteracts the force of the magnetic field  $F_M = qv \times B$  on the carrier. After this equilibrium condition is met,  $E$  will remain constant. The Hall voltage,  $V_H$ , is equal to

$$V_H = Ed = vBd,$$

where  $v$  is the drift velocity. Since

$$v = \frac{i}{nqA},$$

where  $n$  is the bulk carrier density and  $A$  is the cross-sectional area, the sheet carrier density,  $n_s$ , is

$$n_s = nd = \frac{iB}{q|V_H|}.$$

Now, with both the sheet resistance and the Hall voltage, the mobility of the carriers can be calculated using

$$\mu = \frac{1}{qn_s R_s} = \frac{|V_H|}{R_s i B}$$

Using this technique we find, for example, that our zinc tin oxide (ZTO) films grown using the conditions described in Section 5.1 have a carrier concentration of  $10^{14} \text{ cm}^{-3}$  and a mobility of  $2 \text{ cm}^2/(\text{V} \cdot \text{s})$ .

## 4.2.2 Ultraviolet Photoelectron Spectroscopy

To design an efficient optoelectronic device, it is important to understand the energy band alignment of the component materials. The work function (WF), the electron affinity (EA) and the ionization energy (IE) are all important parameters for determining how the energy levels of materials will align at an interface and indicate how carriers will be transported.

The electron affinity is the energy needed to excite an electron from the conduction band minimum. The ionization energy is the energy needed to excite an electron from the top of the valence band. The work function is the energy between the Fermi level

and the vacuum level. The work function of a metal or the ionization energy of a semiconductor can be calculated using a technique known as Ultraviolet Photoelectron Spectroscopy (UPS). In UPS, photons of a fixed energy ( $h\nu$ ) in the deep UV (typically between 20 eV and 45 eV) bombard a sample, ejecting electrons from electronic states with different binding energies. This leads to ejected electrons with a range of kinetic energies given by  $E_k = h\nu - E_b - \phi_s$ , where  $E_b$  is binding energy of the electron, and  $\phi_s$  is the sample work function.

UPS measurements reported in this thesis were taken in an Omicron NanoTech combined deposition and analysis system shown in Figure 4-3. On this system, the UV source is a cold cathode capillary discharge lamp. Helium gas is leaked into the capillary, which is kept under high vacuum using differential pumping. Ignition is achieved by running 1000 V and 100 mA across the capillary. With a pressure of  $3 \cdot 10^{-2}$  mbar we obtain a Helium I line, which provides photons of 21.21 eV, and by decreasing the pressure to  $8 \cdot 10^{-3}$  mbar and increasing the discharge current to 200 mA, we achieve a Helium II line at 40.8 eV. The system is not equipped with a monochromator, so Helium II lines can result in an additional background in the Helium I spectrum. These generated photons are focused onto the sample, and electrons ejected from the sample are collected with a hemispherical deflection analyzer. The analyzer consists of two concentric hemispheres across which voltage is applied, causing electrons that pass between them to deflect. The kinetic energy of the electron determines how much it is deflected. Electron multipliers are located across the exit plane of the analyzer to detect the number of electrons deflected by each amount. The detector for our system provides 0.05 eV resolution.

The basic features of a UPS spectrum can be seen in Figure 4-4, which presents a Helium I spectrum of Au. The onset of counts occurs at 5.2 eV, which corresponds the work function of the Au film. This onset comes from the highest energy (least bound) electrons ejected from the sample. The peaks in the spectrum correspond to populated valence states in Au. No electronic states at energies greater than 21.2 eV can be probed (as seen by the sharp cutoff in the spectrum at 21.2 eV) because 21.2 eV is the maximum energy provided by the incoming photons.

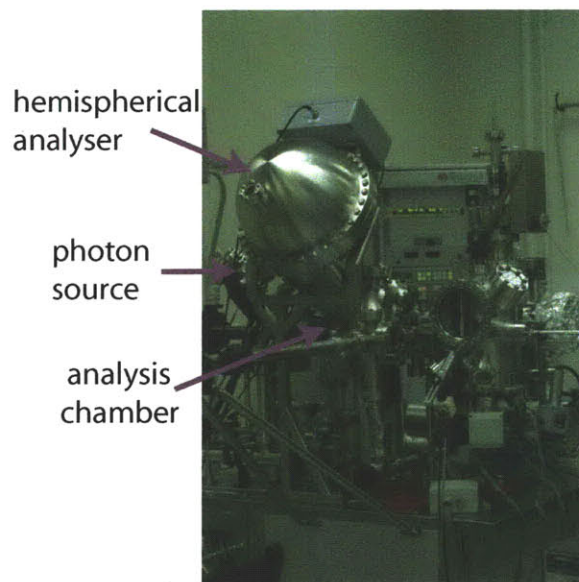


Figure 4-3: Photograph of Omicron NanoTech combined deposition and analysis system used to obtain the ultraviolet photoelectron spectroscopy results presented here.

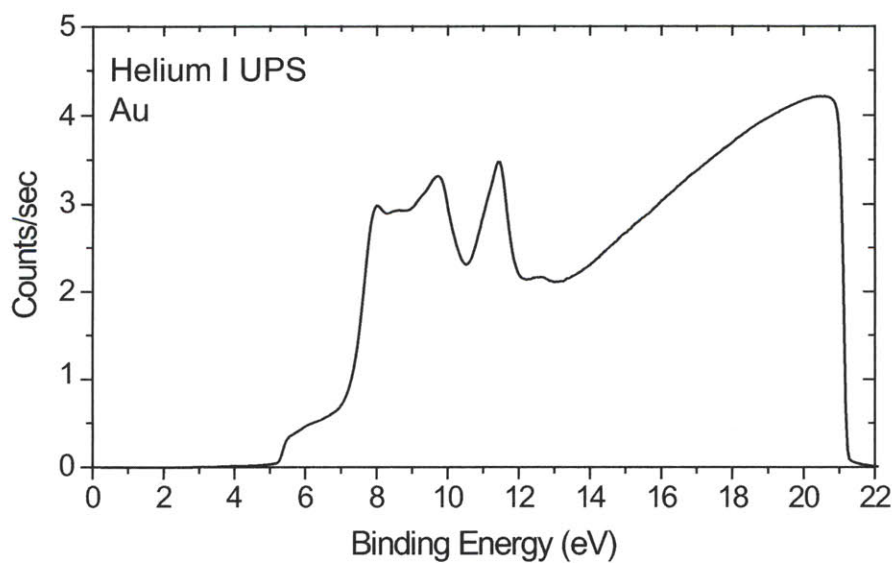


Figure 4-4: Example of data obtained from ultraviolet photoelectron spectroscopy.

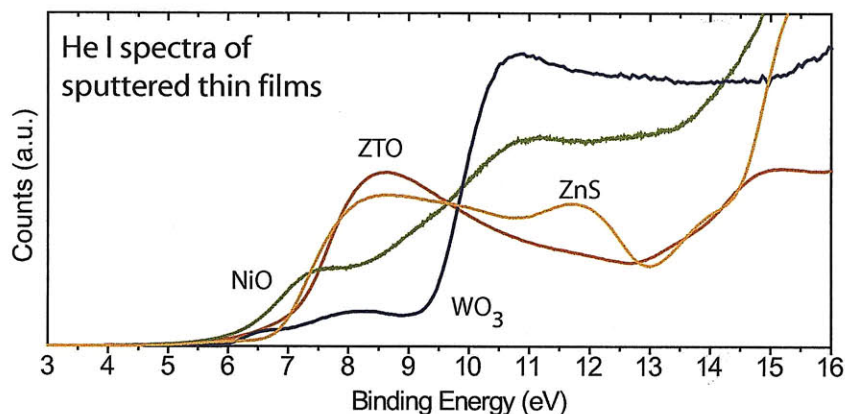


Figure 4-5: Plot of the He I ultraviolet photoelectron spectroscopy (UPS) measurements on NiO, WO<sub>3</sub>, ZTO, and ZnS thin films.

Before discussing the results of the UPS measurements on metal oxides and QDs, it is important to recognize that UPS presents several important limitations and is most valuable as a tool for looking at trends between similar material sets. As described above, UPS assumes that each incident photon transfers all its energy to one electron. This one electron picture is applicable only in cases where the ejection of one electron from a band will not substantially effect the other electrons in the band [58]. This is an acceptable assumption for post-transition metal oxides such as ZnO and SnO<sub>2</sub>, but not for transition metal oxides such as TiO<sub>2</sub>, organic materials, or QDs, where the removal of an electron can substantially change the electronic structure. Furthermore, many of the metal oxides we use in our devices are insulating. UPS measurements on insulating samples can be difficult. The incident photons are neutral particles, but they produce electrons which leave the sample surface. In an insulating sample, a positive surface charge builds up causing the electrons emitted from the sample to slow down due to the Coulomb attraction [58]. This shifts the UPS spectrum. To minimize the likelihood of this happening, we deposited the metal oxides in 20 nm thick, complete layers on top of conductive indium tin oxide (ITO) coated glass slides.

The samples remain in an inert N<sub>2</sub> environment prior to loading into an Omicron system. Both Helium I (21.2 eV) and Helium II (40.8 eV) lines from a He-discharge lamp are used for sample excitation. For accuracy, 10 scans with 0.02 eV increments are taken in succession and averaged. Figure 4-5 shows the He I spectra for the



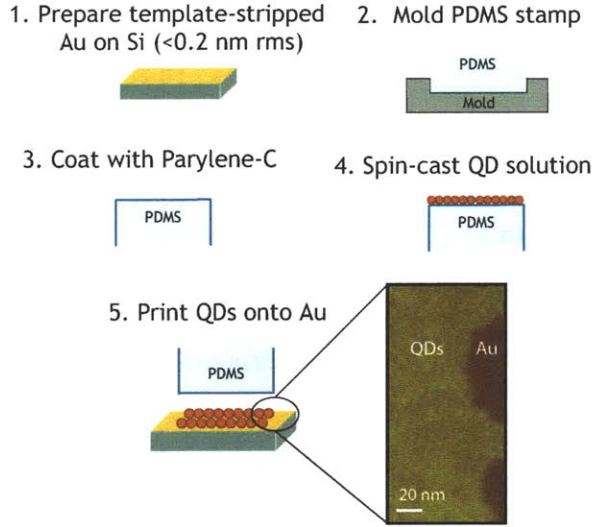


Figure 4-6: Process flow for preparing a QD film for UPS measurements. Atomic force microscopy (AFM) phase image of the edge of a ZnCdSe QD film stamped onto an ultra-smooth template stripped Au surface.

sputtered, 20 nm thick ceramic thin films deposited on conductive ITO. The IE corresponds to the location of the lowest binding energy inflection point on the UPS data. We measure IEs of  $(5.5 \pm 0.1)$  eV,  $(6.3 \pm 0.1)$  eV,  $(7.3 \pm 0.1)$  eV, and  $(8.1 \pm 0.1)$  eV for the NiO,  $\text{WO}_3$ , ZnO, and  $\text{SnO}_2$  films, respectively. As expected, the co-sputtered ZnO and  $\text{SnO}_2$  film (ZTO) has an ionization energy of  $(7.7 \pm 0.1)$  eV, in between that of the constituent ZnO and  $\text{SnO}_2$  films.

While sample preparation for the metal oxide films is relatively straightforward, sample preparation to obtain reproducible UPS measurements on QDs is not trivial, requiring a single and complete monolayer of QDs covering an area at least as large as the photon beam (here, 2 mm in diameter) on a smooth, conductive substrate. Previous efforts to prepare films of QDs for UPS involved surface treatments of the QDs to promote adhesion to the metal surface [59, 60]. We developed a novel method for depositing a monolayer of QDs on a conductive substrate that does not involve chemical treatment of the QD film, which could alter the band alignment. A schematic of the process flow is shown in Figure 4-6. A film of template stripped metal is prepared following the previous work of Blackstock *et al.* [61]. The QD solution is spin cast onto a parylene-coated polydimethylsiloxane (PDMS) stamp and contact

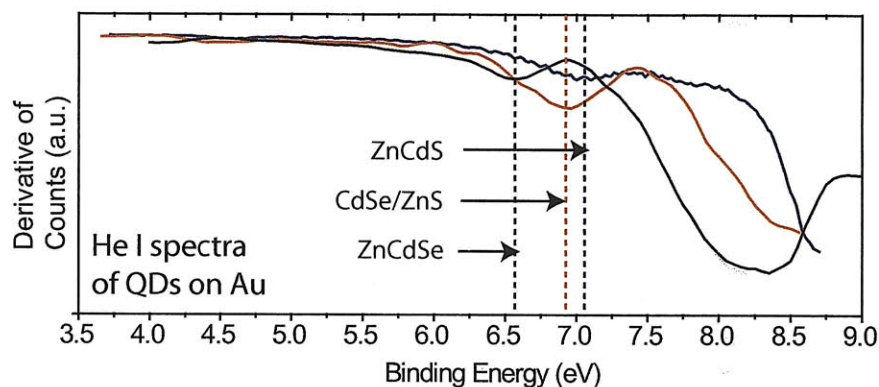


Figure 4-7: Plot of the derivative of the He I UPS spectra for several QD samples. The first minimum of these curves (indicated by the dashed lines) corresponds to the ionization energy of the sample.

printed onto the metal substrate [15], leaving a single monolayer of QDs on top of the Au surface. In Figure 4-6, the AFM phase image of the edge of a stamped QD film highlights the smooth Au surface and the close-packing of the QD monolayer. This sample preparation method was used to obtain the UPS results on QDs presented in this thesis and could be implemented with a variety metal films having a range of work functions and QDs with different capping groups in order to understand the role of the interface on the measured values.

To clearly show the IE values of different QDs, Figure 4-7 plots the first derivative of the counts of the He I UPS spectra versus the binding energy, such that the local minimum corresponds to the valence band edge. We find values of  $(7.1 \pm 0.2)$  eV,  $(6.9 \pm 0.2)$  eV, and  $(6.6 \pm 0.1)$  eV for the ZnCdS, CdSe/ZnS, and ZnCdSe QDs, respectively. The 6.9 eV value for the core/shell CdSe/ZnS QDs likely represents an average of the ZnS shell and CdSe core contributions to the valence states, which is in agreement with our UPS measurements of ZnS thin films,  $(7.4 \pm 0.1)$  eV, and CdSe QDs,  $(6.6 \pm 0.1)$  eV.

The electron affinity (EA) of the materials is calculated by adding the band gap to the measured ionization energy. We determine the band gap of the ceramics by measuring the absorption onset of a film of the material grown on quartz using a CARY 500i spectrophotometer. We approximate the electronic band gap of the QDs by measuring their photoluminescence (PL) spectrum, which gives the optical

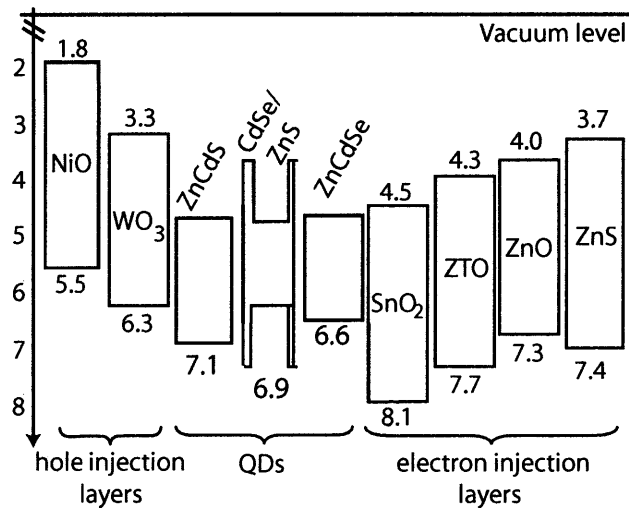


Figure 4-8: Valence and conduction band energies from UPS and optical absorption measurements.

bandgap, and adding to this value 100 meV to account for the approximate exciton binding energy in a QD [62]. We summarize this IE and band gap data in Figure 4-8.

## 4.3 QD-LED Characterization Techniques

This section describes several techniques for characterizing QD-LEDs that will be referred to routinely in Chapters 5-7.

### 4.3.1 Photoluminescence Measurements

As discussed in Chapter 2, studying the luminescence spectrum of QDs can be useful in understanding the effect of an applied electric field on the QD device. For most photoluminescence (PL) spectra, we use a  $\lambda = 337$  nm N<sub>2</sub> pulsed laser source to excite a sample at a 45 degree angle and collect the luminescence normal to the sample using a Princeton Instruments Acton Standard spectrometer. A higher intensity is often needed to observe defect state emission (See Chapter 7). For this we use the frequency doubled operational parametric amplifier output of a titanium-sapphire laser system. The frequency doubled output of an ultra-fast titanium-sapphire system is also used for the time resolved measurements where the PL is detected using a 10 ps resolution

streak camera.

### 4.3.2 DC Electroluminescence Characterization

All the measurements discussed below were taken in air on unpackaged devices. When testing QD-LEDs, we record three important data sets: the current-voltage characteristics, the external quantum efficiency (EQE), and the electroluminescence (EL) spectrum.

The current density vs. voltage ( $J$ - $V$ ) characteristic was recorded using a LabView controlled Keithley 2602 current/voltage source-meter. The emitted light is collected by a Newport UV-818 Si photodetector (in the case of visible wavelengths) or a Newport 1100-NIR Ge photodetector (in the case of infrared wavelengths). The EQE, measured at the same time as the  $J$ - $V$  curve, is defined as the ratio between the number of photons emitted per second and the number of electrons passing through the device per second. The EQE is calculated by

$$\text{EQE}(\%) = 100 \cdot g \cdot \frac{(I_p - I_d) \lambda}{R} \cdot \frac{q}{hc} \cdot \frac{1}{i},$$

where  $I_p$  is the photocurrent detected using a calibrated photodetector from the device EL,  $I_d$  is the dark current registered by the photodetector when the device is not operating, and  $R$  is the responsivity of the detector for the peak wavelength of the device,  $\lambda$ .  $I_p$  is the current through the device,  $q$  is the electron charge,  $h$  is Planck's Constant, and  $c$  is the speed of light.  $g$  is a configuration factor that accounts for the geometry of the light collection setup, in which the QD-LED is not flush with the photodetector face. Given that thin film LEDs are assumed to be Lambertian emitters, with an emission intensity profile,  $I = I_0 \cos(\theta)$ , we can calculate the ratio of the power measured to the total power emitted from the device to be

$$g = \frac{a^2}{R^2 + a^2},$$

where  $R$  is the perpendicular distance between the photodetector and the LED, and

$a$  is the radius of the photodetector.

The EL spectrum ( $EL(\lambda)$ ) is taken with an Princeton Instruments Acton Standard spectrometer. From the EQE and the EL spectrum, it is possible to calculate the device brightness as discussed in the following subsection.

### 4.3.3 Luminance and Chromaticity Coordinates

Luminance is given in units of candelas per square meter ( $Cd/m^2$ ). A candela (Cd) is a measure of luminous intensity,  $L$ , and is calculated using

$$L = 683.002 \cdot i \cdot EQE \int EL(\lambda)S(\lambda)d\lambda,$$

where EQE and  $i$  are the device efficiency and current at a particular voltage.  $S(\lambda)$  refers to the Commission Internationale de l'Eclairage (CIE) sensitivity curve for the human eye. Luminance is then calculated by dividing the luminous intensity by the active device area and  $\pi$ .

When evaluating color purity of an LED, it is useful to calculate the CIE chromaticity coordinates ( $x$  and  $y$ ) so that the emission color can be mapped on the chromaticity diagram presented in Figure 1-2. First, we calculate the overlap of CIE color matching functions ( $\bar{x}(\lambda)$ ,  $\bar{y}(\lambda)$ , and  $\bar{z}(\lambda)$ ), which are related to the amount of red, green, and blue in spectrum, with the luminescence spectrum ( $EL(\lambda)$ ) to find the tristimulus values  $X$ ,  $Y$ ,  $Z$ :

$$X = \int EL(\lambda)\bar{x}(\lambda)d\lambda, Y = \int EL(\lambda)\bar{y}(\lambda)d\lambda, Z = \int EL(\lambda)\bar{z}(\lambda)d\lambda.$$

The chromaticity coordinates are then given by

$$x = \frac{X}{X + Y + Z}, \quad y = \frac{Y}{X + Y + Z}.$$

We can also measure the luminance and chromaticity coordinates directly using a chromaticity meter. The luminance results in Chapter 7 are obtained using a Konica-Minolta CS-200 luminance and color meter.

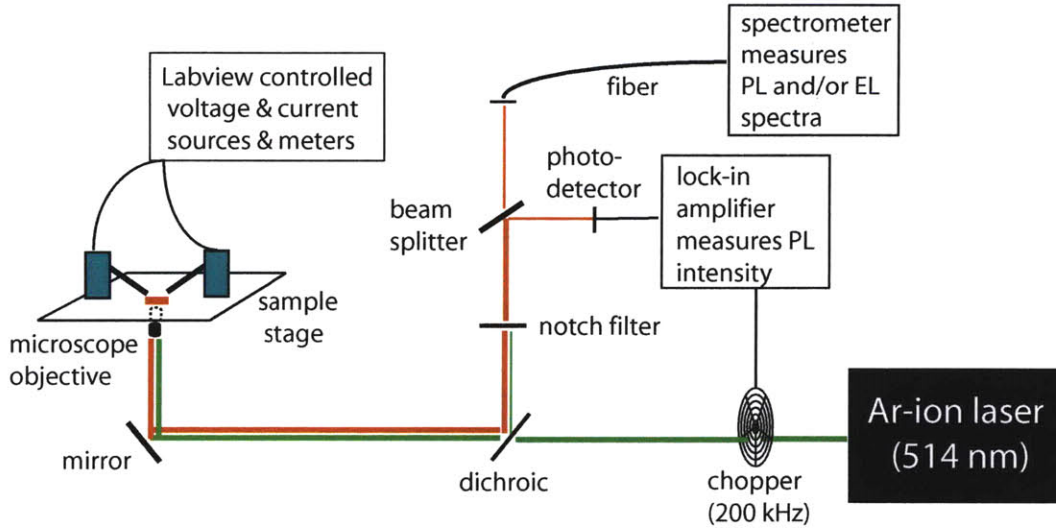


Figure 4-9: Schematic of measurement to simultaneously measure the electroluminescent (EL) and photoluminescent (PL) response of the QD-LED. This setup is used to obtain PL quenching data as well as the effect of an electric field on the PL and EL spectra (See Section 6.3).

#### 4.3.4 Combined Electroluminescence and Photoluminescence Measurements

To assess some of the mechanisms contributing to device inefficiency, it is useful to simultaneously optically and electrically excite the QDs. For example, as discussed in Section 6.3, by recording the quenching of the PL response as a function of applied electric field, we gain insight into the prevalence of exciton dissociation and Auger non-radiative recombination events. Figure 4-9 shows schematically the setup we use for combined PL and EL measurements. A  $\lambda = 514\text{ nm}$  laser beam, chopped at 200 kHz, is focused onto the QD-LED that can be electrically biased. The PL (and EL, if the QD-LED is biased above turn on) signal from the QDs is then split and collected by a photodetector and a spectrometer. The photodetector is locked-in to the chopped laser signal so it measures only the PL intensity. The spectrometer measures the combined PL and EL spectra. For instance, in Section 6.3, we explore how this spectral data enable us to assess the amount of phonon coupling.

### 4.3.5 Time Resolved Electroluminescence

For measurements of QD-LEDs driven with an AC pulse at kilohertz frequency, a different setup for measuring the time-resolved EL is required. The Newport UV-818 Si photodetector used for the measurements described above has a large area making it ideal for accurate measurement of device luminescence but limiting its rise time to  $2\ \mu\text{s}$ . To measure the time response of the electroluminescence, we instead use a surface-mounted Thor Labs high speed Si detector biased at 20 V to obtain a time response of 1 ns. The output current of the Si-detector is dropped across a  $1\ \text{M}\Omega$  resistor to produce a mV-level signal that can be read by the oscilloscope. To prevent AC coupling into the photodetector, the photodetector is electrically grounded to and shielded in an aluminum box. The photodetector is optically aligned with 5 mm diameter hole, covered with a grounded copper wire mesh, that blocks 60% of electromagnetic radiation.





# Chapter 5

## Diode QD-LED

This chapter demonstrates that QD-LEDs containing metal oxide charge transport layers can be systematically designed. We outline four important guidelines for the choice and preparation of these inorganic charge transport layers. First, deposition conditions must be chosen to enable formation of a semiconducting metal oxide layer on top a QD film without damage to the QDs. Second, smooth and amorphous metal oxide layers reduce the chance of electrical shorts or formation of preferred current channels through the device structure. Third, the hole transport layer (HTL) and the electron transport layer (ETL) should be chosen to have similar energy band offsets to the QDs so that electron and hole injection into the QD layer is balanced. Fourth, luminescence quenching of the QDs can be reduced by depositing semiconducting metal oxides with low free carrier concentrations adjacent to the QD film.

### 5.1 The first QD-LED using metal oxide based transport layers

The QD-LED geometry we investigate is shown in Figure 5.1. It consists of an indium tin oxide (ITO) anode, deposited commercially or in-house onto a glass substrate, a p-type metal oxide layer, a QD luminescent layer, an n-type metal oxide layer, and a metal cathode. As discussed in Chapter 3, RF magnetron sputtering is selected

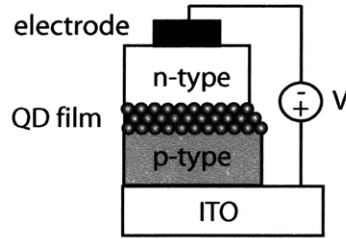


Figure 5-1: Schematic of the basic QD-LED structure.

as the deposition method for the metal oxide transport layers since it is a physical vapor deposition (i.e. non-chemically reactive) technique that can be performed at low power and at room temperature. The p-type layer is deposited first because many common p-type metal oxides such as NiO or CuO require the addition of  $O_2$  to achieve p-type conductivity (Section 3.3). This addition of  $O_2$  is achieved by maintaining a relatively high  $O_2$  partial pressure during sputtering that can cause oxidation of QDs or QD capping ligands, which could be detrimental for QD luminescence efficiency. QDs are then spin cast onto the p-type layer from solution. The n-type layer is sputter-deposited in an Ar environment to minimize the  $O_2$  exposure of the QD film. The top contact is a 100 nm thick evaporated metal such as Ag, Au, or Al.

To define the metal oxide layers and the electrodes, we use shadow masks on top of blanket-deposited ITO. In QD-LEDs with organic based charge transport layer, the ITO layer is typically photolithographically patterned or sputtered-deposited through shadow mask to define bottom electrodes. This introduces a step height on the order of 100 nm between the top of the ITO pattern and the glass substrate. In organic-based QD-LED structures, poly(3,4-ethylenedioxythiophene) poly(styrenesulfonate) (PEDOT:PSS) is often spin cast across the patterned ITO to simultaneously aid hole injection and smooth out the ITO-glass step. In contrast, QD-LEDs with inorganic layers do not incorporate PEDOT:PSS and are therefore designed to avoid the abrupt height change at the ITO/glass step that increases the possibility of cracks and electrical shunts in the subsequently deposited metal oxide layers. Shunts can be manifested by sparking at the point of overlap between the bottom and top electrodes and can lead to no device emission. In our metal oxide based QD-LEDs we use a series of

progressively smaller area mask sets to define each layer so that no metal oxide is deposited across a step. A typical mask set provides ten  $1\text{ mm} \times 2\text{ mm}$  pixels per  $12.7\text{ mm} \times 12.7\text{ mm}$  substrate. This masking scheme, while practical in a laboratory setting, is not directly transferable to a commercial display product, where individual pixels would have to be individually addressed to be driven from an active matrix backplane. Nonetheless, the commercialization of organic LEDs (OLEDs) has led to the development of backplanes that could be used in conjunction with inorganic metal oxide based QD-LEDs but are cost prohibitive to implement in a small scale laboratory setting.

The details of the first-ever demonstration of QD-LEDs with metal oxide charge transport layers are presented in Caruge *et al.* [63]. Following previous work on NiO as a hole transport layer (HTL) [64], we deposit a 20 nm thick film of NiO on the ITO. The resistivity of the NiO film is tuned to  $5\ \Omega \cdot \text{cm}$  by adjusting the  $\text{O}_2$  partial pressure during the RF magnetron sputtering process. X-ray diffraction and hot probe measurements indicate that as-grown NiO films are amorphous and p-type. Atomic force microscope (AFM) characterization of the NiO layer on top of the ITO electrode reveals a root mean square roughness of less than 0.5 nm, which enables deposition of a smooth multilayer of QDs onto the NiO.

The luminescent layer of these first metal oxide based QD-LEDs consists of ZnCdSe alloyed QDs. The batch of these QDs used to obtain the results reported in this section had a solution photoluminescent quantum yield of  $(50 \pm 10)\%$ , an emission peak at wavelength  $\lambda = 638\text{ nm}$ , and a full width at half-maximum (FWHM) of 40 nm. The QDs are spin-coated onto the NiO substrate so as to form a  $(30 \pm 5)\text{ nm}$  thick film consisting of three or four close-packed QD monolayers. We choose ZnCdSe cores over more traditional CdSe/ZnS core shell QDs due to their ease of production. Further, because ZnCdSe alloyed QDs are not overcoated with a wide band gap ZnS layer, they should enable easier charge injection into the QDs. In this study, our highest electroluminescence efficiencies are indeed measured for QD-LEDs containing ZnCdSe QDs; however, devices containing CdSe/ZnS QDs show efficiencies within an order of magnitude.

This QD multilayer is in contrast to organic-based QD-LEDs that use only a monolayer of QDs. The need to move to thicker QD films in this initial metal oxide QD-LED effort can be largely explained by layer morphology and conductivity. In the case of both metal oxides and organic small molecules, the material deposited directly on top of a QD monolayer will fill voids in the monolayer, resulting at times in an interface between the n- and p-type layers of the device. This interface can lead to the formation of an exciton on one of the organic films, which can then diffuse, energy transfer to an adjacent QD, or recombine (perhaps emitting light characteristic of the organic material on which the exciton is formed). In contrast, if the n- and p-type metal oxides are in contact, no exciton is formed, and the pn junction simply provides a highly favorable current pathway to circumvent the more resistive QD layer. In an inorganic QD-LED, the QD layer must therefore be complete. At the same time, if the QD layer becomes too thick, the resistivity of the device is too large. Treated QD films, in which the oleic and TOP capping groups have been replaced with shorter ligands, can radically change the conductivity of the QD film and most likely alter the preferred layer thickness. However, for the simplest case of a spin cast QD layer with its native capping groups, we find that three to four QD layers is optimal. Figure 5-2a shows an AFM phase image of a typical complete, spin-cast layer of ZnCdSe QDs on NiO, such as one used in a QD-LED.

For the electron transport layer (ETL), we select a 50 nm thick, optically transparent film of n-type, co-deposited ZnO and SnO<sub>2</sub> (ZTO), with a resistivity of 10 Ω · cm. Whereas pure ZnO or SnO<sub>2</sub> films tend to be polycrystalline with pronounced grain boundaries, AFM and X-ray diffraction measurements presented in Figure 5-2 indicate that ZTO films are relatively smooth (with less than 0.5 nm rms roughness) and amorphous, reducing the likelihood of morphologically-induced electrical shorts in the device.

Our choice of ZTO also reflects the requirement that the ETL be sputtered directly onto the QDs without damaging them. Introducing O<sub>2</sub> into the sputtering gas could oxidize the organic ligands capping the QDs and produce trap sites that facilitate non-radiative recombination of QD excitons. ZTO is deposited on the QDs

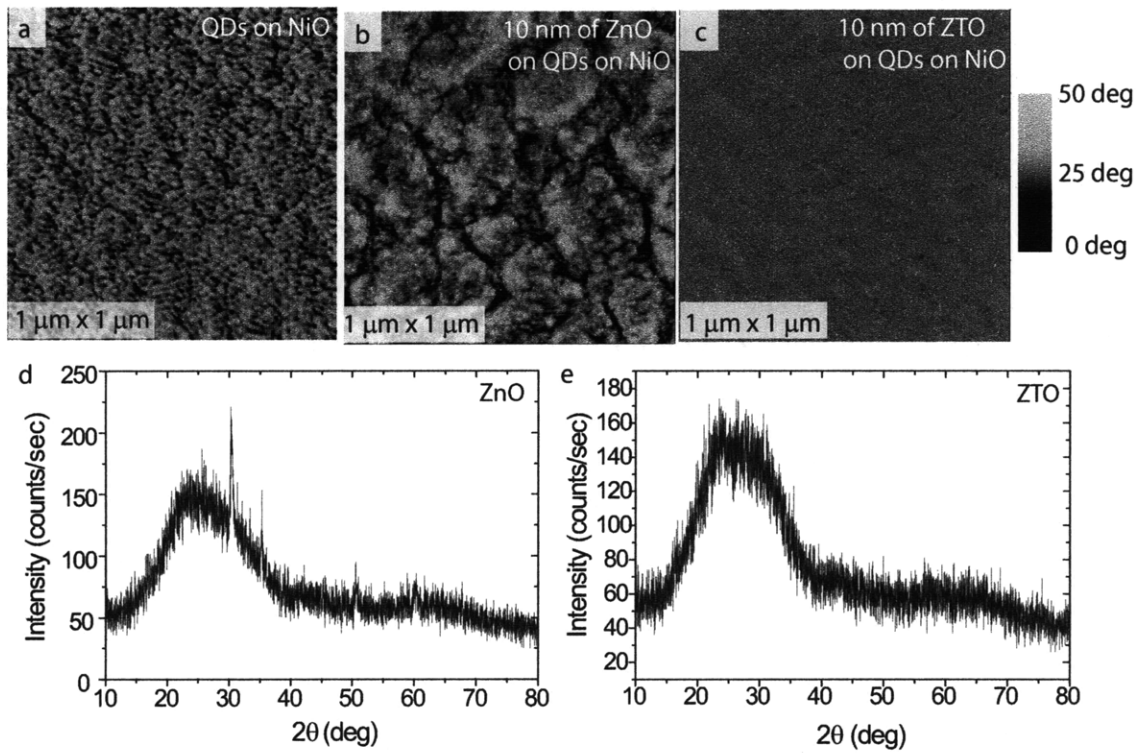


Figure 5-2: AFM phase images measurements showing the QDs spin cast onto the NiO (a), 10 nm of ZnO sputter-deposited on the QD film (b), and 10 nm of ZTO sputter-deposited on the QD film (c). XRD scans of ZnO (d) and ZTO (e) showing that ZnO is polycrystalline while ZTO is amorphous.

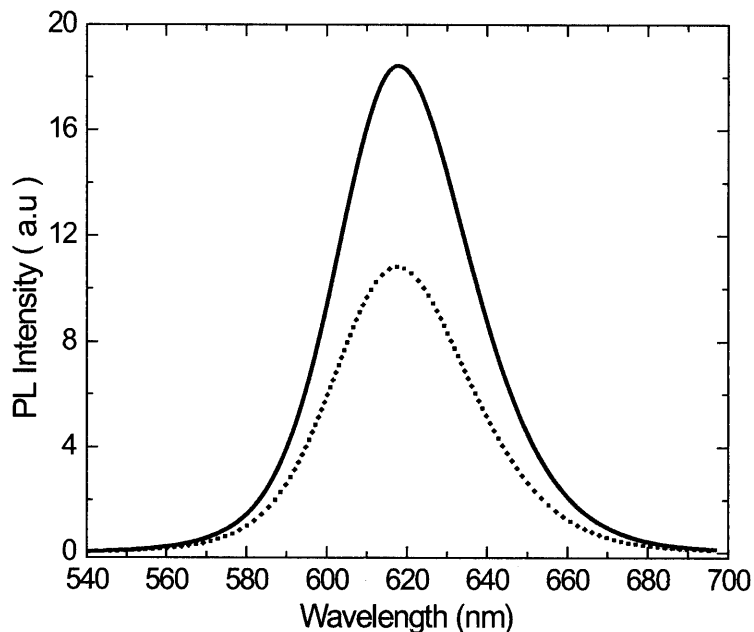


Figure 5-3: Photoluminescence (PL) spectra before (solid line) and after (dotted line) deposition of a 120 nm thick ZTO layer onto ZnCdSe QDs on NiO.

by simultaneously sputtering ZnO at 15 W and SnO<sub>2</sub> at 9 W in a pure argon environment at 5 mTorr pressure. The ZnO to SnO<sub>2</sub> ratio determines the film conductivity, eliminating the need for excess oxygen in the sputtering process. These powers correspond to a combined deposition rate of 0.2 Å/s, which is sufficiently slow to minimize damage to the QD underlayer.

To determine whether the ZTO deposition causes physical damage to the QDs, we compare the photoluminescence (PL) intensity from QDs on NiO and from QDs embedded in a NiO/QD/ZTO structure. As shown in Figure 5-3, we observe a 40 % drop in the QD PL intensity as a result of the ZTO deposition, which indicates that sputtering the ETL on the QDs largely preserves the passivating ligands. In fact, much of the decrease in QD luminescence can be attributed to the additional quenching by the free carriers in the ZTO as discussed in Section 5.3.

A 40 nm thick silver cathode is then thermally evaporated through a shadow mask onto the ZTO at a rate of 1.5 Å/s to allow electron injection into the conduction band of the ZTO layer.

All our QD-LEDs are tested in air over several days. The devices were tested as-

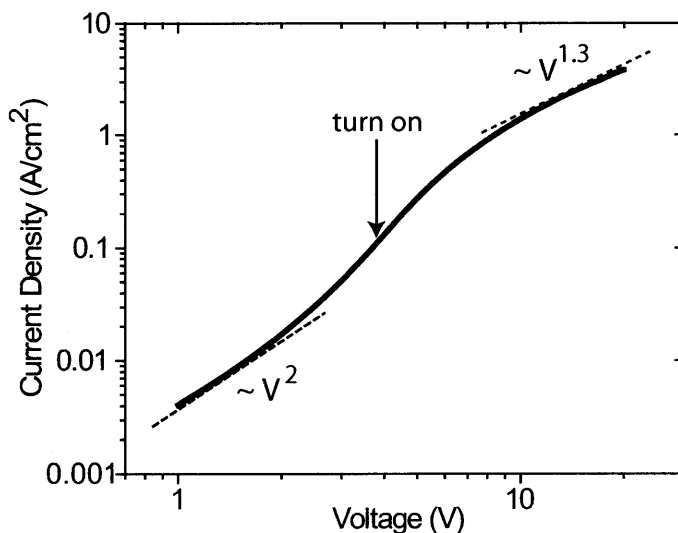


Figure 5-4: The current density vs. voltage ( $J$ - $V$ ) log log plot for a QD-LED described in the text. Three different regimes of conduction are clearly visible.

made, without additional environmental packaging, and were stored in atmospheric conditions in between experiments. Figure 5-4 shows the forward biased current density vs. voltage ( $J$ - $V$ ) log-log plot for the QD-LED described above. The  $J$ - $V$  slope of 2.0 between 1 V and 3 V is indicative of space charge limited conduction for one of the carriers. The increase in the  $J$ - $V$  slope coincides with the first observation of QD-LED electroluminescence at 3.8 V, and is therefore associated with the onset of both electron and hole injection into the QDs. The elevated current and  $J$ - $V$  slope of 1.3 for applied voltages greater than 10 V is a signature of the combined  $J$ - $V$  characteristics for injected electrons and holes, with one or both of the carriers tending to ohmic conduction.

Figure 5-5a shows a characteristic QD EL peak centered at  $\lambda = 642$  nm with a FWHM of 38 nm. The similarity between the EL spectrum and the PL of QDs in solution (FWHM = 40 nm) indicates that the device emission is due entirely to the QDs. Figure 5-5b shows external quantum efficiency (EQE) of the QD-LED as a function of current density, which, at its maximum of 0.09%, is almost two orders of magnitude higher than previous reports of devices with QDs embedded between doped inorganic transport layers. At 6 V and 0.46 A/cm<sup>2</sup> pixel brightness is

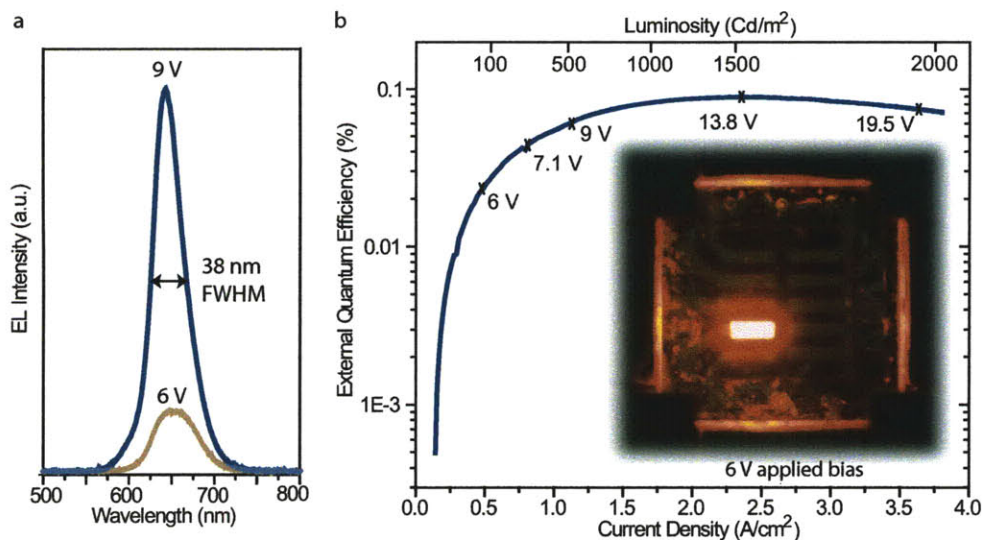


Figure 5-5: a) Electroluminescence (EL) spectra of the QD-LED at 6 V (0.46 A/cm<sup>2</sup>) and 9 V (1.14 A/cm<sup>2</sup>) applied bias. (b) Plot of the QD-LED external quantum efficiency (EQE) measured from the front face of the device as a function of current density. A maximum EQE of 0.09% and a luminance of 1500 Cd/m<sup>2</sup> is reached at 13.8 V, (2.33 A/cm<sup>2</sup>). The inset shows a photograph of a bright and uniform pixel at 6 V applied bias. Significant amount of additional light is guided through the glass substrate and emitted at the four substrate edges, as evident from the photograph. Presence of the edge-emitted light is not reflected in the stated EQE measurements.

uniform at 74 Cd/m<sup>2</sup>, with emission entirely from the QDs. Standard video brightness (200 Cd/m<sup>2</sup>) occurs in our device at 7.15 V and 0.71 A/cm<sup>2</sup>. The peak brightness is measured to be 1950 Cd/m<sup>2</sup> at a current density of 3.73 A/cm<sup>2</sup> (19.5 V), and the peak luminescence efficiency is 0.064 Cd/A at a current density of 2.33 A/cm<sup>2</sup> (13.8 V). Comparable brightness and *J-V* characteristics are observed when the devices are tested after being stored in air for four days, in contrast to unpackaged organic QD-LEDs that can not withstand prolonged atmospheric exposure.

To verify that this QD-LED operates primarily via direct charge injection and not energy transfer, we perform time resolved PL measurements on the charge transport layers and the QDs. No PL signal is measured from optically excited 50 nm thick NiO and ZTO thin films indicating that non-radiative processes faster than 10 ps dominate exciton relaxation in the metal-oxide transport layers. This implies that the dominant mechanism for generating EL in our QD-LEDs is direct charge injection into the QD



layer rather than energy transfer from weakly-bound metal-oxide Wannier excitons to excitons in the QDs.

To further understand the time scales associated with these QD-LEDs, we measure the EL response to a sinusoidally modulated drive voltage. The amplitude of the modulation in the light output plotted in Figure 5-6 shows a  $-3$  dB frequency of 1.2 MHz, which corresponds to QD-LED response faster than 1  $\mu$ s. This RC-time constant was measured by applying a fixed DC bias,  $V_{DC}$ , to the device using a Keithley 2602 and a sinusoidal modulated voltage,  $V_m$ , using an Agilent 3250A waveform generator, such that the total applied voltage is given by  $V = V_{DC} + V_m \sin(\omega t)$ . Frequency  $\omega$  was varied, and the decrease in the modulation of the EL intensity is recorded.

We next consider whether electrically pumped lasing of QDs in QD-LED structures is feasible. To achieve biexciton lasing, the exciton generation rate must compete with non-radiative processes such as the Auger decay. With time resolved PL we measure a biexciton lifetime of 1.3 ns for the ZnCdSe QDs. We also find that these QD-LEDs sustain steady-state current densities of up to 3.5 A/cm<sup>2</sup>. Assuming equal hole and electron currents, that all charge carriers flow through the QDs and not the ligands, an exciton lifetime of 5 ns in a QD in a close-packed film, a QD radius of 4 nm, and a ligand length of 1 nm, this current density corresponds to a carrier injection rate of  $10^7$  carriers per second per QD and a maximum exciton density per QD of 0.1. To achieve the onset of the biexciton lasing action, we approximate that an average charge carrier injection rate of nearly  $10^9$  electrons per second per QD is needed, which is 100 times higher than the maximum steady-state current density obtained in this study. This high carrier density in the QD layers might necessitate even larger drive currents, which further emphasizes the need for robust inorganic devices as the first step in the demonstration of electrically pumped colloidal QD lasers.

This work demonstrates that metal oxides and colloidal QDs can be combined to fabricate LEDs with uniform pixel emission of saturated color and high peak luminance. The brightness of the devices reported here matches that of the best organic-based QD-LEDs and brings benefits of improved shelf-life robustness inherent in the

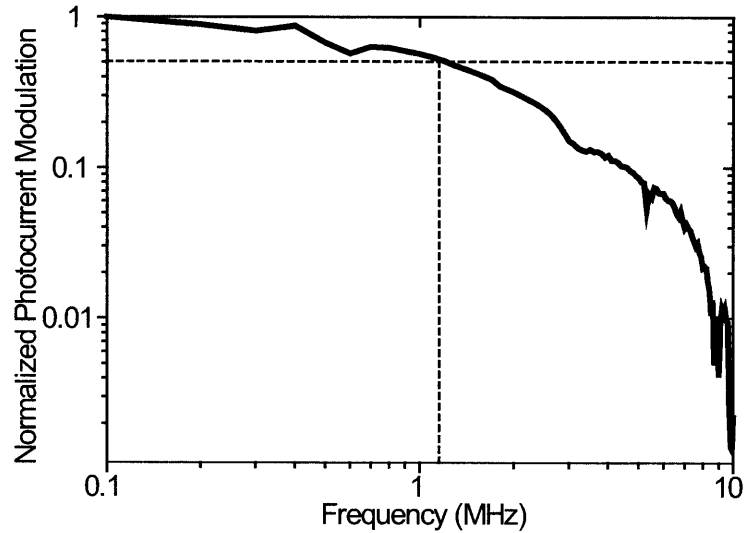


Figure 5-6: Plot of the modulation in QD-LED electroluminescence (EL) intensity as a function of frequency. The half-power point of the curve corresponds to the  $-3$  dB cutoff frequency of 1.2 MHz.

environmental stability of metal oxide charge transport layers. However, the efficiency of these QD-LEDs with p- and n-type inorganic charge transport layers is significantly reduced by charging processes. For one, the relatively high carrier concentrations in metal oxide transport layers lead to luminescence quenching of the adjacent QDs, caused by non-radiative energy transfer between the QDs and the conductive surface. Second, QD-LEDs incorporating p- and n-type metal oxides operate by direct charge injection into the QD film making energy band alignment of the component materials important so as to maintain charge balance between the injected holes and electrons. In this first metal oxide-based QD-LED structure, for example, injection of holes from the p-type NiO into the QDs is more difficult than electron injection from the n-type zinc tin oxide (ZTO) causing a significant build-up of electrons at the emissive QD multilayer, located between the two ceramics (See Figure 5-7). Charging of the QDs can lead to an increase in Auger non-radiative recombination. In following Sections, we demonstrate that inorganic p- and n-type charge transport materials can be systematically selected to counteract the charging processes that cause inefficiency in metal oxide based QD-LEDs and achieve red, green, and blue QD emission in all-inorganic structures.

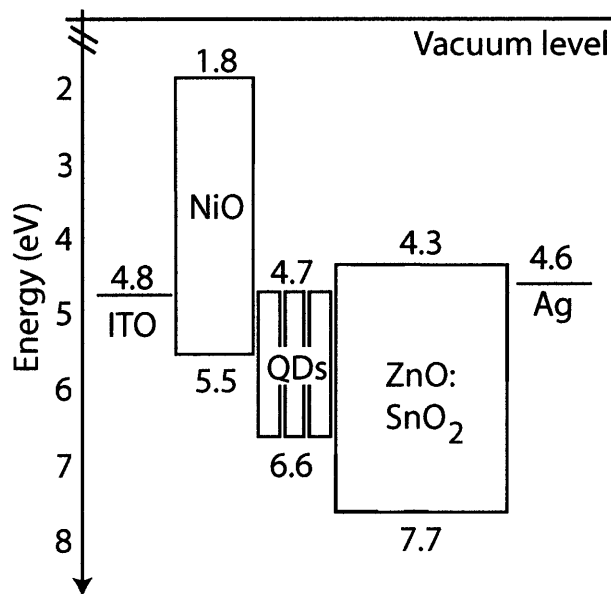


Figure 5-7: A band diagram determined from ultraviolet photoemission spectroscopy measurements and optical absorption measurements giving the approximate ionization energies and bandgap of the QD-LED materials.

## 5.2 Demonstrating red, green, and blue emission

One main advantage of using QDs as the luminescent medium in LEDs is the possibility for multicolor displays or white lighting, which requires excitation of at least red, green, and blue QDs. However, the sensitivity of QD-LEDs with metal oxide charge transport layers to energy band alignment makes multicolor QD excitation particularly challenging. The ZnCdSe QDs used in the initial device demonstration (See Section 5.1) are efficient deep-red lumophores, but the ZnCdSe chemistry is not suitable for wavelengths shorter than  $\lambda = 560$  nm. And, while the standard CdSe/ZnS core-shell QD can be synthesized to emit throughout the visible spectrum, ZnSe/CdSe/ZnS and ZnCdS QD chemistries offer more efficient emission in the green and blue, respectively. Chapter 2 explained that the energy levels of a QD are determined by the chemistry as well as the size of the QD, so we expect QDs with different crystal compositions to have different valence band energies. Indeed, in Chapter 4 we experimentally determined the energy bands for the ZnCdS, CdSe/ZnS, and ZnCdSe QDs and found that the location of their valence bands ranged over 0.5 eV (See Figure

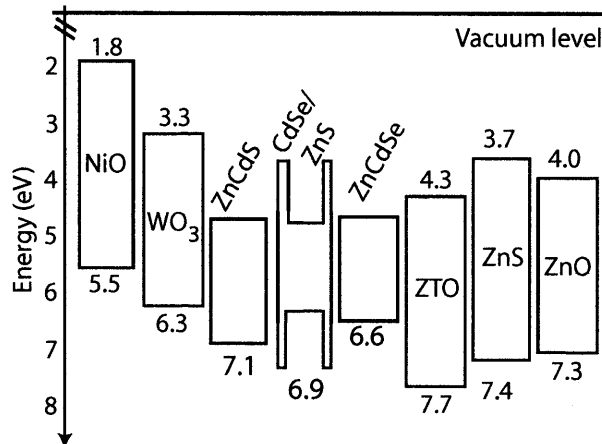


Figure 5-8: Summary of the energy band values obtained from the UPS and band gap measurements.

5-8). In this Section, we demonstrate that understanding the location of the QD band energies enables informed selection of metal oxides for electron and hole injection and systematic design of red, green, and blue emitting QD-LEDs.

The schematic diagram of energy levels presented in Figure 5-8 shows that the valence band of ZnCdS is at 7.1 eV, which is 0.5 eV lower in energy than the ZnCdSe QDs used in the initial metal oxide-based QD-LED device. Since holes already face a 1.1 eV barrier to injection between the ZnCdSe QDs and the NiO, it is not surprising that no electroluminescence (EL) is observed from blue-emitting ZnCdS QDs when they replace the red-emitting ZnCdSe QDs in a NiO/QD/ZTO device structure. To demonstrate that the absence of EL is indeed the result of the increased energy band offset, we replace the NiO layer with a WO<sub>3</sub> layer that is reported to improve hole injection with an IE located 0.8 eV below that of NiO. The EL spectra in Figure 5-9 show the blue ZnCdS and green ZnSe/CdS/ZnS QD emission made possible by the replacement of NiO with WO<sub>3</sub>.

### 5.3 Improving QD-LED efficiency

The results presented in Section 5.2 demonstrate that energy band alignment between the metal oxides and the luminescent QD film is critical for efficient device operation.

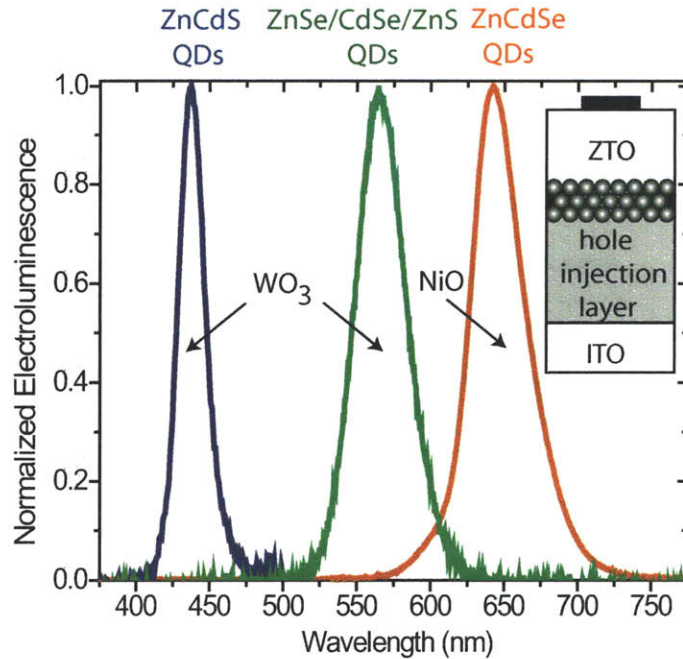


Figure 5-9: Electroluminescence spectra of blue, green, and red-emitting QDs from metal-oxide based QD-LEDs.  $\text{WO}_3$  replaced  $\text{NiO}$  as the hole injection layer to enable blue and green QD EL. The spectra are taken at 18 V, 15 V, and 12 V for the blue, green, and red, respectively.

However, transport layers can be further improved beyond energy band alignment with the QDs. As explained in Chapter 2, two important contributors to reduced device operating efficiency are charging of the QD layer and the conductivity of the adjacent metal oxide layer. ZTO layer already offers favorable band alignment for electron injection into the QD layer, so we fabricate devices that further improve the n-type ZTO layer.

Figure 5-10a presents the cross sectional schematics of four device architectures. Structures 2, 3, and 4 indicate different ways to improve the efficiency of the basic p-type  $\text{NiO}$ , QD, n-type ZTO device (Structure 1). Current density vs. voltage ( $J$ - $V$ ) and external quantum efficiency (EQE) trends for the four structures are shown in Figure 5-10b. The series of four devices were fabricated and tested a total of five times. Each time, the four devices were processed in parallel to assure uniformity between layers shared by the four devices. Different batches of  $\text{ZnCdSe}$  QDs were used for the five different devices series, resulting in some variation in the absolute

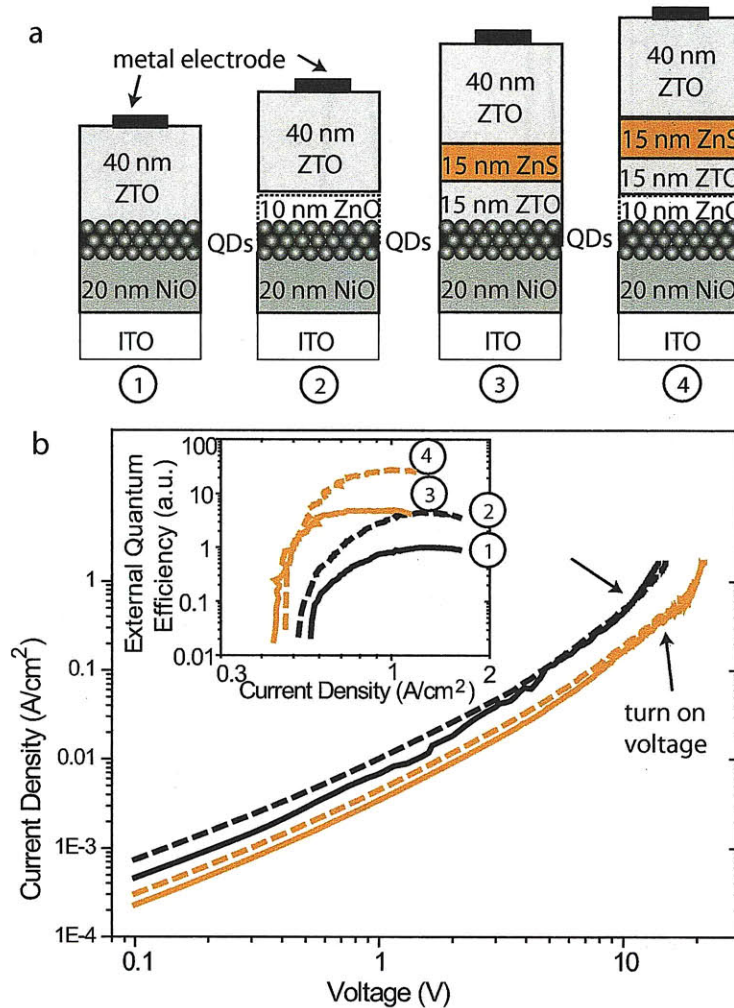


Figure 5-10: a) Schematics of the NiO-QD-ZTO device structures with modified n-type transport layers. In Structures 2 and 4, a 10 nm thick layer of ZnO is sputtered on top of the spin cast QD film. Structures 3 and 4 contain a 15 nm thick layer of ZnS within the ZTO. b) Current density vs. voltage ( $J$ - $V$ ) characteristics of the four structures. The addition of the ZnO layer (dashed vs. solid lines) does not increase the turn on voltage of the device. The inset plot of the external quantum efficiency (EQE) as a function of the current density shows systematic improvement across the four structures. The EQE characteristics for each structure are an average of data from five sets of devices, with each of the four structures processed in parallel for a given set.

EQE values. However, the trends in  $J$ - $V$  and EQE remain the same for each series of four devices, so here we present the EQE data as averages of the five different device series. The average EQEs are normalized with respect to the average EQE of Structure 1, and the largest EQE for Structure 4 observed is 0.2 %.

The first method for increasing device efficiency is to decrease the amount of QD luminescence quenching due to free carriers in the adjacent metal oxide layers. To reducing quenching from the electron transport layer located on top of the QDs, we deposit a thin, relatively insulating layer in an Ar environment at low power to avoid additional damage to the QD film. We chose a 10 nm thick layer of nearly stoichiometric (and therefore insulating) ZnO on top of the QDs (Structure 2). To form a highly insulating 10 nm thick layer of ZnO, the ZnO target is pre-sputtered to be stoichiometric prior to introducing the sample with the exposed QD film. The ZnO film is then sputter-deposited at 16 W in an Ar environment at 4 mTorr to prevent damage to the QD layer. While the ZnO becomes progressively non-stoichiometric during sputtering at these conditions, a 10 nm thick layer remains sufficiently insulating and the most insulating section of the ZnO is in contact with the QD layer. The EQE plot shows that the addition of the 10 nm ZnO layer correspondingly boosts EQE by a factor of 2.

To confirm that this increase in EQE is related to the decrease in QD luminescence quenching, we spun a highly dilute solution of QDs to form a sub-monolayer of QDs on either ZTO or 10 nm of ZnO on ZTO. Figure 5-11a compares the photoluminescence (PL) spectra of these two samples with (solid line) and without (dashed line) a ZnO layer adjacent to the QDs. A  $\lambda = 532$  nm laser source is used so that only the QDs—and not the metal oxides—are optically excited. Consistency between PL measurements for different samples was ensured by using a microscope objective to uniformly illuminate and collect luminescence from the entire sample area. The PL spectra reveal two times the QD intensity over the integrated area for the sample with the ZnO layer, indicating that the insertion of this layer reduced the number of free carriers near the QD layer and the amount of luminescence quenching. Although ZnO is an insulating layer, the turn on voltage remains 6 V for both Structures 1 and

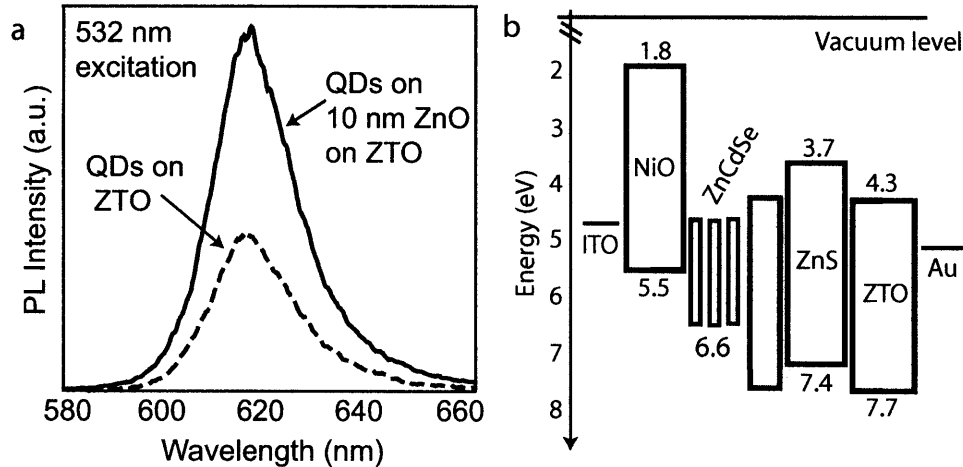


Figure 5-11: a) Photoluminescence spectra of QDs excited with a  $\lambda = 532$  nm laser. The film of QDs is spin cast on either a 40 nm thick layer of sputter deposited ZTO (dashed line) or 10 nm of ZnO on top of 40 nm of ZTO (solid line). The addition of 10 nm of insulating ZnO doubles the PL response of the QD film. b) Schematic band diagram for Structure 3 showing that ZnS acts as a barrier to electrons in the ZTO.

2. We attribute this to the fact that the ZnO does not completely cover the QD layer, as seen by comparing the AFM phase images of the initial QD film (Figure 5-2a), 10 nm of ZnO on top of the QDs (Figure 5-2b), and 10 nm of ZTO on top of the QDs (Figure 5-2c). The incomplete ZnO layer enables passage of charge through the cracks, but still minimizes the concentration of charge carriers adjacent to the QDs.

The second source of luminescence quenching is charging of the QD film. In a material set such as ZnCdSe QDs and ZTO, where there is essentially no energy barrier to electron injection into the QDs, we use a wide band gap, insulating ceramic (ZnS). This ZnS layer controls the number of electrons arriving at the QD film and prevents QD charging by balancing the number of electrons and holes arriving at the QD layer. The schematic band diagram in Figure 5-11b shows that ZnS acts as barrier to electrons in ZTO. Structure 3 demonstrates that inserting a 15 nm layer of RF sputtered ZnS within the ZTO layer improves the EQE by a factor of 5 over that of Structure 1 (See Figure 5-10b). Sputtered ZnS does not deposit uniformly on the QDs; therefore, to ensure a smooth and continuous layer, the ZnS is deposited on top of a low roughness ZTO film (See Figure 5-2c), located 15 nm above the QD film. We note that the insertion of the insulating ZnS layer in Structure 3 increases



the turn on of this device from 6 V to 11 V (Figure 5-10b). The presence of both a 10 nm ZnO layer and a 15 nm ZnS layer (Structure 4) results in the most efficient of the device structures and the ZnO layer does not increase the turn on voltage of the device beyond 11 V.

In summary, we demonstrate that an understanding of the electronic and structural properties of the component materials in metal oxide based QD-LEDs enables systematic fabrication of devices that exhibit increased efficiency and multicolor EL. At the same time, this work underscores the importance of rethinking the design of thin-film QD-LEDs. Organic-based QD-LEDs hold the record efficiencies because of the important role of Förster energy transfer in their operation and the need for only a single monolayer of QDs. Hybrid QD-LEDs with inorganic and organic transport layers can benefit from the dual excitation mechanisms of Förster energy transfer and direct charge injection while gaining stability from the ceramic materials. Systematic improvements to efficiency are possible in the case of inorganic QD-LEDs that operate via direct charge injection, but ultimately new methods for excitation of colloidal QDs that reduce non-radiative charging processes and do not require energy band alignment should be investigated. Developing such inorganic QD-LED structures will be the focus of the remainder of this thesis.



# Chapter 6

## Unipolar QD-LEDs

QDs have been incorporated into thin film LEDs that use some combination of semi-conducting polymers, small organic molecules, III-V materials, and ceramics as charge transport layers. All of these devices rely on a p-i-n type architecture, which requires the simultaneous transport of electrons and holes toward the QD emissive layer. In Chapter 5, we demonstrated that radio frequency (RF) sputter-deposited metal oxides, which are chemically and morphologically stable in air, can be used as charge transport layers to achieve QD-LEDs that do not require packaging. In these devices, efficient EL is dependent on favorable energy band alignment between the charge transport layers and the film of QD emitters. Furthermore, since the most efficient red, green, and blue QDs have different chemical compositions, a series of carefully selected transport layers is required to achieve multicolor EL with comparable efficiency and luminosity.

To obviate the restriction of precise band alignment, in this Chapter we introduce a new unipolar device architecture in which a QD multilayer is embedded in a transparent, n-type ceramic matrix and which is designed to enable only one type of charge carrier (in this case, electrons) to be injected into the device. We present results indicative of a novel, field driven mechanism for QD EL and demonstrate both green and red QD emission, with a peak luminance of  $1000 \text{ Cd/m}^2$  and a luminous efficiency of  $1 \text{ Cd/A}$  from one face of our most efficient transparent devices. These LEDs exhibit long shelf lives and enable constant luminance over extended operating

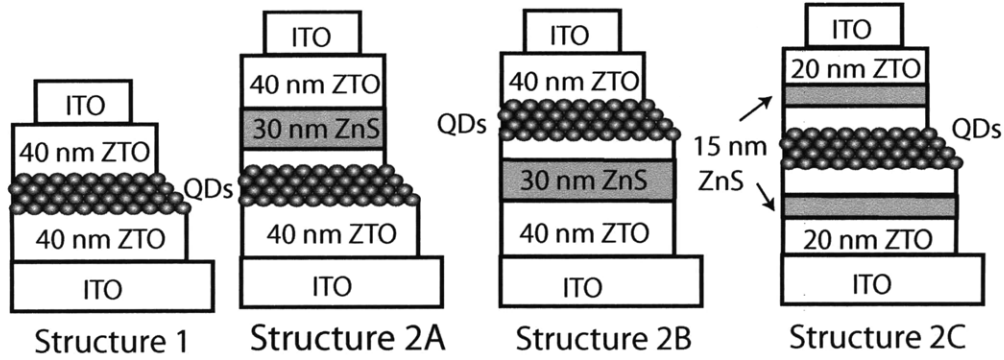


Figure 6-1: Cross-sectional schematics of the device architectures described in this letter. Structure 1 consists of colloidal QDs sandwiched between two layers of ZTO. Structures 2A, 2B, and 2C incorporate at least one layer of ZnS within the ZTO layers, located 15 nm away from the QD film. The ZnS can be positioned in the ZTO above the QDs (Structure 2A), below the QDs (Structure 2B), or on either side of the QDs (Structure 2C).

times in air, unpackaged.

## 6.1 Design and Fabrication of Unipolar QD-LEDs

We form a unipolar, n-i-n QD-LED structure by surrounding the QD film with n-type, co-sputtered ZnO and SnO<sub>2</sub> (ZTO). ZTO was used previously as the electron transport layer in our initial QD-LEDs with metal oxide charge transport layers, resulting in stable device operation. Two types of device structures (Structure 1 and Structures 2A-2C), differentiated by the presence of at least one ZnS layer in Structures 2A-2C, are depicted schematically in Figure 6-1. As discussed further in Section 6.3, ZnS layers are included in order to gain a deeper understanding of operating mechanism and improve device stability.

Device fabrication begins with ZTO deposition on top of commercial indium tin oxide (ITO)-coated glass. The QD film is spin cast, and the top ZTO film is deposited using identical target preparation and growth conditions used for the bottom ZTO layer. A 150 nm thick ITO top contact is then sputter-deposited through a shadow mask to define individual pixels.

We have considerable flexibility over the processing conditions we can use for

the bottom ZTO layer; however, to ensure that we have similar layers of ZTO on either side of the QD layer, we follow our previously developed method for depositing ZTO on top of QDs by co-sputtering the ZnO and SnO<sub>2</sub> in a pure Ar environment (See Section 5.1). Instead of introducing O<sub>2</sub> during the sputtering process, which can damage the QD layer and subsequently reduce its photoluminescence, we control the ZTO film conductivity by adjusting the relative ZnO and SnO<sub>2</sub> deposition rates. We note that this does lead to one important asymmetry: because the ZnO and the SnO<sub>2</sub> both become increasingly nonstoichiometric during sputter-deposition in a pure Ar environment, the bottom ZTO becomes increasingly conductive (i.e. more O<sub>2</sub> vacancies) toward the QD layer while the top ZTO layer becomes increasingly conductive away from the QD layer. The implications of this asymmetry are discussed further in Section 6.3.

For the QD lumophore film, we use both in-house synthesized and commercial (QD Vision, Inc.) red CdSe/ZnS or green ZnSe/CdSe/ZnS core/shell structures. The red QDs have a photoluminescence (PL) quantum yield (QY) of  $(90 \pm 5)\%$  while the green QDs have a PL QY of  $(70 \pm 5)\%$ . The device results presented in this chapter use QDs spun from chloroform at 2000 RPM. Cross sectional and topography AFM scans show five or six layers of QDs across the entire sample. Figure 6-2 shows AFM topography and phase images of a multilayer film of red QDs spun onto ZTO. The darker areas in the topography scan indicate areas where one or two QDs layers are missing; however, the phase image reveals that while small regions ( $< 50 \text{ nm} \times 50 \text{ nm}$ ) exist where there are fewer layers of QDs, the QD film completely covers the bottom ZTO layer.

In Structure 1, we have used ZTO films ranging in thickness from 20 nm to 80 nm. The various Structure 2 architectures integrate a layer of insulating wide band gap RF sputter-deposited ZnS into the basic Structure 1. The total ZnS thickness is 30 nm; in the case of Structure 2C, two 15 nm thick ZnS layers are used. Each ZnS layer is located 15 nm away from the QD region to ensure layer homogeneity. A cross-sectional scanning electron microscope (SEM) image of a completed device Structure 2A is shown in Figure 6-3a.

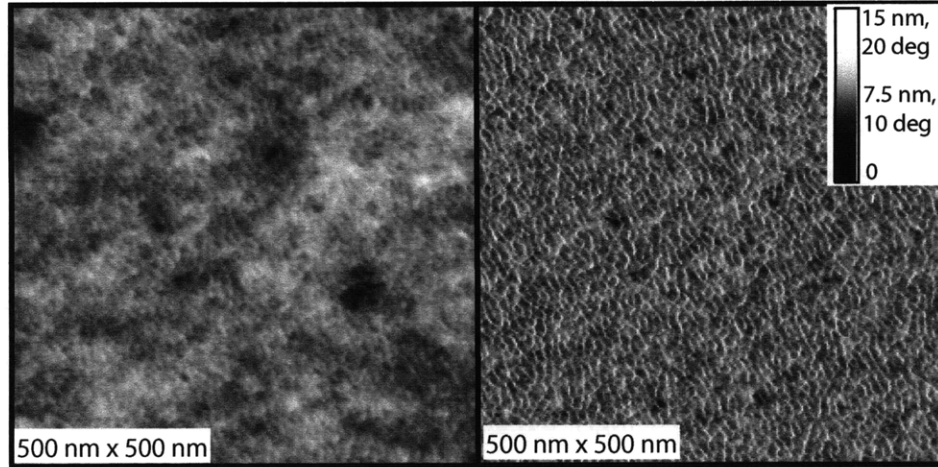


Figure 6-2: Topographical (left) and phase (right) atomic force microscopy (AFM) images of red CdSe/ZnS QDs spin coated onto 40 nm of ZTO on ITO show the type of complete and ordered film necessary for efficient device operation.

Figure 6-3b shows an optimized device structure that is used to achieve the record external quantum efficiency (EQE). It incorporates 10 nm thick, insulating layers of RF sputter-deposited ZnO directly adjacent to the QD film. The presence of these insulating ZnO layers improves the device performance in two ways. It decreases the current through the device and reduces the amount of luminescence quenching due to free carriers present in the conductive ZTO, as described in Sections 2.4 and 5.3.

For this optimized Structure 2A, we measure an absorption of less than 4% at wavelengths above  $\lambda = 500$  nm (see Figure 6-4), with most of the absorption due to the 50 nm thick QD layer. There is negligible absorption from the ceramic thin films, all of which have band gaps greater than 3 eV. The transparency of this device architecture highlights its potential for use in heads-up displays with two way viewing capabilities and stacked red, green, and blue emissive layers.

## 6.2 Unipolar Device Operatation

These unipolar, n-i-n structures enable low-voltage, forward and reverse bias direct current (DC) as well as alternating current (AC) operation. A photograph of a Structure 2A device biased at 18 V highlights the uniform EL over the entire pixel area

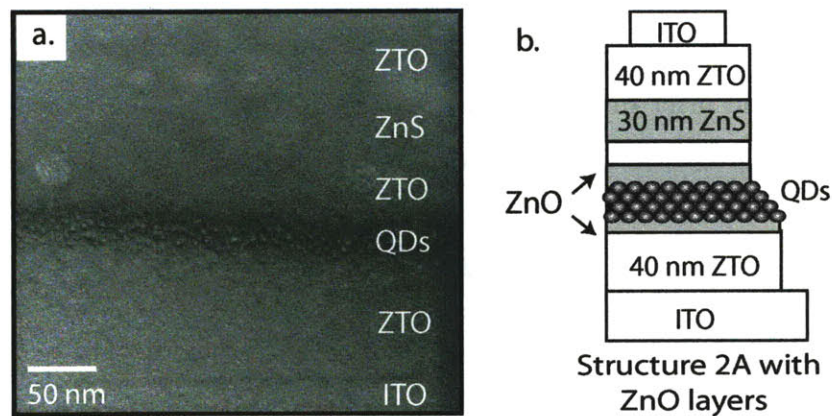


Figure 6-3: a) A cross sectional scanning electron microscope (SEM) image of device Structure 2A, which is grown on a Si substrate to facilitate sample cleaving. The sample is cleaved across the top contact using a diamond blade. The cleaved surface is cross-section polished for 5 hours and SEM images are taken with an electron energy of 10 KeV and a working distance of 3 mm. The SEM reveals continuous ceramic layers and a 50 nm thick QD region. b) The optimized unipolar device structure contains a layer of ZnO on either side of the QD layer.

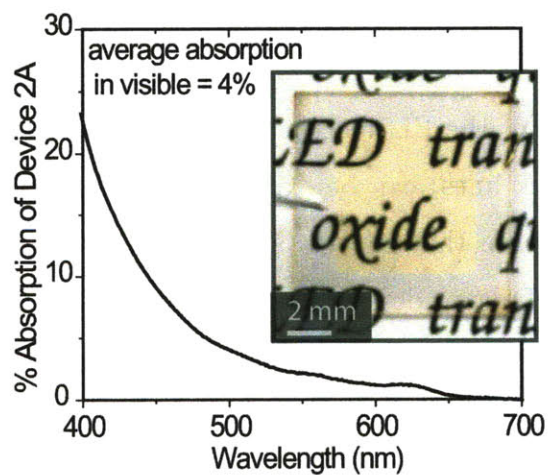


Figure 6-4: Plot of Structure 2A device absorption versus wavelength. The inset photograph shows the device on top of text to demonstrate the transparency of the wideband gap ceramics and thin QD layer.

(Figure 6-5a). In AC operation, luminescence is typically observed for applied square wave pulses with root-mean-square voltages ( $V_{rms}$ ) of 10 V to 15 V at frequencies up to 50 kHz. Figure 6-5b presents the typical current density vs. voltage ( $J$ - $V$ ) characteristics. The inset device schematic indicates our biasing convention where “reverse bias” refers to the bottom ITO layer as the source of electrons (i.e. the cathode).

An external quantum efficiency (EQE) of 0.15 % from the glass side of the device is recorded for the optimized device structure with ZnO layers adjacent to the QD film. With a luminance of 1040 Cd/m<sup>2</sup>, which is ten times video brightness, recorded at a current density of 92 mA/cm<sup>2</sup>, the luminous efficiency of these transparent structures is 1.1 Cd/A. We note that a similar amount of light is emitted through the top ITO surface, so that the overall external luminous efficiency exceeds 2 Cd/A.

The environmental stability of ZTO layers imparts a long shelf life on these unipolar devices. All device measurements are performed in ambient laboratory conditions, and repeated  $J$ - $V$  and EQE measurements recorded every week over the course of 40 days on devices stored in air showed stable luminescent response.

The EL spectra for green and red QDs in Structure 1 at 14 V demonstrate that a unipolar, n-i-n structure can be used to obtain multiple color emission from the same device structure 6-6a where the EL is due entirely to QD emission. The red-shifting and broadening of the EL spectra in comparison to the dilute QD solution PL spectra (dashed black lines) can be explained by well characterized interactions in QD ensembles. We note that the PL spectrum of the concentrated solution of red QDs used for the QD layer deposition (solid black line) matches the device PL spectrum (dashed red line). This suggests that QD proximity, through effects such as energy transfer [65] and dielectric dispersion [66], can explain the red-shift and some of the broadening. At 14 V applied bias, an increase in the full width half-maximum (FWHM) between the device PL and EL spectra of 7 nm for the red device and 8 nm for the green device is observed. Figure 6-6b shows the red shift in peak position of the PL spectra as a function of applied voltage across the device, which displays a quadratic dependence for all measured structures (1, 2A, and 2C). This red shift in



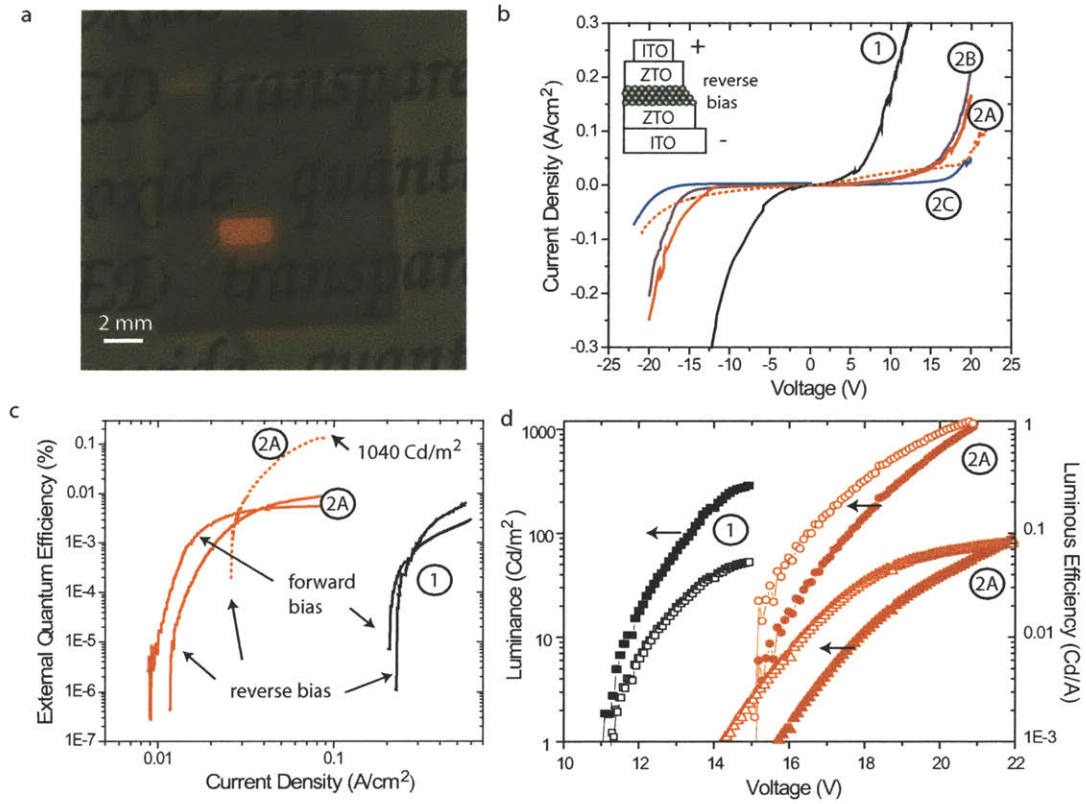


Figure 6-5: a) Photograph of device Structure 2A operating at 18 V, demonstrating the uniformity of pixel illumination as well as device transparency. b) Current density vs. voltage characteristics for device Structures 1 (black line), 2A (red line), 2B (purple line), and 2C (blue line) under forward and reverse DC bias conditions. The inset schematic indicates the bias convention. c) External quantum efficiency (EQE) versus the absolute value of current density for device Structures 1 and 2A. The dotted red lines in panels b and c show the current density and EQE measurements for the optimized Structure 2A device. d) Luminance (solid symbols) and luminous efficiency (open symbols) for device Structure 1 (black) and Structure 2A (red). Data for the optimized Structure 2A is shown in red with circle symbols.

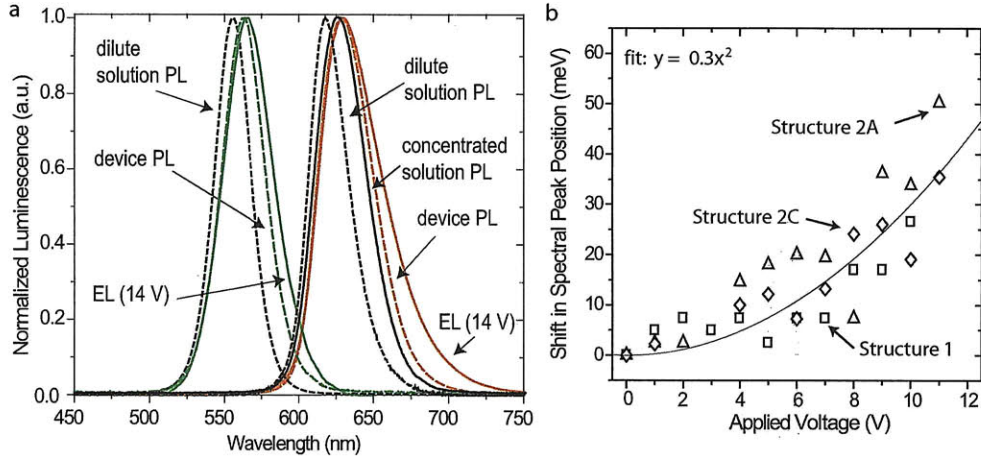


Figure 6-6: a) Spectra corresponding to photoluminescence (PL) of red and green QDs in a dilute solution (dashed black lines), PL of QDs in the device structure (dashed red and green lines), and electroluminescence (EL) from red and green QDs in device Structure 1 at 14 V bias (solid red and green lines). The PL of the concentrated solution of red QDs is shown by a solid black line. b) A plot of the shift in peak position of the PL spectra of device Structures 1 (squares), 2A (triangles), and 2C (diamonds) as a function of voltage applied across the device. For this measurement, biases below the turn-on voltage of the device are used in order to measure only the PL spectral response to electric field and not the combined EL and PL behavior.

peak position and spectral broadening as a function of applied voltage are consistent with the increased LO-phonon coupling expected with larger exciton polarization in the presence of an electric field and thus represent a manifestation of the quantum confined Stark Effect in ensembles of QDs (See Section 2.2).

Based on these observations, we propose a device operating mechanism that invokes a new method for QD luminescence, which we term QD ionization. Further experimental evidence for this proposed operating mechanism and QD ionization will be presented in Sections 6.3 and 7.1.

The schematic energy band diagram for our unipolar device (shown in Figure 6-7) is determined using ultraviolet photoelectron spectroscopy and optical absorption measurements on QD and metal oxide films as detailed in Chapter 4. We note the electron affinity of ZnS is  $(0.6 \pm 0.2)$  eV lower than that of ZTO, indicating that the ZnS shell on the QDs and the ZnS layers in Structures 2A, 2B, and 2C serve as electron blocking layers.

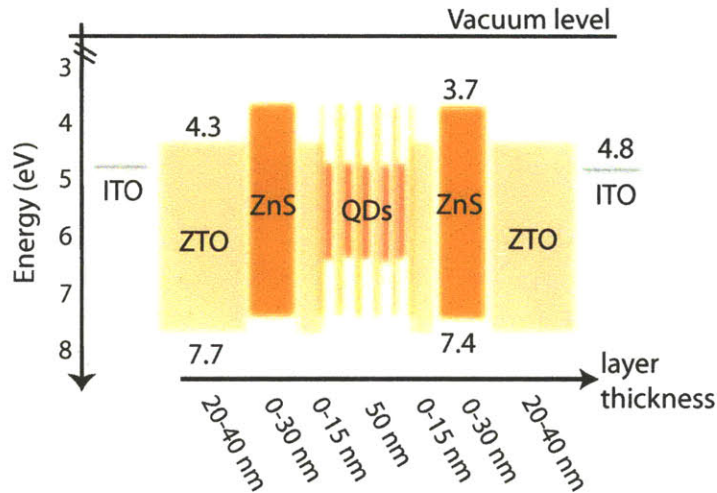


Figure 6-7: Schematic of the zero-bias band diagram for the possible unipolar device structures shows that the ZnS layer(s) and the ZnS shells on the QDs act as electron blocking layers.

Figure 6-8 shows an idealized band diagram of Structure 1 and Structure 2A under applied bias. When a voltage is applied across the device structure, electrons are injected into the n-type ZTO and accumulate at the first ZnS barrier they encounter (1), which can either be a ZnS shell of a QD or a sputtered ZnS layer, depending on the device structure and bias direction. This causes most of the voltage applied to the device to be dropped across the QD film (in the case of Structure 1) or across both the ZnS layer and the QD film (in the case of Structures 2A, 2B, and 2C). If the voltage drop across each QD exceeds the bandgap energy of the QD, an electron can be extracted from the valence band of the QD, leaving behind a hole (2). An electron from a neighboring QD (or ZTO) can then couple with this hole to form an exciton on the QD and lead to radiative recombination (3).

In the case where the first energy barrier electrons encounter is the QD layer (for example in Structure 1, in Structure 2A under reverse bias, or in Structure 2B under forward bias), the electron accumulation occurs in the ZTO as well as in the QD film. Electrons can be injected from the ZTO into QDs. As explained in Section 2.3, this causes build up of space charge in the first layer of QDs that limits

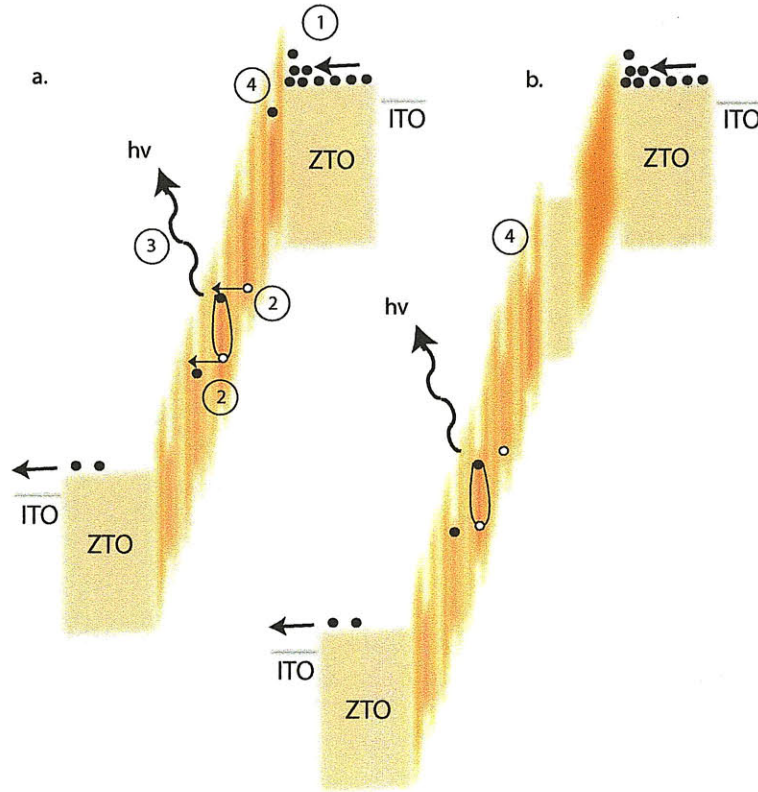


Figure 6-8: Schematic band diagrams of device Structures 1 (a) and 2A (b) under forward bias conditions. We note that a larger applied bias is needed to generate the same voltage drop across the QD film in Structure 2A as in Structure 1.

further injection of electrons into the QD film, thereby enhancing the accumulation of electrons in the ZTO layer adjacent to the QDs (4). In this case, QD charging aids in the accumulation of electrons that in turn enables a sufficient voltage drop across the QD layer to achieve electroluminescence via QD ionization; however, QD charging itself leads to luminescence quenching and slow time response. As demonstrated in Section 5.3, a sputtered ZnS layer serves as an effective barrier for electrons, reducing the direct injection of electrons from ZTO into the QD film and thereby QD charging effects (See Figure 6-8b). The following Section provides experimental confirmation of this reduced QD charging for devices in which the electrons encounter a sputtered ZnS layer prior to the QD film.

While the sputtered ZnS layer reduces charging of the QD film, Structures 2A, 2B, and 2C require a higher applied bias to achieve QD electroluminescence (See Figure 6-5). This supports the hypothesis of QD ionization. A certain minimum

electric field across the QDs is required to extract an electron from the QD valence band, generating the carriers that can recombine to generate QD luminescence. The addition of 30 nm of insulating ZnS in device Structures 2A, 2B, and 2C shifts the voltage at which this electric field is established by 4 V, thereby increasing the electroluminescent threshold of the device by 4 V.

The idea of QD ionization is also supported by our observation of red and green QD luminescence from the same device structure. We note that the voltage at which EL is first recorded for red-emitting QDs is 9 V, while it is 11 V for green-emitting QDs. These red-emitting QDs have a band gap of approximately 2.0 eV, while the band gap of the green QDs is approximately 2.3 eV. This additional 0.3 eV of energy for six layers of QDs, corresponds to an additional 1.8 V required to reach the threshold for QD ionization in the green QD layer.

### 6.3 Investigation of Device Operating Mechanism

In this section, we explain how results from three different techniques further validate our proposed device operating mechanism. We gain insights in the dynamics and location of electrons in our devices by 1) measuring the time resolved current and electroluminescence in response to DC or AC bias, 2) recording the photoluminescence (PL) quenching of the QD film while the device is operating, and 3) examining spectral characteristics of the QD emission to assess the extent of the quantum confined Stark Effect and phonon coupling.

To better understand how electrons are transported into and out of the QD layer, we examine the simplest device structure that contains no ZnS (Structure 1). We fabricate a total of nine devices with 20 nm, 40 nm, or 80 nm thick ZTO layers on either side of the QD film. The QD film thickness is kept constant. We refer to the different devices by the thickness of the ZTO layer (in nm) above and below the QDs, separated by a slash (i.e., 20/20, 20/40, 20/80, 40/20, 40/40, 40/80, 80/20, 80/40, and 80/80). The plot in the upper portion of Figure 6-9a shows the pattern of DC bias applied to the devices over a period of 5 minutes; the bottom portion shows the

resulting current through the devices as a function of time.

DC biases of 12.0 V to 17.5 V were applied to the different structures depending on the device thickness. Smaller voltages applied to thinner device structures; therefore, the magnitudes of the current or external quantum efficiency (Figure 6-9b) should not be directly compared. We also note that asymmetries in the device fabrication may cause variations in the forward and reverse biasing conditions. As mentioned in Section 6.1, sputtering the ZTO layer leads to increasing non-stoichiometry. The ZTO layer below the QDs becomes increasingly non-stoichiometric (conductive) as it approaches the QD layer, while the the ZTO sputter deposited onto the QDs is most insulating near the QD film.

However, we note two key trends in the data. First, when electrons are injected through the thicker ZTO side (e.g. forward bias for the 20/80 device or reverse bias for the 80/20 device), the current decreases quickly and then increases. When electrons are injected through the thinner ZTO side (e.g. reverse bias for the 20/80 device or forward bias for the 80/20 device), the current decreases continuously over the time frames measured. For the device with 40 nm of ZTO on both sides, the current decreases comparably in forward and reverse bias conditions. Second, in the first part of the time sequence (from 0 s to 150 s in Figure 6-9), where the same voltage is repeatedly turned off and then back on, we find that for every device, the current returns to the value it had immediately before the device was turned off. Only a switch in polarity of the bias causes the film to lose this retention effect.

Both these trends are a signature of QD charging. When electrons traveling through ZTO reach the QD interface, they accumulate and can charge the first layer of QDs. This is manifested as a drop in the current seen in all device structures under constant bias. As described in Section 2.3 accumulated electrons (space charge) cause a Coulomb blockade, which slows the passage of subsequent electrons and causes further accumulation of electrons in the ZTO layer. The thinner the ZTO layer, the more quickly electrons saturate the ZTO layer such that it is energetically favorable for electrons to percolate further into the QD film. This results in increased QD charging and a further decrease in current (See solid line 80/20 and 40/20 in forward

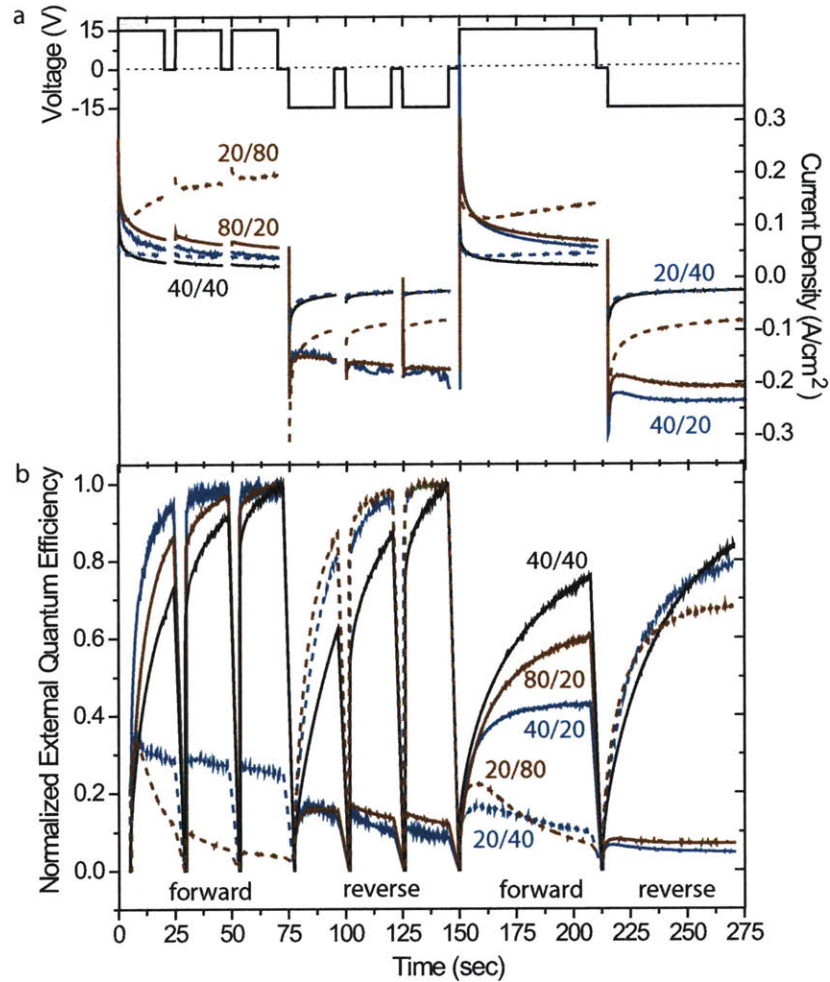


Figure 6-9: Device current (a) and external quantum efficiency (EQE) (b) for five different Structure 1 devices. The voltage pulse applied to generate the measured current and EQE is shown in panel a.

bias or 20/80 or 20/40 in reverse bias). However, when the thinner ZTO layer is near the anode (e.g. 20/80 in forward bias), the device current gradually increases at fixed voltage. After the creation of the initial space charge layer in the QD film, additional electrons tend to accumulate in the ZTO film and not the QD layer.

Indeed, we confirm that a structure with a thinner ZTO layer near the cathode experiences greater QD charging by comparing the amount of quenching of the QD PL in devices where electrons traverse a 40 nm ZTO layer (squares) and a 20 nm ZTO layer (circles) prior to reaching the QD film. Figure 6-10 shows that the 20/40 and 40/20 devices have the same trend in the PL quenching of the QD film with increasing

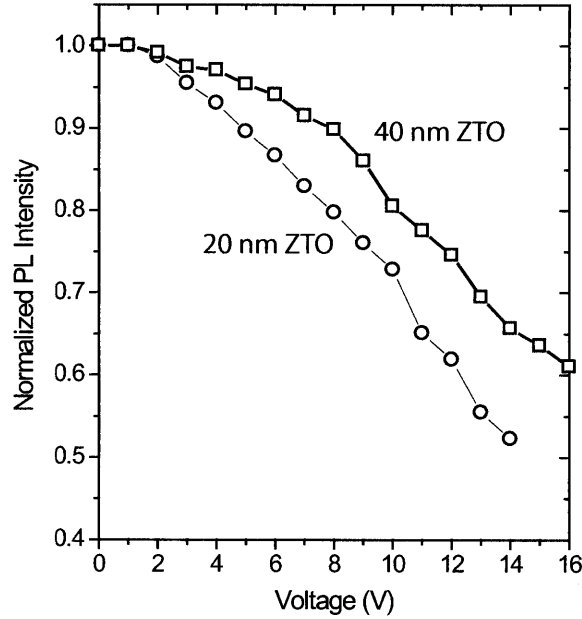


Figure 6-10: Photoluminescent (PL) response of QD film as a function of applied voltage across devices with 20 nm thick (circles) and 40 nm thick (squares) of ZTO. PL signal is normalized to the response with no applied voltage.

applied bias, and that the thinner the ZTO layer, the more the PL quenching recorded at the same applied voltage.

To understand the ramifications of QD charging for device operation, we examine the external quantum efficiency (EQE) for the devices plotted as a function of time in Figure 6-9b. Most notably, QD charging occurs over a long time scale, leading to a device current that changes over the course of minutes even under constant applied bias. The decrease in current due to QD charging leads to an increase in the EQE; however, this increase in EQE is not sustainable. Eventually, the entire QD layer becomes charged and electroluminescence (EL) ceases. On the other hand, if QD charging is reduced by having structures with thinner ZTO layers near the anode, we find decreasing EQE values due to increasing current and decreasing EL intensity. The decrease in the EL intensity can be explained by electrons distributed more evenly across the device, non-uniform electric fields throughout the QD film, and fewer QD ionization events. These observations imply that charging of the QD layer at the ZTO interface is necessary to build up a sufficient voltage drop across the



QD layer and enable QD ionization, but that excessive QD charging will eventually lead to device turn-off due to decreasing current.

In Section 6.2, we introduced the hypothesis that the addition of at least one ZnS layer in the device structure can improve device performance by limiting QD charging, while enabling the build-up of a large enough voltage drop across the QD layer to achieve QD ionization. To demonstrate this, we measure the quenching of the PL of the QD layer due to an applied voltage across the different device structures. This measurement provides an indication of the number of Auger non-radiative recombination and exciton dissociation events caused by QD charging or the presence of an electric field across the QD layer. If we assume that above the electroluminescent turn on, the voltage drop across the QD layer is comparable for all device architectures, Structures 1, 2A, 2B, and 2C should all exhibit similar degrees of exciton dissociation. Thus, differences observed in PL quenching between the structures can be attributed to charging of the QD layer. Figure 6-11 shows that device Structures 2A and 2B, which are identical except for the placement of the ZnS either above or below the QD layer, exhibit different PL quenching trends at the same voltage. When Structure 2A is under forward bias, the electrons are injected from the top contact and are blocked by a ZnS layer barrier prior to reaching the QD film. Consequently, the electric field needed for electroluminescence is achieved with relatively little charging of the QDs and the PL from the QD film shows little quenching with increasing voltage. In the case of the Structure 2B in forward bias, the electrons arrive first at the QD film. Accordingly, Structure 2B exhibits the same charging properties and trend in PL quenching as Structure 1, but offset in voltage (by 4 V) due to the presence of the insulating ZnS. The slightly larger amount of PL quenching in Structure 2C compared to Structure 2A can be explained by the fact that, in forward bias, electrons encounter a 15 nm thick ZnS layer following injection in Structure 2C, but a 30 nm thick layer in Structure 2A. The thinner ZnS layer in Structure 2C blocks fewer electrons, allowing more charging of the QD layer. By using ZnS layers, we are thus able to further validate our understanding of the device operating mechanism and controllably reduce QD charging to improve device

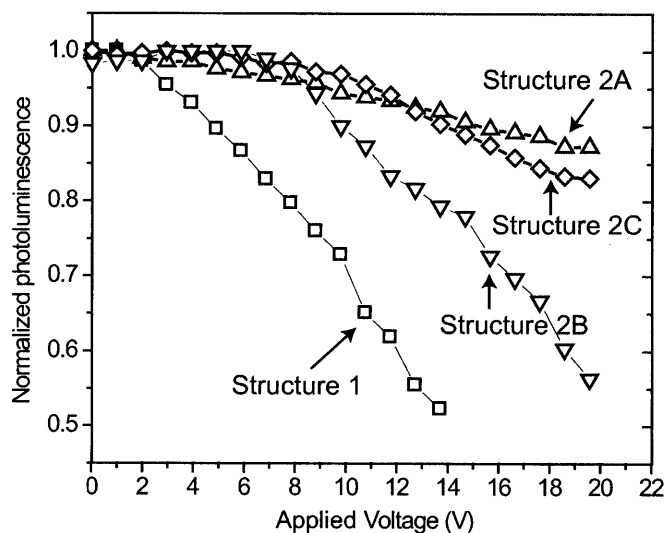


Figure 6-11: a) Plot of normalized photoluminescence (PL) as a function of applied voltage in forward bias for device Structures 1 (squares), 2A (upward pointing triangles), 2B (downward pointing triangles) and 2C (diamonds). In the case of device Structures 2A and 2C in forward bias, electrons injected into the ZTO encounter a ZnS layer prior to the QD film. In contrast, electrons in the ZTO in Structure 1 and 2B do not encounter a ZnS layer and accumulate at the QD film. Consequently, device Structures 2A and 2C show less PL quenching with increasing voltage than Structures 1 and 2B, indicating that accumulation of electrons at the ZnS layer instead of at the QD film reduces charging of the QD layer. The trend in PL quenching of device Structures 1 and 2B are the same but offset in voltage because of the presence of the insulating ZnS layer in Structure 2B. This plot illustrates that electron accumulation at the QD film, not electric field, determines the amount of QD charging luminescence quenching.

performance.

To further confirm the benefits of the ZnS in reducing QD charging, we show the electroluminescent response as a function of time for Structure 1 and Structure 2A under forward and reverse bias conditions (Figure 6-12a). Structure 1 in both forward and reverse bias shows a slow EL time response, which is a signature of QD charging. In contrast, Structure 2A shows a slow time response in reverse bias (when electrons do not encounter a ZnS layer in the ZTO before reaching the QD layer) and a relatively fast time response in forward bias (when the electrons encounter a ZnS layer in the ZTO before reaching the QD layer). Figure 6-12b shows that time constant associated with this EL decreases with increasing voltage. The greater the

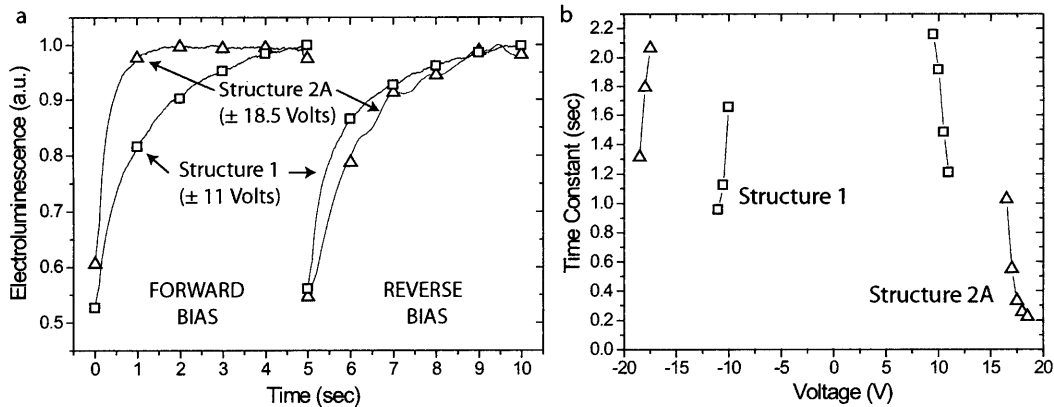


Figure 6-12: a) Electroluminescent intensity as a function of time for Structure 1 (squares) and Structure 2A (triangles) under forward and reverse bias conditions. The bias voltages are chosen such that both devices exhibit the same intensity EL after 5 s. b) Plot of the time constants associated with the EL at different voltages.

voltage applied across the device, the greater the initial current, and the more rapidly the electrons injected into the ZTO accumulate at the first ZnS barrier to enable an electrical field capable of QD ionization.

These time response characteristics are further supported by our observations of the electroluminescence (EL) as a function of the frequency of an applied alternating current bias. As shown in Figure 6-13, the EL increases with increasing frequency for structures containing a layer of ZnS, while the EL decreases with increasing frequency for Structure 1. In Structure 1, high frequency operation is not compatible with the slow dynamics associated with the formation and depletion of a space charge layer in the QD film, which is necessary to create an electric field across the QDs sufficient for QD ionization and EL. Structure 2C shows the greatest increase with frequency because electron accumulation can occur rapidly with either polarity bias due to the presence of a ZnS layer on both sides of the QD layer.

To operate with DC bias, these unipolar devices require a large enough electric field across the QD film to obtain QD ionization and sufficient transport of electrons through the device (reflected as a non-negligible current). To study the electric field and the localization of electrons simultaneously, we examine the photoluminescence (PL) and electroluminescence (EL) spectra of our devices using the setup described in

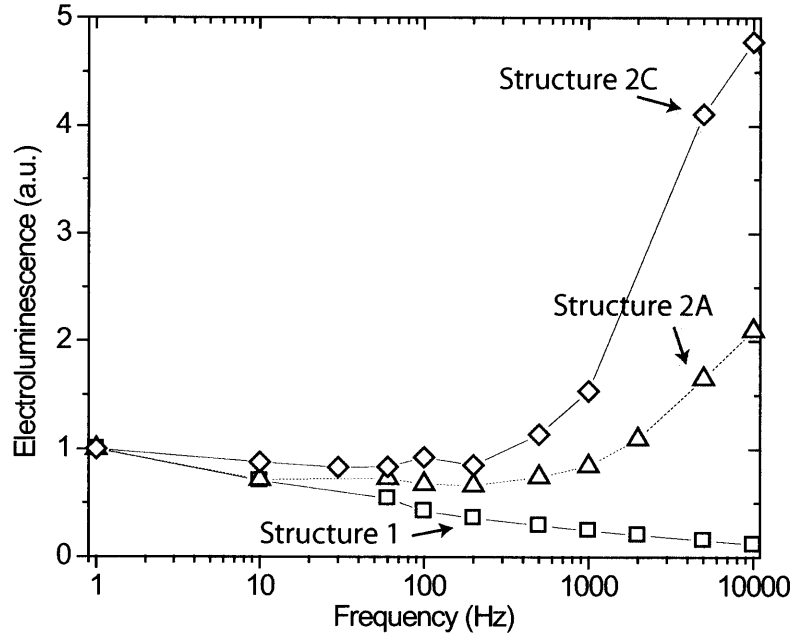


Figure 6-13: Plot of the electroluminescent response as a function of frequency of the applied bias.

Chapter 4. We measure the emission spectrum of our devices under applied DC bias and optically excited with a  $\lambda = 514 \text{ nm}$  laser source. The midpoint positions of the red and blue side and peak position of the spectra of device Structures 1 (squares), 2A (upward pointing triangles), and 2C (diamonds) are plotted with open symbols in Figure 6-14a. Below the EL turn on for the devices (8 V, 10 V, and 12 V for Structures 1, 2A, and 2C, respectively), we are measuring only the PL response. As discussed in Section 6.1, we observe a quadratic dependence of the red shift in peak position (see solid line fit) and a broadening of the PL spectra as a function of the applied voltage across the device. This is consistent with the quantum confined Stark Effect in QD ensembles and increased LO-phonon coupling expected with larger exciton polarization in the presence of an electric field.

At voltages above the device EL turn on, this data provides the combined EL and PL response, and the spectral peak positions begin to deviate from the quadratic dependence. In solid symbols, we overlay the midpoint positions of the red and blue side and peak position of the EL spectra only (i.e., no  $\lambda = 514 \text{ nm}$  laser excitation). The midpoint of blue side of the spectra remains constant at 1.94 V and the spectral

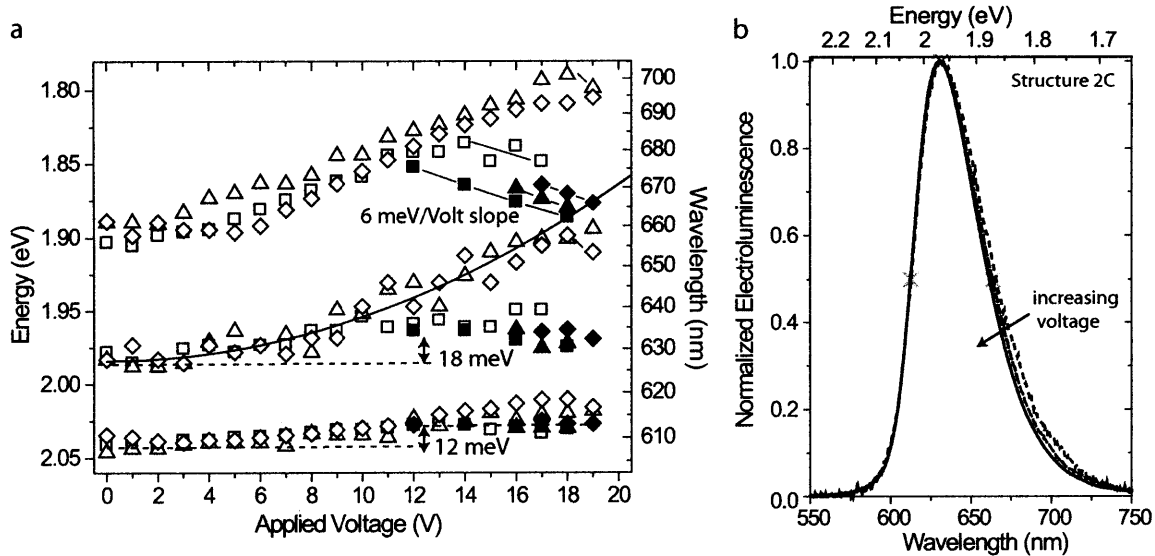


Figure 6-14: a) Plot of the midpoints of the red and blue sides and peak position of the combined EL and PL spectra (open symbols) and EL spectra only (solid symbols). Data for Structures 1 (squares), 2A (upward pointing triangles), 2B (downward pointing triangles), and 2C (diamonds) are shown. b) EL spectra of device Structure 2A at 17 V, 18 V, and 19 V.

peaks increase slightly in energy from 2.03 eV. The midpoints of the red side of the spectra, in contrast, move 6 meV higher in energy for each additional volt applied across the device. To visually indicate this dramatic effect of applied voltage on the EL spectra, Figure 6-14b shows the EL spectra of Structure 2C with applied DC biases of 17 V (dotted line), 18 V (dashed line), and 19 V (solid line). As indicated by the arrow, the red side of the spectra narrows with increasing applied bias, while the peak position and blue side of the spectra remain essentially fixed.

This spectral narrowing can be understood in relation to our proposed device operating mechanism. An increase in applied voltage above the EL turn-on voltage results in an increase in the luminescent intensity, implying an increase in the number of QDs that are ionized. This in turn results in an increase number of electrons in the QD film in proximity to the ionized QDs since diffusion of the electrons in the QD film is relatively slow. Additional electrons near the ionized QDs screen the increase in electric field across the QD layer as a function of voltage, which is seen clearly in the combined PL and EL data. A certain electric field is required for QD ionization;

hence the spectral peak remains near the threshold value for EL (18 meV red-shifted from the 0 V position). As expected, the screening from the additional electrons at higher applied biases reduces more significantly the phonon coupling, which we see manifested in the 6 meV per volt narrowing of the spectra. Indeed, at a given voltage, narrower spectra correspond to the devices with the highest densities of electrons in the QD layer. For example, at 17 V, Structure 1 has a current of 10.75 A/cm<sup>2</sup> and a spectral full width half maximum (FWHM) of 48 nm; Structure 2C has a current of 0.012 A/cm<sup>2</sup> and FWHM of 52 nm. The difference between the EL and PL spectra indicates that electrons are situated locally in the QD film: the EL spectra reflect the local conditions around QDs that exhibit EL and the PL spectra reflect the average conditions across the QD layer.

In summary, we demonstrated that the introduction of an appropriate thin film of ceramic material (in this case, ZnS) into the charge transport layer to create a potential barrier for majority carriers improves device performance by reducing charging of the QD layer.

## 6.4 Benefits of Unipolar Device

In addition to offering multicolor QD emission from transparent device structures that exhibit stable operation in air without packaging, the unipolar device architecture solves one of the key challenges facing QD display technology: constant luminance during extended operation.

Understanding of the device operating mechanism gained from the experiments described in the previous section enables us to choose favorable bias conditions for extended testing. A device held under constant DC bias exhibits gradual charging of the QD layer, which is manifested by a corresponding decrease in device current over time. Device Structure 1 no longer exhibits EL after approximately 5 minutes at constant applied bias due to a lack of sufficient current through the device. Structure 2A, in which the QD charging occurs at a slower rate due to the presence of the ZnS layer, exhibits EL for approximately 45 minutes when forward biased in a constant

voltage mode. In order to circumvent eventual device turn-off with a constant applied voltage, we therefore perform extended lifetime testing on Structure 2A run in a constant current mode, with voltage and luminescence measured in 5 s intervals. We test a device with an average EQE to ensure that our results are representative. Figure 6-15a shows luminescence as a function of time during 20 hours of continuous device operation. This data is replotted in Figure 6-15b to show luminosity as a function of voltage while omitting the information regarding the time at which the luminosity and voltage data point was taken. Figure 6-15b) shows that all the 14,400 data points fall on the same curve. In other words, for a given voltage and current at any point during the 20 hours of testing, the device exhibits the same luminosity. To exemplify this, we indicate data points  $\alpha$  and  $\beta$  that have identical and luminescence response at the same voltage although they are taken more than eight hours apart. This plot indicates that an unpackaged device does not degrade over 20 hours of continuous operation in air.

In summary, this chapter introduced a unipolar, n-i-n light emitting device architecture that operates using a previously unreported method of QD excitation. We demonstrated that QD ionization as a means for generating electroluminescence (EL) facilitates the use of stable transport materials and reduces the need for complicated band alignment engineering discussed in Chapter 5. In addition to enabling air stable electroluminescence (EL) from multicolored QDs at constant luminance, these unipolar devices represent a paradigm shift away from direct injection of electrons and hole into the QD layer. While Section 6.3 described experiments which provided evidence in support of our proposed operating mechanism, further investigation of the QD ionization mechanism is required. In Chapter 7, we present a device structure that eliminates electron injection into the QD layer from a semiconducting metal oxide (as in the unipolar architecture), and therefore enables focused study of the generation of charge carriers via ionization of QD in high field conditions.

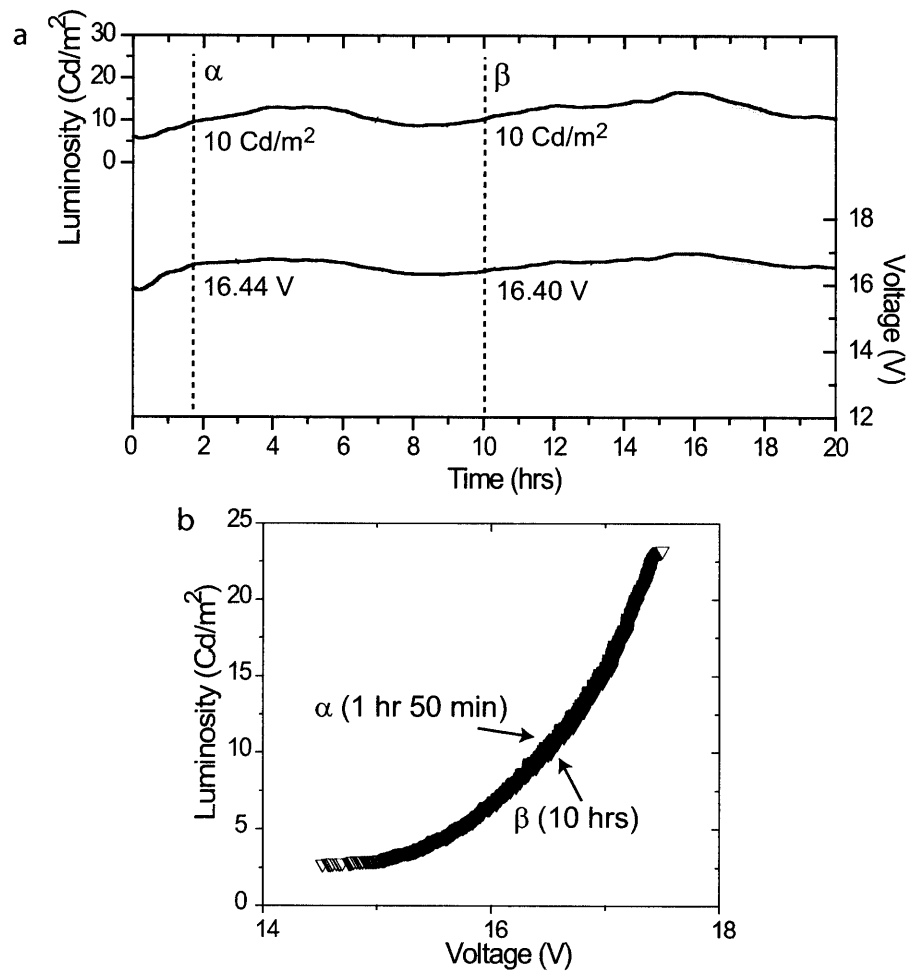


Figure 6-15: a) Plot of luminosity (top, left axis) and voltage (bottom, right axis) as a function of time for device Structure 2A operated in forward bias at a constant current of 30 mA/cm<sup>2</sup>. The device was unpackaged and operated in air. Voltage and luminescence data were recorded every 5 s for 20 consecutive hours and then binned and averaged into one minute intervals. b) Scatter plot of luminosity versus voltage using all of the data in panel a shows that despite fluctuations in the voltage and luminosity over time, the luminosity at a given voltage is constant, indicating that these fluctuations do not correspond to changes in the device performance with time. For example, the voltage and luminosity at 1 hour 50 minutes ( $\alpha$ ) and 10 hours ( $\beta$ ) are comparable.



# Chapter 7

## QD Thin Film Electroluminescence

The unipolar device architecture presented in Chapter 6 demonstrates that direct injection of hole and electrons into the QD film from n- and p-type charge transport layers is not the only method for achieving electroluminescence (EL). In this Chapter, we go one step beyond the unipolar device architecture and discuss devices that eliminate charge transport layers such as ZTO. These thin film electroluminescent (TFEL) devices incorporate a film of QDs between two insulating and wide band gap metal oxides. We find that these TFEL QD devices eliminate the need for energy band alignment between the QD film and the neighboring metal oxide layers and provide a structure in which an arbitrarily high electric field (up to the break down field of the constituent metal oxide layers) can be created, enabling electrical excitation of virtually any type of QD.

In addition to the benefits of this system for studying field-driven electrical excitation of colloidal QDs, this work is also motivated by the technological challenges currently facing TFEL devices. Alternating current thin-film electroluminescent (AC-TFEL) devices already occupy a segment of the large area, high resolution, flat panel display market. AC-TFEL devices currently available for purchase consist of a phosphor layer, such as manganese doped-zinc sulfide (ZnS:Mn), vertically sandwiched between two insulators that are contacted by electrodes. When a sufficiently high voltage is applied across the electrodes, electrons trapped at insulator-phosphor interface are injected into the conduction band of the phosphor, where they are accel-

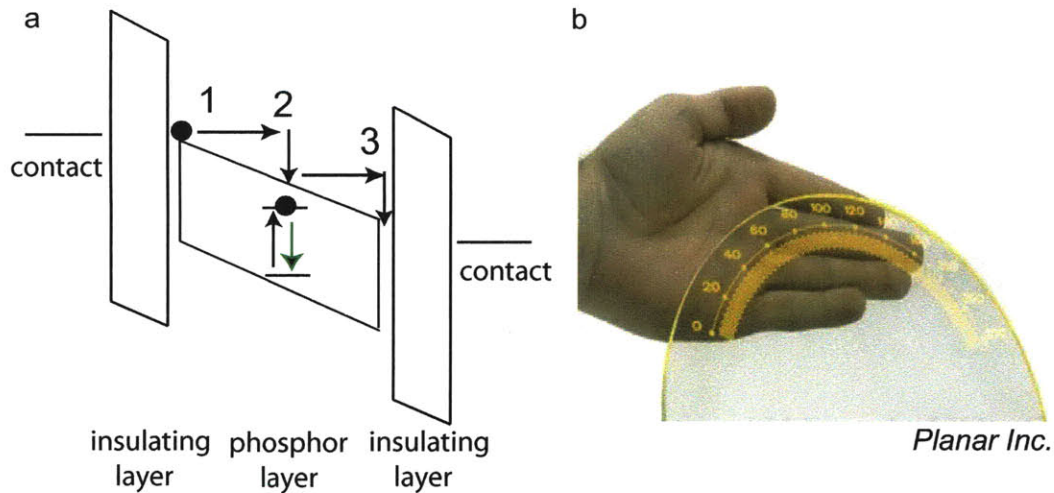


Figure 7-1: a) Schematic band diagram of an AC TFEL device showing some of the key operating principles. Electrons trapped at interfaces between the insulating and phosphor layers are injected into the conduction band of the phosphor, where they are accelerated by the field (1). These high energy electrons can excite the luminescent dopant centers in the phosphor layer via impact excitation and ionization mechanisms. The luminescent center can then radiatively or non-radiatively relax (2). The electrons are transported to the other interface where they become trapped (3). b) Photograph of a Planar Inc. transparent AC TFEL display.

erated by the field and can excite the luminescent dopant centers in the phosphor layer via impact excitation and ionization mechanisms [67, 68]. AC-TFEL displays are robust, possess long lifetimes, and offer high luminance with relatively low power consumption [69]. However, while fabrication of AC-TFEL devices has been the subject of considerable study over the past three decades, challenges remain. Development of multicolor displays with balanced red, green, and blue (RGB) emission has proven difficult as the most efficient red, green, and blue phosphors comprise different materials systems that require different deposition and annealing steps [70, 71, 69]. Additionally, differences in luminous efficiencies of different colors can span an order of magnitude, complicating electronic driving of balanced color displays. As shown in Figure 7-1, transparent AC-TFEL displays have recently been demonstrated by Planar Inc.; however, the processing of the phosphor to achieve transparency is difficult and has not yet been developed for phosphors other than ZnS:Mn.

In this chapter, we demonstrate that QD films can replace phosphor-doped thin

films in TFEL devices. We demonstrate EL from red, green, blue, and infrared emitting QDs, as well as from Mn-doped nanocrystals. The use of QDs as the active luminescent materials enables a solution-deposited active layer and room temperature device fabrication.

## 7.1 Field-Driven Electroluminescence from QDs

### 7.1.1 Thin Film Electroluminescence

For our QD TFEL devices, we choose a device architecture similar to that of Mn doped ZnS thin film-based devices. As shown in Figure 7-2a, the QDs are sandwiched between two insulating metal oxide layers, such as  $\text{HfO}_2$ ,  $\text{Al}_2\text{O}_3$ , or  $\text{SiO}_2$ . Both metal oxides layers are sputter deposited in an inert Ar environment at 4 mTorr with a power of 100 W (for  $\text{HfO}_2$ ), 150 W (for  $\text{Al}_2\text{O}_3$ ), and 165 W (for  $\text{SiO}_2$ ). Transparent devices, shown in Figure 7-2b, can be realized by using sputter deposited indium tin oxide (ITO) for both electrodes; however, most often we sputter-deposit an Al top electrode, which can also serve as a reflector for the EL. In this section, we describe a device with spin cast QD layers. The spin conditions vary based on the QD capping ligands and the metal oxide layer, and they are optimized for layer uniformity as described in Chapter 4. The height of the spin cast layer is determined by cross-sectional AFM, and typical layer thicknesses range from 50 nm to 100 nm. Figure 7-2c shows images of completed devices with red, green, and blue QD active layers under UV illumination.

Figure 7-3a shows the electroluminescence (EL) spectra and photoluminescence (PL) spectra for TFEL devices with QDs that emit in the infrared, red, green, and blue. We note that all the devices experience broadening of the red-side of the spectrum. As discussed in Chapter 2, broadening of the red-side of a QD emission spectrum is indicative of enhanced phonon coupling, which is consistent with the repetitive polarization of the QD crystal lattice due to the high, alternating electric fields applied to this device structure.

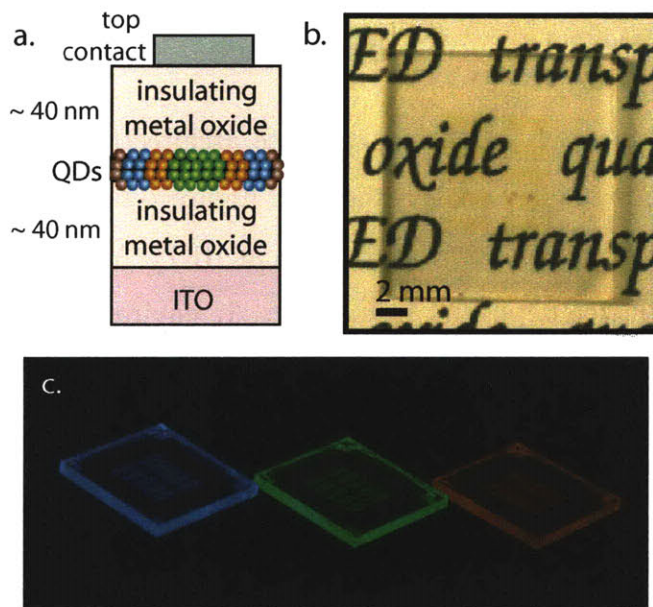


Figure 7-2: a) Schematic of a TFEL device incorporating a QD layer. b) Photograph of a completed TFEL structure (containing red-emitting QDs) that uses ITO for both the top and bottom contacts. The device is placed on top of a sheet of paper with black lettering to highlight the transparency of the device. c) Photograph of completed device structures containing red, green, and blue QD active layers under UV illumination.

The EL spectrum of the blue emitting QD device shows a secondary emission peak situated in the deep red wavelength region (centered at 1.6 eV). This peak is characteristic of defect state emission that can be attributed to the loss of passivating ligands on the QDs. The PL spectra of devices containing QDs that emit in the visible wavelength region are taken with the time-resolved setup described in Chapter 4. This relatively high powered laser excitation source enables excitation of defect states in the QDs caused by the sputter deposition of the top metal oxide layer (See Section 7.2). However, in this case, no defect state emission is visible in the blue PL spectrum (taken before device operation), which suggests that defect states are created during device operation. We observe that the defect state peak in the EL spectrum becomes more pronounced as a function of time. The origin of these defect states and a method for minimizing their creation is discussed in Section 7.1.2.

As highlighted in Figure 7-3, these TFEL devices enable the first demonstration of EL using either PbS/CdS or CdSe/ZnS core/shell QDs, providing tunable emission across a 1  $\mu\text{m}$  wavelength range. The ability to electrically excite QDs of different chemistries and over a wide range of emission wavelengths highlights that while the EL turn on voltage depends on the QD band gap (the bluer the QD emission, the higher the voltage required to achieve EL turn on), the band alignment between the QDs and the metal oxide layers is of little importance. This is consistent with our hypothesis that TFEL devices operate via QD ionization and subsequent recombination of the ionized electron. As discussed in Chapter 6, QD ionization will occur when the voltage drop across each QD exceeds the band gap energy of the QD.

To confirm that EL can be ascribed to the QD ionization process, we experimentally determine - for each different color-emitting TFEL device - the smallest voltage drop per QD that results in EL and compare this value to the bandgap of the QD. To determine the approximate voltage drop per QD, we model our TFEL device as three capacitors in series ( $C_{oxide}$ ,  $C_{QD}$ , and  $C_{oxide}$ ). We measure the capacitance as a function of frequency for the insulating metal oxide films and the entire TFEL device, and from these values we calculate the capacitance of the QD layer. The number of layers of QDs in the QD film is determined by dividing the thickness of the QD layer

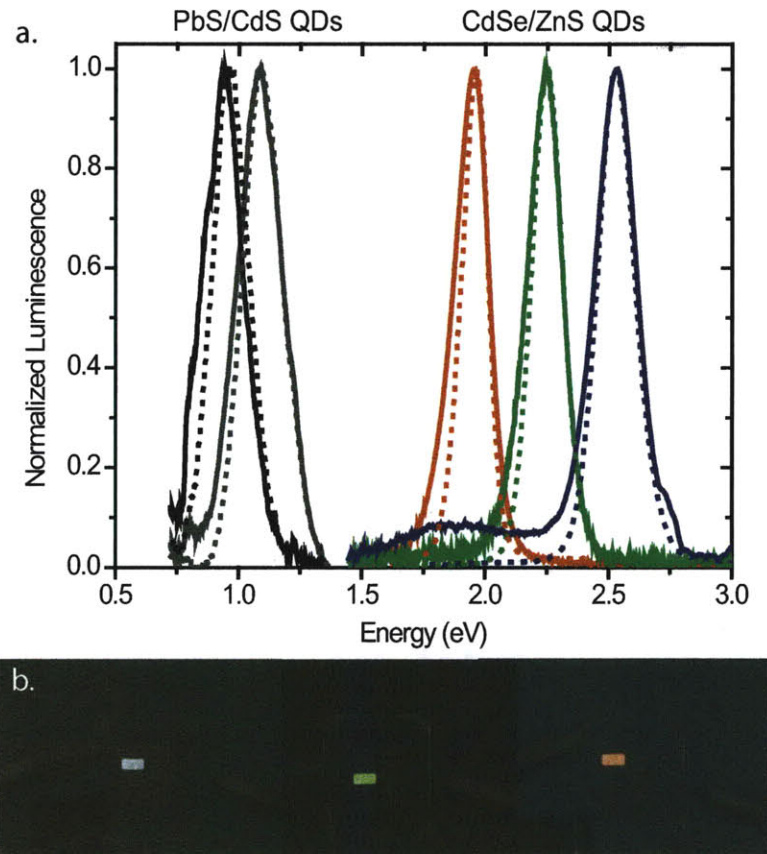


Figure 7-3: a) Photoluminescence (dashed lines) and electroluminescence (solid lines) spectra for blue, green, red, and infrared emitting QDs in a TFEL device structure. b) Photographs of the red, green, and blue devices operating at 30 kHz and 110  $V_{p-p}$ , 130  $V_{p-p}$ , and 145  $V_{p-p}$ , respectively.

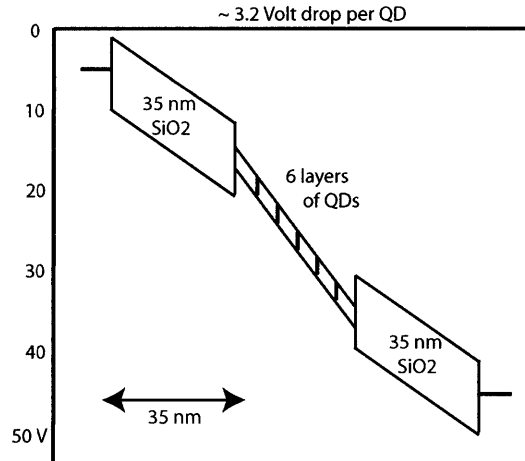


Figure 7-4: Schematic band diagram for TFEL device under  $80 V_{p-p}$  applied bias.

by the diameter of a single QD, measured by AFM. These capacitance and thickness values enable us to calculate the voltage drop across each layer and each QD for a given applied bias. For example, Figure 7-4 shows a schematic band diagram of a TFEL device with SiO<sub>2</sub> metal oxide layers and an active layer of red CdSe/ZnS QDs under  $80 V_{p-p}$  applied bias. We find a 3.2 V per QD drop, which should be sufficient to ionize the QDs, and indeed, we observe EL from TFEL device biased at  $80 V_{p-p}$ .

For each TFEL device containing a different color-emitting QD, we choose three different sample biases slightly above the threshold voltage at which EL is first observed, and plot the light power versus the voltage drop per QD (See Figure 7-5). If we compare the voltage-axis intercepts for each device, which provide an approximate value for the EL threshold, to the energy of the luminescence for the corresponding device shown in Figure 7-3a, we find that threshold voltages correspond well to the QD bandgap energies for the blue, green, red, and infrared emitting devices. We find further indication that the EL is due entirely to the voltage dropped across each QD by determining that the EL threshold occurs at the same voltage drop per QD for structures having either Al<sub>2</sub>O<sub>3</sub> (dotted red line) or SiO<sub>2</sub> (solid red line) insulating layers, but containing the same red CdSe/ZnS QDs.

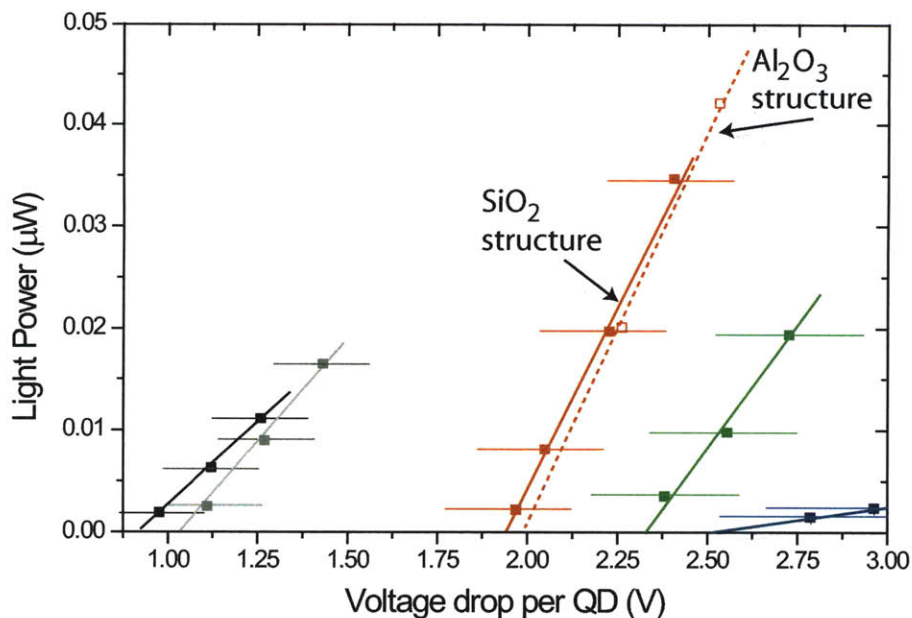


Figure 7-5: Plot of the light output as a function of the voltage drop across the QD layer.

### 7.1.2 Mixed QD and Insulating Polymer

As discussed previously, we observe that the defect state peak in the EL spectrum becomes more pronounced during device operation. While the defect state emission is particularly prominent for the blue-emitting devices, we also observe it in the green and red QD devices under extended operation. We attribute this increase in defect state emission to the loss of passivating ligands that surround the QDs. Indeed, Figure 7-6a shows that the photoluminescence of the QD active layer is drastically reduced over the course of device operation.

We can reduce the loss of ligands by stabilizing the QDs in a polyisobutylene (PIB) polymer. PIB is a transparent, electrically insulating polymer, which we will discuss further in Section 7.3. In this experiment, we prepare a solution of PIB in chloroform at a concentration of 15 mg per 1 mL and then combine it in a 1 to 1 ratio by volume with the same QD solution used for the active layer of the device shown in Figure 7-6a. Figure 7-6b shows little evidence of QD luminescence quenching following operation of the QD-polymer devices, indicating that the PIB reduces ligands loss during device operation.



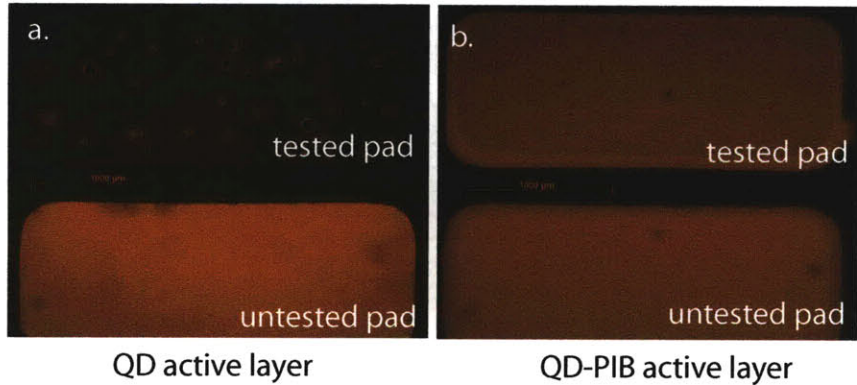


Figure 7-6: Fluorescence microscope images of tested and untested pads in TFEL devices with a QD active layer (a) and with a QD-PIB composite active layer (b). The tested pad in panel a exhibits quenched QD luminescence, which can be attributed to loss of QD ligands.

Furthermore, the ability to achieve EL from a mixed QD and insulating polymer active layer reinforces the hypothesis that QD ionization is the mechanism for EL in these QD TFEL devices. AFM images of the QD-PIB layer indicate that the QDs cluster together in groups of approximately 10 to 20 QDs surrounded by continuous network of PIB. With the QDs dispersed in clusters, no electrical continuity is possible across the entire QD film. QD ionization requires only that two QDs be in electrical contact: an electron must be extracted from one QD and transferred to the neighboring QD so that this electron can recombine with the vacancy it created when the polarity electric field is reversed. Indeed, we find that completely dispersing the QDs in an acrylic polymer (provided by QD Vision Inc.) so that no two QDs are in electrical contact leads to high thin film PL efficiencies but prevents EL.

### 7.1.3 Electrical and Optical Characterization

We can gain further insight into the operating mechanism of the TFEL devices by measuring their time resolved electrical and optical properties. This is somewhat more complicated than characterization of the diode and unipolar QD-LEDs discussed in Chapters 5 and 6, respectively. First, a TFEL device is capacitive so the current in the QD layer that contributes to EL cannot be measured directly with a current

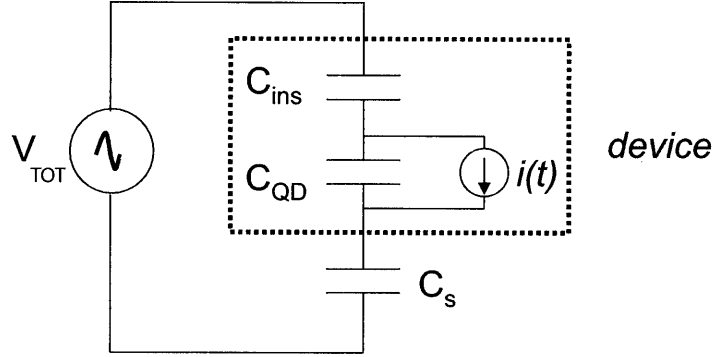


Figure 7-7: Schematic of test setup used to measure the current through the QD layer as a function of time.

meter. Second, the device operates with high voltage sinusoidal inputs in the kilohertz frequency range, necessitating specialized test circuitry and electrical shielding described in Chapter 4.

To calculate the current in the QD layer, we implement a method that is similar to that used for calculating the current through the phosphor layer in AC-TFEL devices [67, 72]. When a TFEL device is biased below threshold (i.e. at a voltage where no electroluminescence is observed), the device is considered to consist of three capacitors in series. Above a threshold, current flows in the active layer, and the device can be treated as three capacitors in series with a current source in parallel with the center capacitor (active layer). In a thin film phosphor device, this current originates from electrons trapped at interface states, which can be tunnel emitted into the active layer under sufficient applied bias. The source of this current in field-driven QD devices is the electrons that are extracted from the valence band of the QD in the QD ionization process. This internal current ( $i_{int}$ ), regardless of its origin, cannot be directly measured; however, a sense capacitor ( $C_s$ ) in series with the device can be used to record the charge ( $q_{int}$ ) traveling in the active layer. A schematic of the test setup is shown in Figure 7-7. We measure the input voltage ( $V_{TOT}$ ) and the voltage across the sense capacitor ( $v_s$ ). The voltage across device ( $v_{dev}$ ) is simply  $v_{dev} = V_{TOT} - v_s$ . The sense capacitor is chosen to be approximately an order of magnitude larger than the device capacitance. For the data reported below we use a

10 nF sense capacitor; however, we also verify that 3.3 nF sense capacitor generates the same results for the time resolved current. If we know the capacitance of the metal oxide layers ( $C_{ins}$ ) and the capacitance of the QD layer ( $C_{QD}$ ), we calculate the charge across the QD layer to be

$$q_{int}(t) = \frac{(C_{ins} + C_{QD})}{C_{ins}} C_s v_s(t) - C_{QD} v_{dev}(t). \quad (7.1)$$

The current through QD layer as a function of time can be found by taking the derivative of Equation 7.1:

$$i_{int}(t) = \frac{dq_{int}(t)}{dt}.$$

Simultaneously, we record the time resolved electroluminescence using a surface mounted photodetector with a 1 ns response time when biased at 20 V (See Chapter 4).

Figure 7-8 shows the voltage across device ( $v_{dev}$ ), the current through the QD layer ( $i_{int}$ ), and the EL response as a function of time for three different frequencies of the applied bias. In Figure 7-8a, the current through the QD layer follows the polarity of the applied bias, and the maximum EL is observed at the largest current values. This suggests that the QD ionization process does not require a switch in the polarity of the applied bias to generate EL. This observation is consistent with our DC bias operation of the unipolar devices presented in Chapter 6. If multiple QDs are ionized, the electron extracted from one QD can recombine with the hole left by an extracted electron from the neighboring QD. However, unlike the unipolar device architecture in which electrons can be injected into the QD layer from the ZTO, in the case of that TFEL architecture, the supply of electrons is finite (carriers are generated entirely from within the QD active layer) so an AC bias is required for sustained EL. As in the case of the unipolar device architecture containing insulating ZnS layers, Figure 7-8 shows that in TFEL devices, the EL increases as a function of the frequency of applied voltage (See Figure 6-13). Our time resolved data shows that a higher frequency implies more carriers in the active layer (manifested as a larger current), which increases the probability of electron and hole recombination.

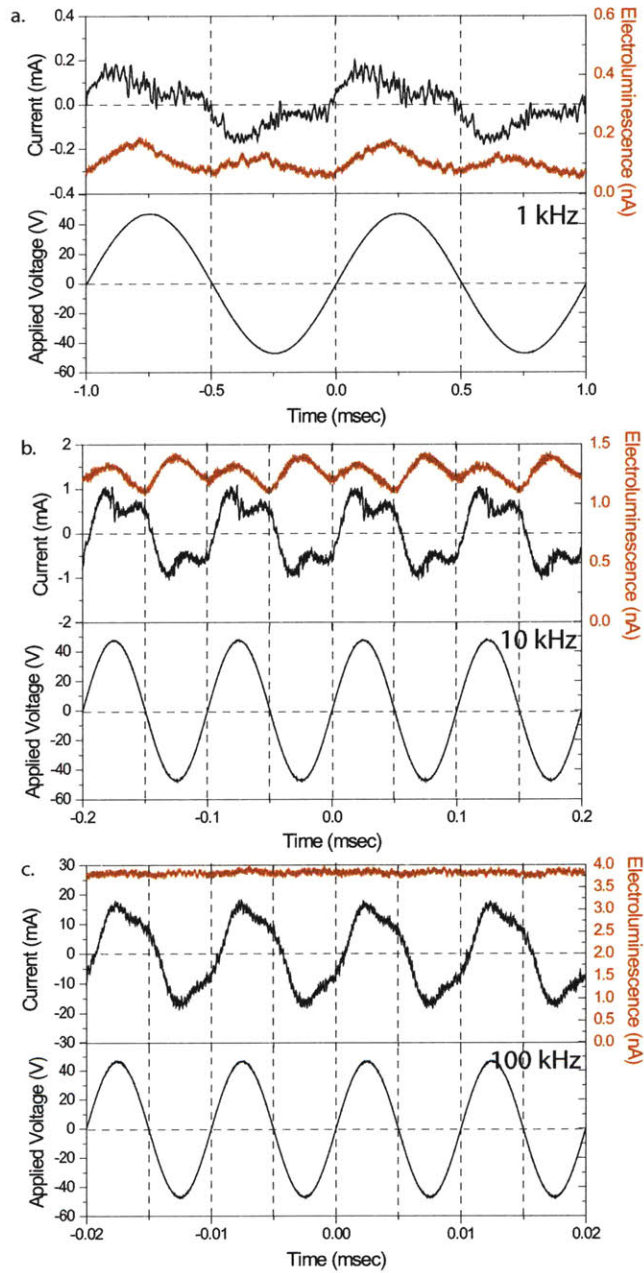


Figure 7-8: Plots of the voltage across the device, the current through the QD layer, and the electroluminescence of the device recorded by the photodetector for applied bias frequencies of a) 1 kHz, b) 10 kHz, and c) 100 kHz.

## 7.2 Electrical Excitation of Phosphor-doped Nanocrystals

Because of the similarity between our QD-LED structures described in Section 7.1 and commercial AC-TFEL devices with phosphor layers, we investigate the possibility of electrically exciting phosphor-doped QDs. To date, colloidal nanocrystals have successfully been doped with transition metals (such as Fe, Ni, Mn, Cu) and lanthanides (such as Eu, Er, Tm, Tb) to alter their electronic, optical, or magnetic properties [73]. If the excitation energy of the dopant is smaller than the band gap of the host material, the photoluminescence of the doped nanocrystal is determined by the dopant atoms; light emission is independent of the band gap of the host material and largely immune to thermal and chemical variations of the surrounding medium [74]. For example, by using different dopants or various synthetic procedures [75], the emission wavelength of doped ZnSe nanocrystals can be tuned from the blue through the red, suggesting the possibility of developing multicolored AC-TFEL displays. Furthermore, when the nanocrystal host material is a wide band gap semiconductor such as ZnSe, thin films of nanocrystals do not absorb in the visible wavelength region (See Figure 7-10b), making them compatible with the construction of transparent devices. Such devices could be used for displays with two-way, heads-up viewing capabilities.

However, until this work, there had been no demonstration of EL from phosphor impurity dopants in ZnSe or other wide band gap host nanocrystals. Luminescence of CdS:Mn/ZnS nanocrystals embedded into a polymer-LED was observed [76]; however, color-tunable doping or a transparent device is challenging to achieve with this structure because of the relatively small band gap of CdS. In order for these doped nanocrystals to be luminescent at the colors of the dopant, the excitation energy of the dopant needs to be smaller than the band gap of the host material to enable energy transfer of an exciton on the nanocrystal core to the impurity dopant.

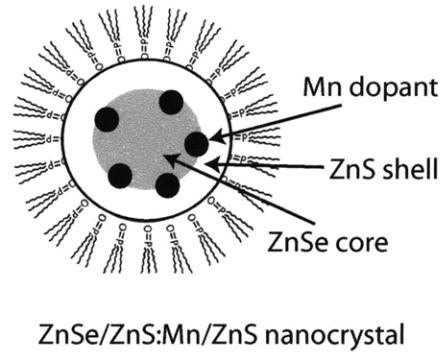


Figure 7-9: Schematic of a ZnSe/ZnS:Mn/ZnS nanocrystal.

### 7.2.1 Synthesis of Mn-doped Nanocrystals of EL

We chose to work with Mn-doped nanocrystals as Mn is the most commonly used phosphor dopant in AC-TFEL devices. Jon Halpert adapted a synthesis for ZnSe/ZnS:Mn/ZnS nanocrystals from Thakar *et al.* [77] that offers the stability and high quantum yield needed for AC-TFEL applications. The high quantum yield of these ZnSe/ZnS:Mn/ZnS nanocrystals is due to their thick ZnS shell, which localizes the excited state on the Mn dopant atom by preventing energy transfer to surface states or the surrounding medium. The thick shell also improves the stability of the nanocrystal, preventing migration of the Mn dopant. The ratio of Zn and S precursors in the overcoating step, the final ZnS shell thickness, and the ligand chemistry account for the greater quantum yield in our nanocrystals. ZnSe cores are prepared by injecting 96 mg of diethyl zinc and 0.67 ml of trioctylphosphine (TOP)-selenide into a flask of 10 ml of oleylamine, degassed at 140 °C. After heating at 270 °C for 90 minutes, the flask is cooled to 170 °C and a solution of 45 mg of manganese stearate, 76 mg of diethyl zinc, and 160 mg of hexamethyldisilathiane in 6 ml TOP is added at a rate of 1 drop per second. These ZnSe/ZnS:Mn particles are precipitated twice using methanol and butanol and redispersed in hexane. This solution is then added to a degassed flask containing 10 g of trioctylphosphine oxide (TOPO) and 0.4 g of n-hexylphosphonic acid (HPA) at 80 °C. The hexane is removed under vacuum. The flask is then placed under argon and heated to 170 °C. A solution of 80 mg diethyl

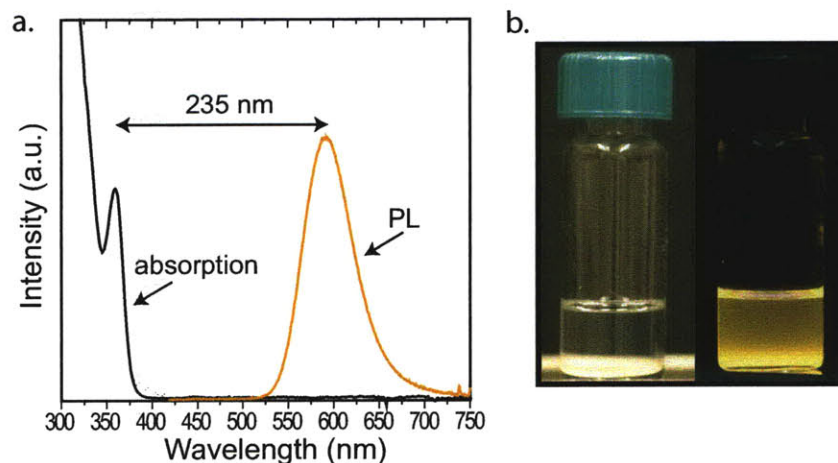


Figure 7-10: a) The absorption (black line) and photoluminescence (orange line) spectra of the ZnSe/ZnS:Mn/ZnS nanocrystals in solution show a large (235 nm) Stokes shift. b) Photographs of a vial of ZnSe/ZnS:Mn/ZnS nanocrystals in chloroform under room lighting (left) and under UV illumination (right) provide visual confirmation of the spectra shown in panel a, which indicate that these orange-emitting nanocrystals exhibit no absorption in the visible wavelength regime.

zinc and 160 mg of hexamethyldisilathiane in 5 ml TOP is added dropwise and the flask is cooled to room temperature. 4 ml of hexane and 4 ml butanol are then added. The ZnSe/ZnS:Mn/ZnS nanocrystals are finally precipitated twice using methanol and butanol and redispersed in chloroform.

Figure 7-10a shows the absorption and photoluminescence (PL) spectra for these nanocrystals in solution. As discussed previously, the nanocrystals do not absorb in the visible wavelength region because the host material, ZnSe, is a wide band gap semiconductor. The PL spectrum is centered at wavelength  $\lambda = 590$  nm, which is characteristic of the Mn phosphor transition [77]. Streak camera measurements of this photoluminescence reveal an excited state lifetime in excess of 1 ms, consistent with the expected phosphorescent emission decay mechanism. The photographs of the nanocrystals in room light and under UV illumination (Figure 7-10b) provide a visual indication of the transparency of the nanocrystals as well as their high quantum yield (QY), which we measure to be  $65 \pm 5\%$  for the nanocrystals in solution. A direct measurement of QY by comparing the solution to an organic dye is not possible due to the large Stokes shift in the ZnSe/ZnS:Mn/ZnS nanocrystals. The QY measurement

is therefore performed by comparing the nanocrystal solution to a solution of orange emitting CdSe/ZnS quantum dots with a QY of 65 %, previously calibrated to a solution of Rhodamine 610 (QY = 65 %). In addition to having a high QY, we note that the ZnSe/ZnS:Mn/ZnS nanocrystal solution also exhibits a long shelf life. Figure 7-10 shows a nanocrystal solution synthesized over one year prior to the date of the photographs.

## 7.2.2 Device Structure

The AC-TFEL device structure that enables electrical excitation of the doped nanocrystals is shown schematically in Figure 7-11. It is fabricated using room temperature radio frequency (RF) magnetron sputtered ceramics and solution deposited nanocrystals. We begin by sputtering 80 nm of an insulating metal oxide of either Al<sub>2</sub>O<sub>3</sub> or HfO<sub>2</sub> onto commercially-deposited indium tin oxide (ITO) on glass from Thin Film Devices, Inc. Both the bottom and top insulating layers are sputtered in an inert Ar environment at 4 mTorr with a power of either 150 W (for Al<sub>2</sub>O<sub>3</sub>) or 100 W (for HfO<sub>2</sub>). The sputter-deposited insulating films are complete and planar, as revealed by atomic force microscopy (AFM) characterization. For a device consisting of Al<sub>2</sub>O<sub>3</sub> layers, for example, we measure a root-mean-square (rms) surface roughness of 0.3 nm for the bottom layer and a surface roughness of 0.9 nm (rms) for the top layer. The observation of sub-1 nm roughness over a 5 μm × 5 μm area of the top insulating layers indicates that the multiple ZnS and nanocrystal layers in the middle of the device structure maintain planarity throughout the multilayer growth.

The active layer of the device consists of alternating layers of sputtered ZnS and spin cast ZnSe/ZnS:Mn/ZnS nanocrystals. Each layer of ZnS is 12 nm thick and is sputter-deposited with a power of 25 W in 4 mTorr of Ar. A thickness of 12 nm of ZnS is chosen because it is enough to form a complete layer that is not damaged upon subsequent spin-casting of the next nanocrystal layer. Thicker ZnS layers, while also complete and capable of withstanding the subsequent spin-casting steps, increase the turn on voltage of the device. The layers of nanocrystals are spin cast in a nitrogen glove box onto the ZnS at a speed of 1200 RPM from chloroform. Cross sectional AFM



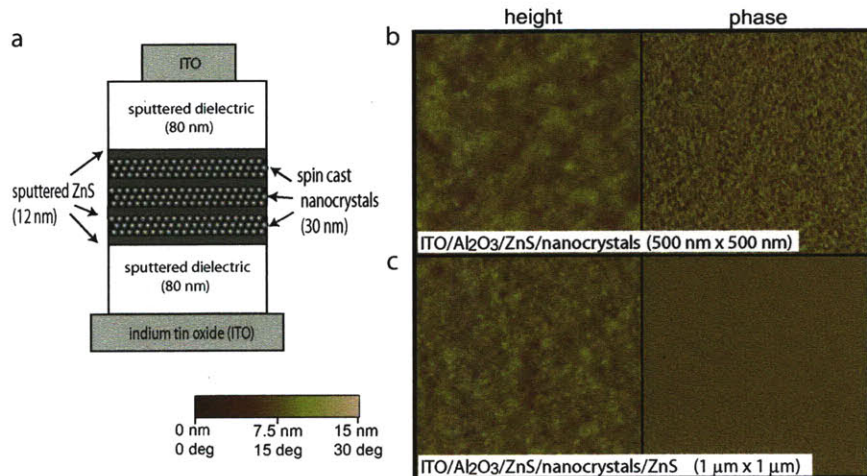


Figure 7-11: a) A schematic of the doped nanocrystal-based AC-TFEL device structure. Atomic force microscopy topographic and phase images show: b) the first layer of nanocrystals spin cast on ZnS, and c) a subsequent layer of ZnS sputtered on top of the nanocrystals. Comparison of the phase images in panels b and c shows that the nanocrystals are completely covered by the 12 nm layer of ZnS.

scans indicate that the total thickness of each layer of nanocrystals is approximately 30 nm, corresponding to approximately four to five layers of nanocrystals. Figures 7-11b and 7-11c show AFM topography and phase images of the nanocrystal layer and the first ZnS layer on top of the nanocrystals. Figure 7-11b reveals a highly monodisperse film of 5 nm diameter nanocrystals. The rms roughnesses of the two layers are 1 nm and 0.8 nm, respectively, indicating that both the nanocrystals and the ZnS form smooth, complete layers. The contrast between the phase images in Figures 7-11b and 7-11c (right hand panel) further confirms the completeness of the ZnS layer on top of the nanocrystals. The device is completed with a second, 80 nm thick insulating layer and a 150 nm thick top electrode of either ITO or Al, which are sputtered at 35 W in 4 mTorr of Ar. Use of top ITO electrodes results in a highly transparent completed structure.

In the AC-TFEL architecture presented here, the alternating layers of ZnS and nanocrystals are necessary for device electroluminescence (EL). To confirm that the ZnS layers are critical to device operation, we fabricate four devices with continuous 30 nm or 90 nm thick layers of ZnSe/ZnS:Mn/ZnS nanocrystals sandwiched between both Al<sub>2</sub>O<sub>3</sub> and HfO<sub>2</sub> dielectric layers. The 90 nm thick layer is spin cast using

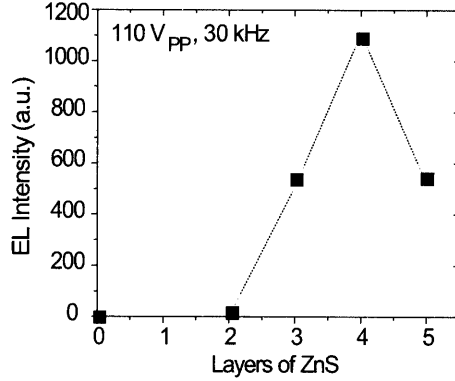


Figure 7-12: Plot of the electroluminescent (EL) intensity versus the number of layers of ZnS in the device structure. We find that for a given bias condition (here,  $100 V_{p-p}$  at 30 kHz), devices with four layers of ZnS (and three 30 nm thick layers of nanocrystals) give the largest EL response.

a more concentrated solution of nanocrystals, and its thickness and uniformity are characterized by AFM, as described previously. No EL is observed from these devices, indicating that the device luminescence is determined by the number of ZnS layer-nanocrystal interfaces and not by the number of luminescent impurity centers. To determine the optimal number of ZnS layers within the device, we fabricate structures with two, three, four, or five 12 nm thick ZnS layers (sandwiching one, two, three, or four layers of nanocrystals, each of which is 30 nm thick). 80 nm thick  $Al_2O_3$  layers are used as the dielectrics for the four devices with Al as the top contact. EL is measured while the devices are biased with a square-wave pulse at a frequency of 30 kHz and peak-to-peak voltage ( $V_{p-p}$ ) of 110 V. The trend in EL response is shown in Figure 7-12. The luminescence from the device with two layers of ZnS is below our reliable detection threshold. We find four layers of ZnS to be optimal; devices with three and five layers of ZnS (containing two or four layers of nanocrystals, respectively) exhibit lower EL intensity than the device with four ZnS layers. The device with five layers of ZnS (and 4 layers of nanocrystals) can operate at the same brightness as the four ZnS layer device, but it requires an increased operating voltage to do so because of the additional voltage drop across the insulating layers of ZnS and nanocrystals. Likewise, devices with multiple 90 nm thick nanocrystal layers exhibit electroluminescence, but they require higher operating voltages than devices with

30 nm thick nanocrystal layers to achieve the same field drop across the nanocrystal layers. These results demonstrate the importance of maximizing both the number of interfaces and the electric field dropped across the nanocrystal layers.

The following results pertain to transparent devices with four layers of ZnS and three 30 nm thick layers of nanocrystals, depicted schematically in Figure 7-11a. The photographs in Figure 7-13a provide a visual indication of device transparency, as well as the uniform illumination at  $2 \text{ Cd/m}^2$  of a  $1 \text{ mm} \times 2 \text{ mm}$  pixel with an applied voltage of  $170 V_{p-p}$  at 30 kHz. We test the device using an HP 3254A function generator, which enables us to sweep frequency across a large range with voltages up to  $200 V_{p-p}$ . Our devices show EL emission at frequencies greater than 10 kHz and with voltages as low as  $110 V_{p-p}$  (for operation at 30 kHz). Trends of increasing EL intensity as a function of both increasing voltage and increasing frequency are shown in Figure 7-13b.

These trends are consistent with impact excitation of the Mn impurity dopant whereby electrons are accelerated across the sputtered ZnS layers. However, the trends can also be explained by the QD ionization process described in Chapter 6 and Section 7.1. The high electric field across the nanocrystal layers can cause electrons to be removed from the valence band of the ZnSe cores, leaving holes behind. An electron from a neighboring nanocrystal, aided by the field, can then couple with the hole to form an exciton on the ZnSe core whose energy can be transferred to the Mn impurity dopant. Further experiments would be needed to understand in detail the mechanism that best explains the excitation of the Mn dopant in these devices.

Figure 7-14 shows the normalized EL spectra for a device with  $\text{Al}_2\text{O}_3$  (solid orange line) and  $\text{HfO}_2$  (dashed orange line) insulating layers, both operating at 30 kHz and  $170 V_{p-p}$ . The overlap of these spectra confirms that the insulating layer does not contribute to or affect the observed EL spectral shape. The dominant peaks in the two EL spectra overlap with the solution PL spectrum (gray line), indicating that the phosphor transition accounts for the EL response. The broad background emission that spans from 450 nm wavelength into the near-IR is likely a result of electrical excitation of ZnSe defect states that may be created during the sputtered ZnS layer

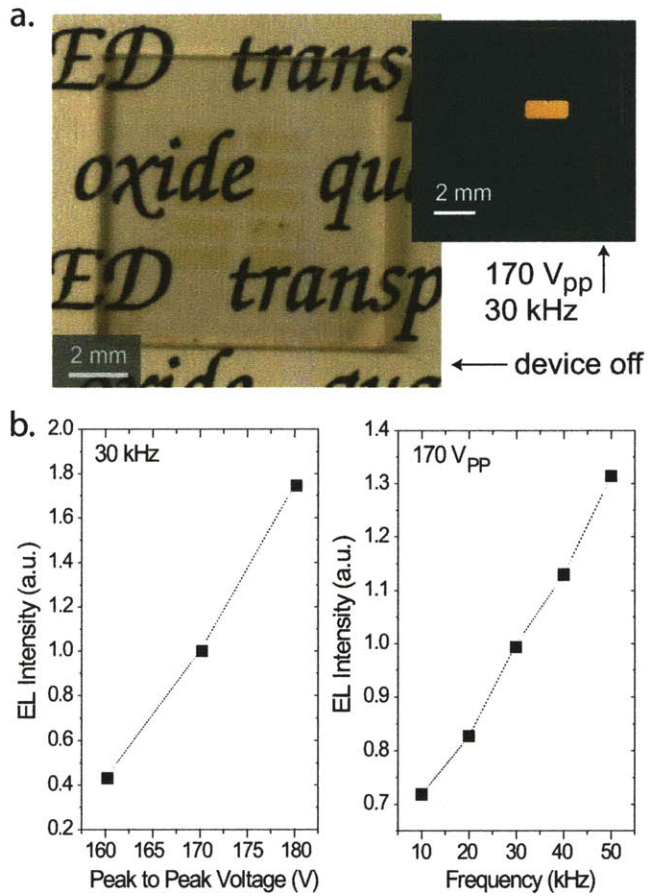


Figure 7-13: a) A photograph of a 12.7 mm  $\times$  12.7 mm glass substrate containing ten 1 mm  $\times$  2 mm AC-TFEL devices, with no bias applied. The substrate is pictured on top of printed text to demonstrate the transparency of the AC-TFEL device architecture. The inset shows the uniformity of pixel illumination (in the dark) with the device operating at 170 V<sub>p-p</sub> and 30 kHz. b) Plots of the EL response as a function of drive voltage and frequency. Values are normalized with respect to the EL response at 170 V<sub>p-p</sub> and 30 kHz.

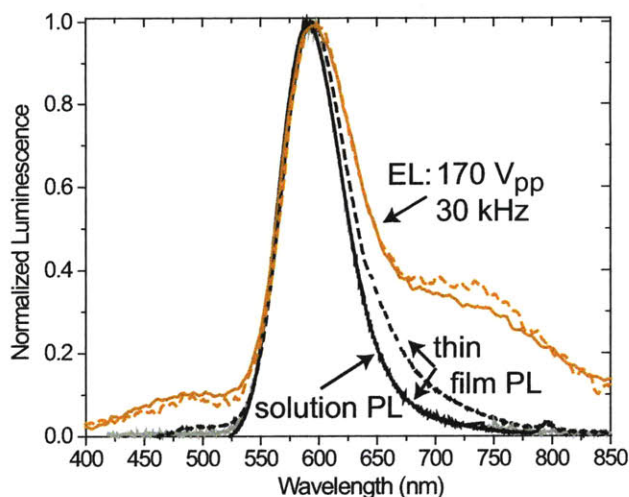


Figure 7-14: The EL spectra for devices with  $\text{Al}_2\text{O}_3$  and  $\text{HfO}_2$  insulating layers are presented by the solid and dashed orange curves, respectively. The bias conditions are  $170 \text{ V}_{\text{p-p}}$  and  $30 \text{ kHz}$ . A photoluminescence (PL) spectrum of an incomplete device structure ( $\text{ITO}/\text{Al}_2\text{O}_3/\text{ZnS}/30 \text{ nm}$  nanocrystals) (solid black curve) matches solution PL spectrum of the nanocrystals in chloroform (solid gray curve). The PL spectrum of a more complete device (consisting of  $\text{ITO}/\text{Al}_2\text{O}_3/\text{ZnS}/30 \text{ nm}$  nanocrystals/ $\text{ZnS}$ ) in which  $\text{ZnS}$  has been sputtered onto the nanocrystals is shown with the dashed black line.

deposition. These defect states could similarly be excited by exciton energy transfer from the  $\text{ZnSe}$  core. A PL spectrum (black line) of an incomplete device structure ( $\text{ITO}/\text{Al}_2\text{O}_3/\text{ZnS}/30 \text{ nm}$  nanocrystals) matches the solution PL spectrum and shows no evidence of defect states. However, the PL spectrum of a more complete structure consisting of  $\text{ITO}/\text{Al}_2\text{O}_3/\text{ZnS}/30 \text{ nm}$  nanocrystals/ $\text{ZnS}$  (dashed black line) exhibits broadening of the red and blue edges of the nanocrystal luminescence, which is indicative of defect states. The defect states are more prominent in the EL spectra than in the PL spectrum, suggesting that the PL excitation probes all nanocrystals while the EL signal is dominated by nanocrystals at the  $\text{ZnS}$  interface.

While the shape of the EL spectrum is the same regardless of the insulating layer used, the EL intensity is a factor of two less for devices using  $\text{HfO}_2$  instead of  $\text{Al}_2\text{O}_3$ . This observation is consistent with a field driven excitation mechanism. Since the static dielectric constant of  $\text{HfO}_2$  is approximately twice that of  $\text{Al}_2\text{O}_3$ , we expect that the field drop will be larger across the  $\text{HfO}_2$  layers than across the  $\text{Al}_2\text{O}_3$  layers

in otherwise comparable device structures. This implies a reduction in the electric field across the nanocrystals and ZnS in the HfO<sub>2</sub>-containing structures, which is consistent with the observed lower EL intensity of HfO<sub>2</sub>-containing structures.

In summary, we have demonstrated AC driven electroluminescence from highly efficient and stable ZnSe/ZnS:Mn/ZnS nanocrystals. Because the demonstrated device architecture is comparable to existing AC-TFEL technology, our use of spin-casting to deposit the nanocrystals in multilayer stacks highlights the viability of solution-based techniques for depositing the active phosphor layer in AC-TFEL devices, which could enable print-fabrication of transparent multicolor AC-TFEL displays.

### 7.3 Inkjet Printing of Quantum Dot Films

Solution processing of nanocrystalline colloids enables a wide range of deposition techniques such as spin-casting, microcontact printing [15], inkjet printing [49], and electro-spray [78]. Microcontact printing techniques have been used to demonstrate side-by-side patterning of nanocrystals of different emission colors with the 30 dpi pattern resolution (25 nm features) [15] necessary for high resolution displays.

One of the benefits of using metal oxide-based device architectures is that the colloidal QD solutions can be deposited directly on the metal oxides without damaging the metal oxides with the solvent. In our demonstrations of TFEL QD devices in the previous Sections, we have used spin-casting active emissive layer. Inkjet printing however is an attractive deposition technique for any large area electronics application because it minimizes material use and allows for an arbitrary number of laterally resolved patterns. In this section, we demonstrate print-deposition of high resolution, patterned, multicolored thin films of luminescent colloidal QD-polymer composites and use the printed patterns in fabricating robust, bright, full color AC-driven displays.

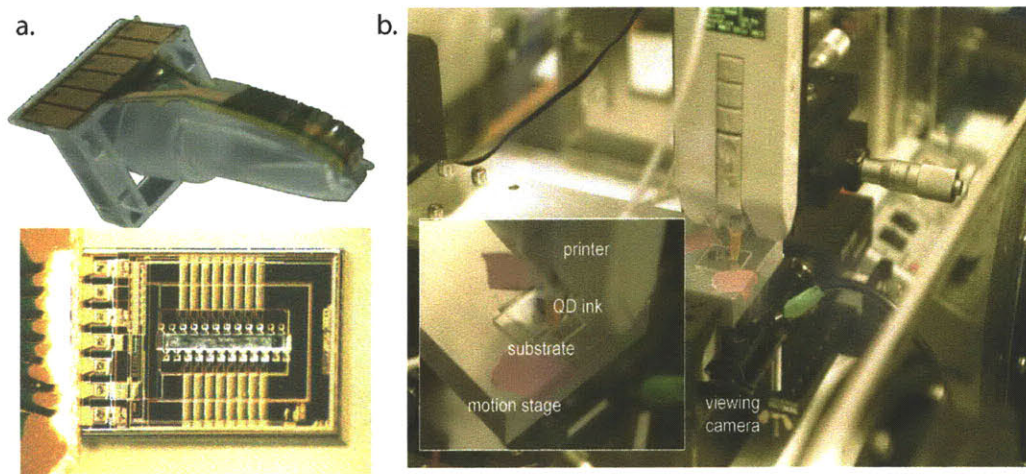


Figure 7-15: a) Photograph of the Hewlett Packard Thermal Inkjet Pico-fluidic dispensing System (TIPS) printhead. Courtesy of HP. b) Photograph of print station setup including the precision movable stage under the fixed TIPS system.

### 7.3.1 QD Ink Solutions and Printing Technique

We use a Hewlett Packard Thermal Inkjet Pico-fluidic dispensing System (TIPS) to deposit QD inks in picoliter-sized quantities on-demand. Drop volumes range from 2 pL to 220 pL and can be dispensed at up to several thousand drops per second. Drop control is achieved by controlling ejection energy (applied voltage) and length of firing pulses, and by choosing appropriate fluidic chamber dimensions, that controlled precision movable stage under the fixed TIPS system. Patterns in this work are formed with 50 pL to 30 pL drop volumes, deposited at a 50  $\mu\text{m}$  to 100  $\mu\text{m}$  pitch.

Our experiments show that it is possible to directly inkjet print QDs dispersed in a solvent, but that the structural and luminescent properties of the QD layer are improved if the QDs are embedded in an optically transparent polymer matrix [79]. Before we achieved well-defined patterns with QD-PIB composite inks, substantial work was done to find an appropriate polymer and optimize the polymer to QD ratio. Our selection criteria were that the polymer be soluble in a liquid compatible with the TIPS printhead, robust yet flexible at room temperature, and optically transparent across the visible wavelength regime. For example, chlorinated solvents such as chloroform and chlorobenzene are not compatible with the TIPS printhead.

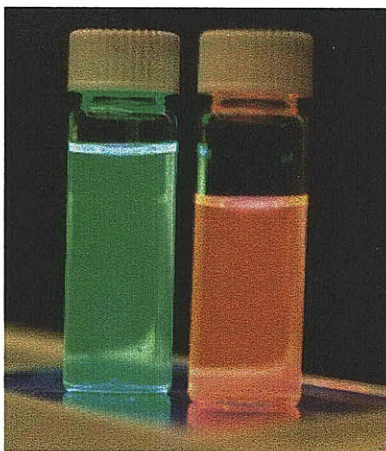


Figure 7-16: QD and polyisobutylene (PIB) ink solutions under UV illumination.

We select 400,000 molecular weight polyisobutylene (PIB) dissolved in hexane and octane (0.1 g PIB per 10 mL hexane and 1 mL of octane). This PIB solution is mixed with a 2 mg/ml concentration of quantum dots (QDs) in hexane in proportions of one part PIB solution to between two and four parts QD solution to form the printable ink solutions. Examples of these QD ink solutions are shown in Figure 7-16.

One challenge in inkjet printing a uniform thin film is avoiding the “coffee ring” phenomenon, whereby solutes migrate to the edge of a printed drop during the drying process, forming a thin film of uneven thickness [80, 81]. Previous studies have shown that two-solvent techniques can be used to achieve greater uniformity of inkjet printed films and to facilitate deposition of QDs [82]. Figure 7-17 compares inkjet printed lines of QDs in hexane/octane (9:1) and a solution of inkjet QD-PIB composite in hexane/octane (9:1). The PIB-composite is more uniform with less “coffee-stain effect”. Identical printing conditions of 180 pL per drop, 2 drops per burst, an energy of 29.25 V per burst, and 4.4  $\mu$ s pulse width were used for both samples.

We also worked to optimize the hexane to octane ratio to reduce non-uniform drying patterns and enable thin films with QDs evenly suspended in a PIB matrix. Because octane has a higher boiling point than hexane, addition of octane into the ink solution facilitates printing by increasing the drying time of the ink and thereby reducing the likelihood of caking of QDs on the printhead nozzle. However, addition of octane also delays the drying time of the printed pattern, leading to migration



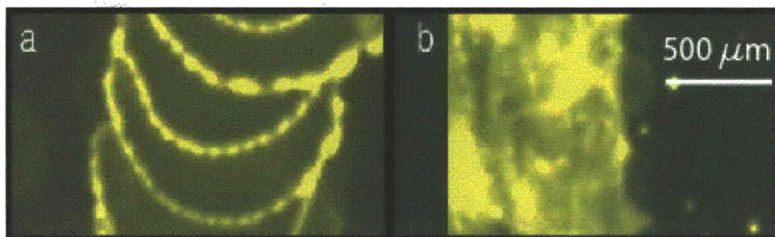


Figure 7-17: Fluorescence microscope images of an inkjet printed line using solutions of (a) QDs in hexane/octane (9:1) and (b) QDs and PIB in hexane/octane (9:1). Identical inkjet printing settings were used for both solutions.

of the QDs in the pattern after deposition. Figure 7-18 shows optical microscope images and photographs of printed QD-PIB composites ( $3\text{ mm} \times 5\text{ mm}$ ) where the PIB solution is 0.1 g PIB per 1 mL hexane and 9 mL of octane (Figure 7-18a) and 0.1 g PIB per 5 mL hexane and 5 mL of octane (Figure 7-18b). We continued to reduce the amount of octane in the PIB solution to arrive at the 0.1 g PIB per 10 mL hexane and 1 mL of octane used to achieve the results presented elsewhere in this work. This ratio of octane to hexane reduced clogging during the printing step while still enabling high resolution printing without substantial migration of QDs in the printed pattern. By heating the substrate during inkjet printing, we can accelerate the solvent evaporation and reduce migration of QDs in the PIB-QD composite. Figures 7-18c and 7-18d show patterns generated with the same ink (based on a PIB solution of 0.1 g PIB per 9 mL hexane and 1 mL of octane) and printing conditions; however, in the case of the pattern in Figure 7-18d, the substrate was heated to  $60^\circ\text{C}$  during printing. We note that substrate heating can also cause heating of the printhead, which leads to evaporation of the ink solution and clogging of the printhead nozzle. We recommend air flow to minimize printhead heating or increasing the printhead to substrate distance. The latter option, however, is not suitable for high-resolution patterns, where increased printhead to substrate distance can reduce pattern fidelity.

A 1 mm long profilometry scan from the ITO to the top surface of a  $3\text{ mm} \times 5\text{ mm}$  QD-PIB feature (Figure 7-19a) demonstrates the edge definition and top surface uniformity achievable using large droplet sizes and high-speed printing. This feature is comprised of 15 layers of QD-PIB composite printed with 280 pL droplets at a

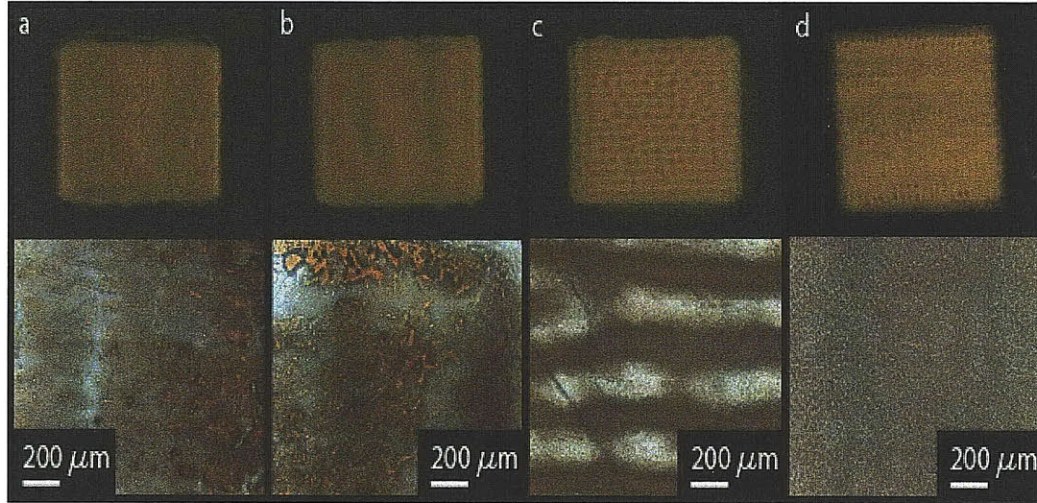


Figure 7-18: Photographs (top) and optical microscope images (bottom) of printed QD-PIB composites from inks with hexane to octane ratios of (a) 1 to 9 and (b) 1 to 1, and from an ink with a 9 to 1 hexane/octane ratio (c) without and (d) with substrate heating. All patterns were deposited with identical printhead settings.

50  $\mu\text{m}$  pitch. Figure 7-19b, which presents a fluorescence microscope image of a series of parallel lines printed using 120 pL droplets at a pitch of 250  $\mu\text{m}$ , indicates the feasibility of high-resolution patterns. Here, the QD-PIB ratio is tuned to result in 100  $\mu\text{m}$  wide lines, where each line is composed of 14 layers of the printed composite to give 2  $\mu\text{m}$  thick printed features. The lack of drift in the printed pattern over the 14 layers and the absence of “coffee ring” features highlight the level of accuracy, uniformity, and repeatability afforded in printing with a QD-polymer composite. A photograph of the MIT seal (2 cm in diameter) printed with QDs is shown in Figure 7-19c to further demonstrate the arbitrary complexity possible with inkjet printing.

Another benefit to embedding QDs in an insulating polymer matrix is the decrease in the amount of QD luminescence quenching observed in closed-packed QD structures. We measure, on average, a factor of 2.5 increase in the PL efficiency for QDs in the PIB matrix as compared to a spin coated, neat thin film of QDs. For both red and green nanoparticles, we inkjet print 10 mm  $\times$  14 mm rectangles of QD-PIB composite and spin coat solutions of the same nanoparticles on quartz substrates. We measure the PL for each QD-PIB and QD-only sample excited with a  $\lambda = 408$  nm laser and adjust for the absorption of the sample at  $\lambda = 408$  nm. The PL measure-

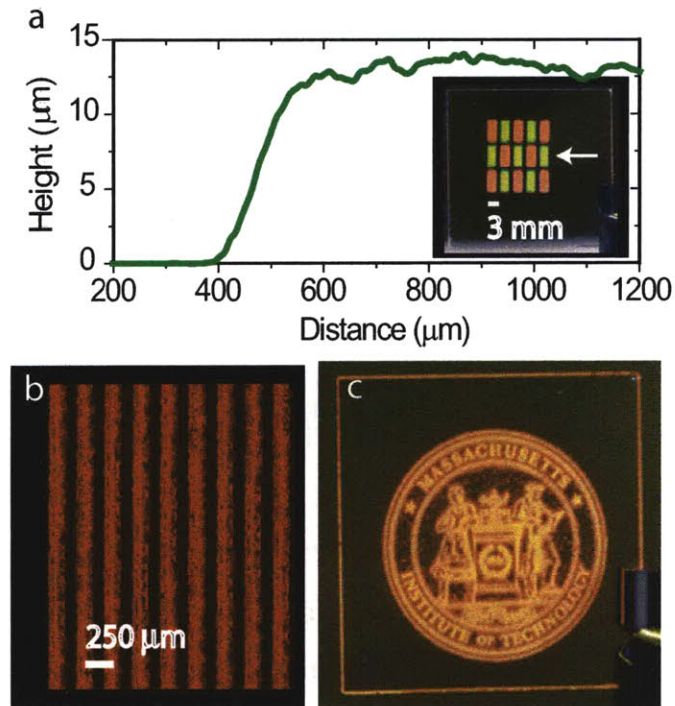


Figure 7-19: a) 1 mm profilometry scan of the edge of a green rectangular pixel measuring 3 mm  $\times$  5 mm demonstrates the edge definition and top surface uniformity of an average pixel. The inset is a photograph of a multicolor QD-PIB pattern inkjet printed on 25.4 mm  $\times$  25.4 mm indium tin oxide (ITO) coated glass and illuminated with  $\lambda = 365$  nm light. b) Luminescence microscope photograph of a series of parallel lines printed to be 100  $\mu$ m wide at 250  $\mu$ m pitch demonstrates the feasibility of printing high-resolution patterns. c) Photograph of the MIT seal printed in QDs.

ment is performed in ten different locations across each sample to account for any non-uniformities across the spin-coated and inkjet printed features.

We use inkjet printing to deposit well-defined, uniform thin films of QDs suspended in a polyisobutylene (PIB) matrix that exhibit enhanced photoluminescence (PL) efficiency over thin films of QDs. Over a period of several months we observe no aggregation of QDs in the QD-PIB ink stored in a sealed glass vial and no degradation or phase separation in printed QD-PIB thin films kept in ambient conditions, indicating a high degree of compatibility between QDs and PIB.

### 7.3.2 Optical Downconversion as Proof of Concept Devices

To demonstrate the benefits of print-deposition of high resolution, patterned, multi-colored thin films of luminescent colloidal QD-polymer composites for display technology without the complications of electrical excitation of QDs, we fabricate robust, bright, full color AC-driven displays that optically excite the QDs. Previously in this thesis, we have demonstrated the use of QD luminescent centers in thin film structures in which QDs were electrically excited. In this section, we demonstrate planar, full color AC-EL displays, which comprise luminescent thin films of QDs that absorb blue electroluminescence from a commercial phosphor powder and then emit photons at a longer wavelength characteristic of the QD bandgap.

QDs are choice materials for this type of optical excitation. The small Stokes shift of red and green-emitting QDs enables their optical excitation by blue light. This property of QDs led to the demonstration of optical downconversion using blue GaN LEDs to excite QDs in poly(lauryl) methacrylate (PLMA) and the generation of point sources of saturated color light [50]. In contrast to the earlier work by Taylor *et al.* [83] that uses a white phosphor and poly[2-methoxy-5-(2'-ethyl-hexyloxy)-1,4-phenylene vinylene] (MEH-PPV) to absorb phosphor luminescence forming MEH-PPV excitons which are then energy transferred to QDs, our devices operate entirely by long range radiative energy transfer with no short range Förster energy transfer expected. Consequently, as shown in Figure 7-20, we are not limited to red QDs, but can optically excite any QD that has a first absorption peak at a wavelength longer

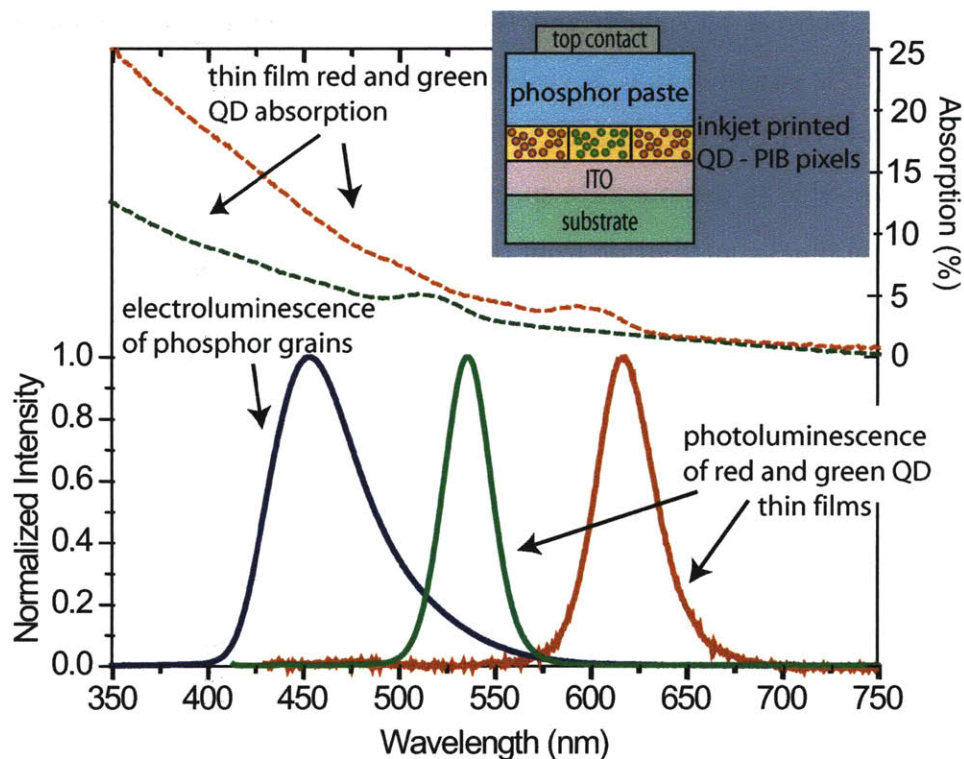


Figure 7-20: Absorption and photoluminescence spectra of spin coated thin films of red and green quantum dots (QDs) and the electroluminescence spectrum of the blue phosphor paste powered by 50 kHz AC excitation demonstrate the spectral overlaps needed to achieve optical downconversion of phosphor emission to QD film luminescence. The inset schematic depicts the cross section of an AC powder EL device structure with QD-PIB pixels.

than  $\lambda = 450$  nm.

To fabricate these devices, shown schematically in the inset of Figure 7-20, we inkjet print QD solutions onto conductive, transparent indium tin oxide (ITO) coated glass or flexible polyethylene terephthalate (PET). The inkjet printed films of QD-PIB composite are covered with a thin film of ZnS:Cu powder in an electrically insulating, transparent binder from Osram-Sylvania, that is doctor-blade deposited and dried at 50 °C. Conductive adhesive tape serves as the top electrode and defines the working device area. All fabrication and testing is done in ambient conditions and without device packaging. We observe long device shelf lives with no degradation or decrease in brightness during intermittent device testing over one year.

The spectra and photographs in Figure 7-21 show both the blue electrolumi-

nescence of the ZnS:Cu phosphors and the green and red QD spectra of optically downconverted QD emission that is visible when an AC power is applied across the device structures. Because our printing technique results in PIB/QD films of uniform thickness, we are able to demonstrate spectral purity in the optically downconverted QD light with minimal contribution from the blue phosphor EL emission. When plotted on a Commission International d’Eclairage (CIE) chromaticity diagram (Figure 7-21c), the CIE coordinates of our devices define a color triangle that is comparable to the International Telecommunication Union HDTV standard.

Previous work has shown that a solution of mixed QDs can be used to obtain colors inside the space defined by CIE coordinates of the individual QD luminescence [16, 82]. Now we demonstrate that by varying the thickness of the printed QD-PIB layer, a single QD ink solution can be used to achieve the set of colors on the trajectory between the CIE coordinates of the blue phosphor and the CIE coordinates of the particular QD lumophore. For a given printed QD-PIB thickness, we observe little change in the CIE coordinates over the entire range of applied voltages ( $50 V_{\text{rms}}$  to  $430 V_{\text{rms}}$ ). While the data in Figure 7-21 highlights the color uniformity of large ( $8 \text{ mm} \times 10 \text{ mm}$ ) rectangular pixels, it is also possible to fabricate working AC-EL devices with high-resolution features such as the lines in Figure 7-19. Figure 7-22a is a photoluminescence photograph of a completed device structure on a flexible ITO-coated PET substrate with a ruler pattern that marks off 2 mm divisions for a 1 cm shape printed to scale.

We measure luminance as a function of applied AC voltage for devices with a different number of printed red and green QD-PIB layers, as well as for blue (ZnS:Cu phosphor only) devices (Figure 7-22b). The luminance versus RMS voltage plot highlights the tradeoff between spectral purity and brightness at a specific driving voltage. As shown in Figure 7-22b, the spectral purity, defined as the fraction of the device electroluminescence spectrum comprised of QD emission, increases as a function of the number of QD-PIB layers. The downconversion efficiency, which we define as the ratio of the watts of QD emission collected to the watts of the phosphor emission created, decreases as a function of the number of QD-PIB layers. These



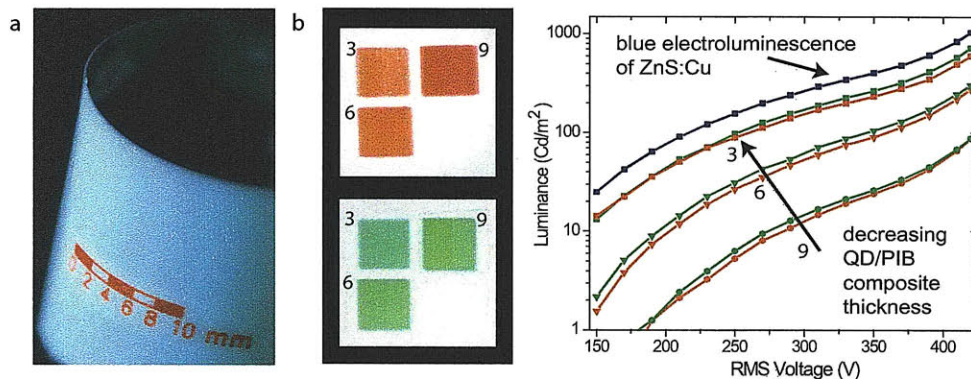


Figure 7-22: a) Photograph of a completed device on a flexible substrate under  $\lambda = 365$  nm wavelength illumination. The ruler pattern printed with red QD-PIB ink is to scale. b) Photographs of the photoluminescence devices with three, six, and nine layers of inkjet printed QD-PIB, under  $\lambda = 365$  nm wavelength illumination, provide a visual indication of the color purity. The plot shows luminance versus applied rms voltage for a blue (ZnS:Cu phosphor only) pixel, as well as the red and green pixels with three, six, and nine layers of QD-PIB.

trends provide insight into the performance of our devices. For a thin QD-PIB layer ( $2\ \mu\text{m}$  thick), we measure downconversion efficiencies near 12%. This is consistent with the 15% PL efficiency of the QDs in the PIB matrix with additional losses due to QD light self-absorption. As the thickness of the QD-PIB layer increases, less blue light reaches the QDs furthest from the phosphor layer, while lower energy emission from the layer of QDs closest to the phosphor is subject to more scattering and reabsorption. The luminous efficiency of our red emitting devices is directly related to the efficiency of the blue phosphor, which is often reported to be between 5 lm/W and 10 lm/W [69].

### 7.3.3 Enhanced Device Luminescence using Metal Oxide Thin Films

We use this downconversion device to demonstrate that metal oxide layer thickness can play an important role in the device luminance due entirely to thin film reflection, such as optical outcoupling. Device luminance can be increased when additional transparent metal oxide layers are inserted into the device structure. We limit our



choice of metal oxides to materials that are robust insulators, such as  $\text{Al}_2\text{O}_3$  and  $\text{ZnO}$ , and investigate device structures with metal oxides on either side of the QD-PIB composite layer, such as the one shown schematically in the inset of Figure 7-23a.

To determine the layer thicknesses of the metal oxides needed to simultaneously maximize absorption of the phosphor luminescence by the QDs and the transmission of the QD luminescence through the glass to the viewer, we model the device as a dielectric stack. We use a transmission and propagation numerical simulation matrix method [84]. For each interface (a, b, c, ...) and layer (1, 2, ... n), we find solutions to:

$$\begin{bmatrix} E_{1b}^+ \\ E_{1b}^- \end{bmatrix} = \frac{1}{t} \begin{bmatrix} 1 & r \\ r & 1 \end{bmatrix} \begin{bmatrix} E_{2b}^+ \\ E_{2b}^- \end{bmatrix}$$

$$\begin{bmatrix} E_{1a}^+ \\ E_{1a}^- \end{bmatrix} = \frac{1}{t} \begin{bmatrix} e^{-i\beta} & 1 \\ 1 & e^{-i\beta} \end{bmatrix} \begin{bmatrix} E_{1b}^+ \\ E_{1b}^- \end{bmatrix}$$

The first equation describes the matching conditions for the forward and reverse traveling electric field amplitudes at a boundary  $b$ , where  $r$  and  $t$  are the reflection and transmission Fresnel coefficients for a wave incident from material 1 to material 2. The second matrix equation relates to the propagation of an electric field through material 1 by matching the forward and reverse electric field amplitudes between boundary  $a$  and boundary  $b$ , which are separated by the thickness  $d$  of layer 1. The coefficient  $\beta$  is defined to be

$$\beta = \frac{2\pi\tilde{n}d}{\lambda}$$

where  $\tilde{n}$  is the complex index of refraction of layer 1. The simulation accounts for the wavelength dependence of the absorption and emission profiles of the different layers. We apply the Maxwell-Garnett mixing rule relation to determine values of the index of refraction for the phosphor ( $n = 2.3$ ) and the QD-PIB layer ( $n = 1.8$ ). The complex part of the QD index of refraction is calculated from the absorption data of QD-PIB films printed on glass substrates.

We find that  $\text{ZnO}$ , which has an index of approximately 2.0 in the visible wave-

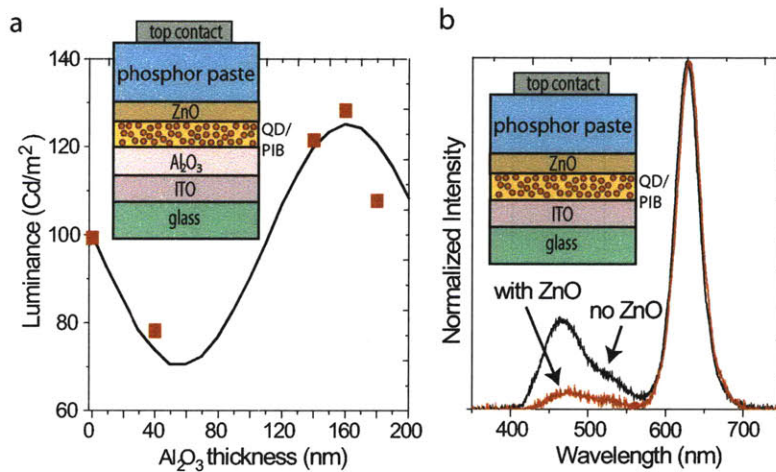


Figure 7-23: a) Data are taken from devices with 50 nm thick ZnO layers and variable thickness Al<sub>2</sub>O<sub>3</sub> transparent metal oxide layers, positioned as shown with the inset schematic. The plot shows measured (data points) and modeled (black line) device luminance as a function of Al<sub>2</sub>O<sub>3</sub> layer thickness. The data follow the oscillatory trend predicted by the model described in the text. b) The electroluminescence spectra for devices with and without a 20 nm ZnO layer indicate that the ZnO contributes to waveguiding of the phosphor electroluminescence in the plane of the substrate which facilitates an improved color purity of the emission. The inset schematic shows the placement of the ZnO layer in the device structure.

length range, is a desirable buffer layer between the phosphor and the QD-PIB matrix as it laterally waveguides some of the phosphor electroluminescence, which facilitates an improved color purity of the top surface QD emission. To minimize waveguiding of the QD emission in the ITO layer (refractive index  $\sim 2.0$ ), the lower index  $\text{Al}_2\text{O}_3$  ( $\sim 1.6$ ) can be inserted between the ITO and the QD-PIB layer. Our model indicates that transmission of QD luminescence to the viewer is maximized using a 50 nm thick layer of ZnO and a 160 nm thick layer of  $\text{Al}_2\text{O}_3$ . To demonstrate that predicted trends in luminance are indeed observed, we fabricate devices with layers of ZnO and/or  $\text{Al}_2\text{O}_3$  deposited with RF magnetron sputtering as described previously. The devices shown in Figure 7-23a contain  $\text{Al}_2\text{O}_3$  film thicknesses of 0 nm, 40 nm, 140 nm, 160 nm, and 180 nm on ITO, followed by nine inkjet printed QD-PIB layers, and 50 nm of ZnO. Figure 7-23a plots luminance measured at  $420 V_{\text{rms}}$  and 31 kHz versus  $\text{Al}_2\text{O}_3$  thickness for these devices. The data follow the oscillatory trend predicted by the optical modeling. To demonstrate the waveguiding effect in the ZnO layer, we fabricate two devices, one with and one without a 20 nm layer of ZnO on top of the QD-PIB composite. As shown by the device electroluminescence spectra in Figure 7-23b, the ZnO layer waveguides the phosphor emission in the plane of the substrate, decreasing the transmission of blue light to the viewer while still allowing excitation of the QDs. The demonstrated use of sputtered metal oxide films in the device structures confirms that the inkjet printing technique is compatible with AC thin film EL devices in which two thick insulating layers, such as  $\text{Al}_2\text{O}_3$ , surround a crystalline phosphor layer.

### 7.3.4 Electrical Excitation of Inkjet Printed Active Layers

This work introducing metal oxide layers into the optical downconversion device highlights the fact that a metal oxide layer can be deposited on top of an inkjet printing pattern. In Section 7.1, we showed that TFEL device stability improved when the QDs were embedded in a polymer matrix. Using the techniques presented in this section for achieving smooth and uniform inkjet printed layers, we deposited an QD-polymer in a TFEL structure (See Figure 7-24a). Figure 7-24b shows a photograph

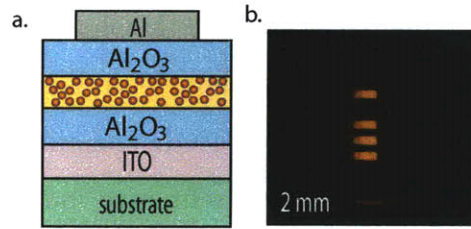


Figure 7-24: a) Schematic diagram of a thin film EL device using an inkjet printed QD-polymer active layer. b) A photograph of a TFEL device biased at  $130 V_{p-p}$  and 30 kHz.

of QD emission from a TFEL device with an inkjet printed polymer-QD active layer.

In summary, we developed QD thin film electroluminescent (TFEL) structures that sandwich QDs between two insulating metal oxide layers, and used these structures to confirm that QD ionization is responsible for EL. These TFEL structures enabled EL from QDs emitting throughout the visible and near infrared parts of the spectrum, and the first demonstration of EL from nanocrystals with phosphor doped-core/shell structures. Using these metal oxide TFEL as a platform, we demonstrated a simple and scalable method to achieve patterned pixels for a flexible, full color, large area, AC-driven display. The QD-polymer composite used to form stable ink solutions contributes to an efficient and robust device architecture.

# Chapter 8

## Conclusion

### 8.1 Thesis Summary

QD-LEDs are of interest for applications such as thin film displays with improved color saturation and white lighting with high color rendering index. To date, the most efficient visible-emitting QD-LEDs involve a monolayer of QDs sandwiched between organic charge transport layers; however, the use of molecular organic materials as charge transport layers introduces fabrication challenges similar to those facing organic LEDs (OLEDs), namely the need for packaging in order to prevent degradation due to atmospheric oxygen or water vapor exposure.

This thesis introduced methods for integrating colloiddally synthesized quantum dots (QDs) and metal oxides into air-stable optoelectronic devices, presented the three distinct light emitting devices (LEDs) with metal oxides surrounding a QD active layer, and used these novel metal oxide based QD-LEDs to study mechanisms for electrical excitation of QDs.

We report the first all-inorganic QD-LED with n- and p-type metal oxide charge transport layers. This QD-LED has uniformly emitting pixels with a peak luminance of nearly 2000 Cd/m<sup>2</sup> and an extended shelf life, but it has limited efficiency and only enables excitation of red-emitting colloidal QDs. By characterizing the QD and metal oxide layers using atomic force microscopy, photoluminescence spectroscopy, x-ray diffraction, and ultraviolet photoelectron spectroscopy, we determine the physical

origins of these limitations and present design rules that enable systematic improvement of QD-LED efficiency and electrical excitation red, green, and blue-emitting QDs from the same air-stable device structure. Despite this success, we recognize that unlike QD-LEDs with organic charge transport layers which benefit from the concomitant roles of both Förster energy transfer and direct charge injection, QD-LEDs with metal oxide charge transport layer operate solely via direct charge injection, requiring device designs to be based largely on energy band alignment considerations.

We therefore develop a unipolar, n-i-n light emitting device architecture which highlights the possibility for a paradigm shift away from direct charge injection into QDs as a means for electroluminescence (EL) in inorganic-based QD-LED structures. These devices are the first reported example of DC-field driven EL in QDs. Using rational insertion of a thin film of insulating ZnS, we demonstrate our understanding and control over this novel mechanism of QD excitation, which we explain via electron extraction from the valence band of the QDs under high field. This unipolar device structure solves two major challenges facing QD light emitting technology: it eliminates the need for packaging to prevent degradation due to atmospheric oxygen or water vapor exposure and it reduces the need for complicated band alignment engineering. We demonstrate EL using both green and red QDs and constant luminance from the device over 20 hours of continuous operation in air, unpackaged. Our most efficient devices exhibit a peak luminance of 1000 Cd/m<sup>2</sup> with a record luminous efficiency 2 Cd/A from both faces of the device.

To further understand field driven excitation mechanisms in QDs, we develop QD thin film electroluminescent (TFEL) structures, which sandwich QDs between two insulating metal oxide layers. Because no current is transported through the TFEL devices, the need for alignment of energy bands is eliminated, and EL from QDs with emission peaks at wavelengths from 450 nm to 1500 nm can be achieved in the same device structure. We confirm that our electron extraction mechanism is again responsible for EL by demonstrating the correlation between the QD band gap and the electric field required for EL. This structure also enables the first demonstration of EL from novel QDs such as nanocrystals with phosphor doped-core/shell

structures, which offer the possibility of a solution processed active layer in TFEL signage, which currently requires high temperature, vacuum-based deposition techniques. Indeed, one attractive feature of metal oxide surfaces is their compatibility with a variety of QD deposition techniques including spin coating, contact printing, and inkjet printing. Printing techniques are desirable because they reduce material waste and allow patterned pixels for side-by-side red, green, and blue emission. We demonstrate inkjet printing of QDs and QD-polymer composites for the fabrication of high resolution or large area, full-color, AC driven displays on flexible substrates.

## 8.2 Future Directions

This research has enabled air-stable devices that improve on existing QD-based display and lighting solutions and led to the discovery of field-driven electroluminescence from QDs. More broadly, this work demonstrated that metal oxide and QDs can be successfully integrated into optoelectronic devices and that metal oxide QD-LEDs can be used as a platform for studying QD physics.

The work presented in Chapters 6 and 7 demonstrated for the first time that QD ionization can be used as a method for generating the charge carriers necessary for electroluminescence (EL) and offers the possibility for further study. Experimental investigation and computational modeling of this process could aid in the design of novel nanostructures, such as barbells [85], that optimize the efficiency of QD ionization and the subsequent EL. For example, a nanostructure consisting of a QD attached to a quantum rod could be designed to facilitate the ionization and recombination processes. Upon application of an electric field, the electron and hole would spatially separate within the nanostructure (with electron or hole leaving the QD for the rod portion of the nanostructure). When the polarity of the applied bias is switched, the electron and hole would then recombine in the QD. In this design, the entire ionization and recombination process would occur in the nanostructure so that the nanostructures themselves could be electrically isolated from each other (e.g. in an acrylic polymer) so that, as discussed in Sections 2.4 and 7.1, the luminescent

efficiency of the film is preserved.

In addition to aiding in the development of multicolor, flexible, and air-stable LEDs, this work presented in this thesis informs other QD-based optoelectronics research, such as the development of QD solar cells, QD photodetectors, and QD lasers. Because QD size and chemistry can be selected to create generate a specific absorption spectrum, QDs offer the possibility of optically optimized solar cells. For example, one can envision a tandem solar cell in which blue, red, and IR light absorbing QD layers are arranged to ensure that the majority of incoming photons are absorbed in a layer where the energy for exciton formation in that layer is comparable to the absorbed photon energy so that excess energy is not lost as heat via phonons. Progress towards such a multilayer structure has been realized in the form of a heterojunction solar cell incorporating a light absorbing CdSe QD layer and TPD as a hole-transporting organic layer [86]. This device was inspired in part by the hybrid QD and organic LED structures, and, for instance, makes use of a contact printed QD layer, which was first developed to enable multicolor QD-LEDs. Similarly, the methods for integrating QDs and metal oxides introduced in thesis will perhaps find use in the developing the first metal oxide-based QD solar cells. Furthermore, the methods for characterizing the metal oxide and QD layers and the study of direct charge injection from the metal oxides into the QDs presented in Chapter 5 will facilitate the rational design of devices to enable effective charge extraction from QDs.

Electrically driven colloidal QD lasers are perhaps the holy grail of QD optoelectronic research, promising a laser source that is spectrally tunable by simply changing the size of the QDs used as the active gain medium. Because of the strong, 3D electronic confinement in QDs and the resulting quantization of the electronic states, a QD laser is predicted to have low and temperature-independent threshold and high-frequency modulation with negligible chirping effects (small linewidth enhancement). Epitaxially grown QD lasers have shown evidence of low thresholds, temperature independence, and high gain; however, these effects are anticipated to be even more dramatic in a laser that uses colloidal QDs, which have a narrower size distribution and can be easily deposited in densely packed multilayers [87].



In this thesis, we introduced metal oxide charge transport layers that support high current densities and bring us one step closer toward the goal of an electrically pumped colloidal QD laser. Simultaneously, other groups have focused on advancing QD synthesis. Recently, thick shell QDs have been reported to suppress blinking [37, 47], which has been linked to suppressed Auger recombination and increased the optical gain [88]. Furthermore new work replacing organic aliphatic ligands on QDs with metal chalcogenide ligands has enabled QD films that exhibit record electronic transport properties [38]. Combining our work on metal oxide-based structures with these advancements in colloidal QD synthesis may be the key to achieving the high exciton density and slowed recombination rates necessary to achieve electrically-driven colloidal QD lasing.



# Bibliography

- [1] Anikeeva, P. O., Halpert, J. E., Bawendi, M. G. & Bulović, V. QD-LEDs with electroluminescence tunable over the entire visible spectrum. *Nano Lett.*, 9:2532–2536, 2009.
- [2] S.A. Empedocles. *Detection and Spectroscopy of Single CdSe Nanocrystallite Quantum Dots*. PhD thesis, Massachusetts Institute of Technology, 1999.
- [3] L. L. Hench and J. K. West. *Principles of Electronic Ceramics*. John Wiley and Sons, New York, 1990.
- [4] *Light's Labour's Lost - Policies for Energy Efficient Lighting*. International Energy Agency, 2006.
- [5] E. F. Schubert. *Light Emitting Diodes*. Cambridge University Press, 2006.
- [6] S. Reineke, F. Lindner, G. Schwartz, N. Seidler, K. Walzer, B. L ussem, K. Leo. White organic light-emitting diodes with fluorescent tube efficiency. *Nature*, 459:234–238, 2009.
- [7] J. Chen. *Novel Patterning Techniques for Manufacturing Organic and Nanostructured Electronics*. PhD thesis, Massachusetts Institute of Technology, 2007.
- [8] J. Yu. *Improving OLED Technology for Displays*. PhD thesis, Massachusetts Institute of Technology, 2008.
- [9] C.B. Murray, D.J. Norris, M.G. Bawendi. Synthesis and characterization of nearly monodisperse CdE (E = sulfur, selenium, tellurium) semiconductor nanocrystallites. *J. Am. Chem. Soc.*, 115:8706–8715, 1993.

- [10] V.L. Colvin, K.L. Cunningham, A.P. Alivisatos. Electric field modulation studies of optical absorption in CdSe nanocrystals Dipole character of the excited state. *J. Chem. Phys.*, 101:7122–7138, 1994.
- [11] B.O. Dabbousi, M.G. Bawendi, O. Onitsuka, M.F. Rubner. Electroluminescence from CdSe quantum-dot/polymer composites. *Applied Physics Letters*, 66:1316–1318, 1995.
- [12] S. Coe, W.-K. Woo, M.G. Bawendi, V. Bulovic. Electroluminescence from single monolayers of nanocrystals in molecular organic devices. *Nature*, 420:800–803, 2002.
- [13] Anikeeva, P. O., Madigan, C. F., Halpert, J. E., Bawendi, M. G. & Bulović, V. Electronic and excitonic processes in light-emitting devices based on organic materials and colloidal quantum dots. *Phys. Rev. B*, 78:085434, 2008.
- [14] S. Coe-Sullivan. Materials research society. December 2008.
- [15] L. Kim, P.O. Anikeeva, S.A. Coe-Sullivan, J.S. Steckel, M.G. Bawendi, V. Bulović. Contact printing of quantum dot light-emitting devices. *Nano Lett.*, 8:4513–4517, 2008.
- [16] Anikeeva, P.O., Halpert, J.E., Bawendi, M.G. & Bulović, V. Electroluminescence from a mixed red-green-blue colloidal quantum dot monolayer. *Nano Lett.*, 7:2196–2200, 2007.
- [17] A. H. Mueller, M.A. Petruska, M. Achermann, D. J. Werder, E.A. Akhadov, D.D. Koleske, M.A. Hoffbauer, V.I. Klimov. Multicolor light-emitting diodes based on semiconducting nanocrystals encapsulated in GaN charge injection layers. *Nano Lett.*, 5:1039–1044, 2005.
- [18] M. Achermann, M.A. Petruska, D.D. Koleske, M.H. Crawford, V.I. Klimov. Nanocrystal-Based Light-Emitting Diodes Utilizing High-Efficiency Nonradiative Energy Transfer for Color Conversion. *Nano Lett.*, 6:1396–1400, 2006.

- [19] J.W. Stouwdam, R.A.J. Janssen. Red, green, and blue quantum dot LEDs with solution processable ZnO nanocrystal electron injection layers. *J. Mat. Chem.*, 18:1889–1894, 2008.
- [20] K.S. Cho et al. High-performance crosslinked colloidal quantum-dot light-emitting diodes. *Nature Photonics*, 3:341–345, 2009.
- [21] D. J. Norris. Electronic Structure in Semiconductor Nanocrystals. In *Semiconductor and Metal Nanocrystals: Synthesis and Electronic and Optical Properties*. Marcel Dekker Ltd, 2003.
- [22] M.A. Hines, P. Guyot-Sionnest. Synthesis and Characterization of Strongly Luminescing ZnS-Capped CdSe Nanocrystals. *J. Phys. Chem.*, 100:468–471, 1996.
- [23] B. O. Dabbousi, J. Rodriguez-Viejo, F. V. Mikulec, J. R. Heine, H. Mattoussi, R. Ober, K. F. Jensen, M. G. Bawendi. (CdSe)ZnS Core-Shell Quantum Dots: Synthesis and Characterization of a Size Series of Highly Luminescent Nanocrystallites. *J. Phys. Chem. A*, 101:9463–9475, 1997.
- [24] J. E. Halpert. *Design and synthesis of nanocrystal heterostructures for optoelectronic applications*. PhD thesis, Massachusetts Institute of Technology, 2008.
- [25] X. Zhong, M. Han, Z. Dong, T. J. White, W. Knoll. Composition-Tunable  $Zn_xCd_{1-x}Se$  Nanocrystals with High Luminescence and Stability. *J. Amer. Chem. Soc.*, 125:8589–8594, 2003.
- [26] S. A. Ivanov, J. Nanda, A. Piryatinski, M. Achermann, L. P. Balet, I. V. Bezel, P. O. Anikeeva, S. Tretiak, V. I. Klimov. Light Amplification Using Inverted Core/Shell Nanocrystals: Towards Lasing in the Single-Exciton Regime. *J. Phys. Chem. B*, 108:10625–10630, 2004.
- [27] J.S. Steckel, P. Snee, S. Coe-Sullivan, J.P. Zimmer, J.E. Halpert, P.O. Anikeeva, L.-A. Kim, V. Bulović, M.G. Bawendi. Color-Saturated Green-Emitting QD-LEDs. *Angew. Chem. Int. Ed.*, 45:5796–5799, 2006.

- [28] X. Zhong, Y. Feng, W. Knoll, M. Han. Alloyed  $Zn_xCd_{1-x}S$  Nanocrystals with Highly Narrow Luminescence Spectral Width. *J. Amer. Chem. Soc.*, 125:13559–13563, 2003.
- [29] J. M. Pietryga, D. J. Werder, D. J. Williams, J. L. Casson, R. D. Schaller, V. I. Klimov, J. A. Hollingsworth. Utilizing the lability of lead selenide to produce heterostructured nanocrystals with bright, stable infrared emission. *J. Am. Chem. Soc.*, 130:4879–4885, 2008.
- [30] A. Sacra, D.J. Norris, C.B. Murray, M.G. Bawendi. Stark Spectroscopy of CdSe nanocrystallites: this significance of transition linewidths. *J. Chem. Phys.*, 103:5236–5245, 1995.
- [31] A. Sacra. *Stark spectroscopy of cadmium Selenide (CdSe) nanocrystallites*. PhD thesis, Massachusetts Institute of Technology, 1996.
- [32] S.A. Empedocles, M.G. Bawendi. Quantum-Confined Stark Effect in Single CdSe Nanocrystallite Quantum Dots. *Science*, 278:2114–2117, 1997.
- [33] V.L. Colvin, K.L. Cunningham, A.P. Alivisatos. Electric field modulation studies of optical absorption in CdSe nanocrystals: Dipole character of the excited state. *J. Chem. Phys.*, 101:7122–7138, 1994.
- [34] S.A. Empedocles, D.J. Norris, M.G. Bawendi. Photoluminescence Spectroscopy of Single CdSe Nanocrystallite Quantum Dots. *Phys. Rev. Lett.*, 77:3873–3876, 1996.
- [35] M. Drindić, M.V. Jarosz, M.Y. Morgan, M.A. Kastner, M.G. Bawendi. Transport propert of annealed CdSe collidal nanocrystal solids. *J. Appl. Phys.*, 92:7498–7503, 2002.
- [36] V.J. Porter, S. Geyer, J.E. Halpert, M.A. Kastner, M.G. Bawendi. Photoconduction in Annealed and Chemically Treated CdSe/ZnS Inorganic Nanocrystal Films. *J. Phys. Chem. C*, 112:2308–2316, 2008.

- [37] Y. Chen et al. "Giant" Multishell CdSe Nanocrystal Quantum Dots with Suppressed Blinking. *J. Amer. Chem. Soc.*, 130:5026–5027, 2008.
- [38] M. V. Kovalenko, M. Scheele, D. V. Talapin. Colloidal Nanocrystals with Molecular Metal Chalcogenide Surface Ligands. *Science*, 324:1417–1420, 2009.
- [39] N. Y. Morgan, C.A. Leatherdale, M. Drinić, M.V. Jarosz, M.A. Kastner, M.G. Bawendi. Electronic Transport in films of colloidal CdSe nanocrystals. *Phys. Rev. B*, 66:075339, 2002.
- [40] A. L. Efros, B. I. Shklovskii. Coulomb gap and low temperature conductivity of disordered systems. *J. Phys. Chem. C.*, 8:L49–L51, 1975.
- [41] W. Xue, P.A. Lee. Monte Carlo simulations of the electron glass. *Phys. Rev. B*, 38:9093–9098, 1988.
- [42] M. Nirmal, B. O. Dabbousi, M. G. Bawendi, J. J. Macklin, J. K. Trautman, T. D. Harris, L. E. Brus. Fluorescence Intermittency in single cadmium selenide nanocrystals. *Nature*, 383:802–804, 1996.
- [43] A.L. Efros. Almost always bright. *Nature Mat.*, 7:612–613, 2008.
- [44] A.L. Efros, M. Rosen. Random Telegraph Singal in the Photoluminescence Intensity of a Single Quantum Dot. *Phys. Rev. Lett.*, 78:1110–1113, 1997.
- [45] V.I. Klimov, A.A. Mikhailovsky, D.W. McBranch, C.A. Leatherdale, M.G. Bawendi. Quantization of multiparticle Auger rates in semiconductor quantum dots. *Science*, 287:1011–1013, 2000.
- [46] G. Nair. *Many Body Processes in the Photophysics of Colloidal Semiconductor Nanocrystals*. PhD thesis, Massachusetts Institute of Technology, 2009.
- [47] B. Mahler, P. Spinicelli, S. Buil, X. Quelin, J.-P. Hermier, B. Dubertret. Towards non-blinking colloidal quantum dots. *Nature Materials*, 7:659–664, 2008.

- [48] K.T. Shimizu, W.K. Woo, B.R. Fisher, H.J. Eisler, M.G. Bawendi. Surface-Enhanced Emission from Single Semiconductor Nanocrystals. *Phys. Rev. Lett.*, 89:117401, 2002.
- [49] V. Wood, M.J. Panzer, J. Chen, M.S. Bradley, J.E. Halpert, M.G. Bawendi, V. Bulović. Inkjet-Printed Quantum Dot-Polymer Composites for Full-Color AC-Driven Displays. *Adv. Mat.*, 21:2151–2155, 2009.
- [50] J. Lee, V.C. Sundar, J.R. Heine, M.G. Bawendi, R. Jensen. Full color emission from II-VI semiconductor quantum dot-polymer composites. *Adv. Mat.*, 12:1102–1105, 2000.
- [51] Ch. Arens, N. Roussau, D. Schikora, K. Lischka, O. Schöps, E. Herz, U. Woggon, D. Litvinov, D. Gerthsen, M. V. Artemyev. Colloidal nanocrystals integrated in epitaxial nanostructures: structural and optical properties. *physica status solidi (c)*, 3:861–864, 2006.
- [52] A. Pourret, P. Guyot-Sionnest, J. W. Elam. Atomic Layer Deposition of ZnO in Quantum Dot Thin Films. *Adv. Mat.*, 21:232–235, 2009.
- [53] W.H. Class. Basics of Plasmas. In *The Book of Basics*. Materials Research Corporation, 1982.
- [54] K. Wasa and M. Kitabatake and H. Adachi. *Thin Film Materials Technology: Sputtering of Compound Materials*. William Andrew Publishing, New York, 2004.
- [55] P. D. Davidse and L. I. Maissel. Dielectric Thin Films through RF Sputtering. *J. Appl. Phys.*, 37:574–579, 1966.
- [56] S. Rosnagel. Sputtering and Sputter Deposition. In *Handbook of Thin Film Deposition: Principles, Methods, Equipment, and Applications*. Noyes Publications, 2002.
- [57] S. R. Elliot, editor. *Physics of Amorphous Materials*. Longman, New York, 1983.



- [58] V. E. Henrich and P. A. Cox. *The Surface Science of Metal Oxides*. Cambridge University Press, Cambridge, 1994.
- [59] V.L. Colvin, A.N. Goldstein, A.P. Alivisatos. Semiconductor Nanocrystals Covalently Bound to Metal-Surfaces with Self-Assembled Monolayers. *J. Amer. Chem. Soc.*, 114:5221–5230, 1992.
- [60] P.-J. Wu, K.D. Tsuei, M.-T. Hsieh, K.-H. Wei, K.S. Liang. Dependence of the final-state effect on the coupling between a CdSe nanoparticle and its neighbors studied with photoemission spectroscopy. *Phys. Rev. B*, 75:115402, 2007.
- [61] J.J. Blackstock, Z. Li, M.R. Freeman, D.R. Stewart. Ultra-flat platinum surfaces from template-stripping of sputter deposited films. *Surface Science*, 546:87–96, 2003.
- [62] R.W. Meulenberg, J.R. Lee, A. Wolcott, J.Z. Zhang, L.J. Terminello, T. von Buuren. Determination of the Exciton Binding Energy in CdSe Quantum Dots. *ACS Nano*, 3:325–330, 2009.
- [63] J.-M. Caruge, J.E. Halpert, V. Wood, M.G. Bawendi, V. Bulović. Colloidal quantum-dot light-emitting diodes with metal-oxide charge transport layers. *Nature Photonics*, 2:247–250, 2008.
- [64] J.-M. Caruge, J.E. Halpert, V. Bulović, M.G. Bawendi. NiO as an inorganic hole-transporting layer in quantum-dot light-emitting devices. *Nano Lett.*, 6:2991–2994, 2006.
- [65] C.R. Kagan, C.B. Murray, M.G. Bawendi. Long-range resonance transfer of electronic excitations in close-packed CdSe quantum-dot solids. *Phys. Rev. B*, 54:8633, 1996.
- [66] C.A. Leatherdale, M.G. Bawendi. Observation of solvatochromism in CdSe colloidal quantum dots. *Phys. Rev. B*, 63:165315, 2001.

- [67] J.P. Keir, J.F. Wager. Electrical characterization of thin-film electroluminescent devices. *Annu. Rev. Mat. Sci.*, 27:223, 1997.
- [68] M. Dur, S.M. Goodnick, S.S. Pennathur, J.F. Wager, M. Reigrotzki, R. Redmer. High-field transport and electroluminescence in ZnS phosphor layers. *J. Appl. Phys.*, 83:3176, 1998.
- [69] Y. Ono. *Electroluminescent Displays*. World Scientific, 2005.
- [70] D. Li, B.L. Clark, D.A. Keszler, P. Keir, J.F. Wager. Color control in sulfide phosphors: Turning up the light for electroluminescent displays. *Chem. Mater.*, 12:268, 2000.
- [71] C. King. *Electroluminescent Displays*. Planar Systems, 2003.
- [72] E. Bringuier. Charge Transfer in ZnS-type electroluminescence. *J. Appl. Phys.*, 66:1314–1325, 1989.
- [73] D.J. Norris, A.L. Efros, S.C. Erwin. Doped Nanocrystals. *Science*, 319:1776–1779, 2008.
- [74] N. Pradhan, D. Goorskey, J. Thessing, X. Peng. An alternative of CdSe nanocrystal emitters: Pure and tunable impurity emissions in ZnSe nanocrystals. *J. Amer. Chem. Soc.*, 127:17586–17587, 2005.
- [75] N. Pradhan, X. Peng. Efficient and color-tunable Mn-doped ZnSe nanocrystal emitters: Control of optical performance via greener synthetic chemistry. *J. Amer. Chem. Soc.*, 129:3339–3347, 2007.
- [76] H. Yang, S. Santra, P.H. Holloway. Syntheses and applications of Mn-doped II-VI semiconductor nanocrystal. *J. Nanoscience and Nanotechnology*, 5:1364, 2005.
- [77] R. Thakar, Y. Chen, P. T. Snee. Efficient emission from core/(doped) shell nanoparticles: Applications for chemical sensing. *Nano Lett.*, 7:3429, 2007.

- [78] S. Kobayashi, Y. Tani, H. Kawazoe. Quantum Dot Activated All-inorganic Electroluminescent Device Fabricated Using Solution-Synthesized CdSe/ZnS Nanocrystals. *Jap. J. Appl. Phys.*, 46:L966–L969, 2007.
- [79] M. Böberl, M.V. Kovalenko, S. Gamerith, E.J.W. List, W. Heiss. Inkjet-printed nanocrystal photodetectors operating up to 3  $\mu\text{m}$  wavelengths. *Adv. Mat.*, 19:3574–3578, 2007.
- [80] R.D. Deegan, O. Bakajin, T.F. Dupont, G. Huber, S.R. Nagel, T.A. Witten. Capillary flow as the cause of ring stains from dried liquid drops . *Nature*, 389:827–829, 1997.
- [81] R.D. Deegan, O. Bakajin, T.F. Dupont, G. Huber, S.R. Nagel, T.A. Witten. Pattern formation in drying drops. *Phys. Rev. E*, 62:756–764, 2000.
- [82] E. Tekin, P.J. Smith, S. Hoepfener, A.M.J. van de Berg, A.S. Susa, A.L. Rogach, J. Feldmann, U.S. Schubert. Inkjet printing of luminescent CdTe nanocrystal-polymer composites. *Adv. Funct. Mat.*, 17:23–28, 2007.
- [83] R.M. Taylor, K.H. Church, M.I. Sluch. Red light emission from hybrid organic/inorganic quantum dot AC light emitting displays. *Displays*, 28:92–96, 2007.
- [84] J.A. Kong. *Electromagnetic Wave Theory*. EMW Publishing, 2000.
- [85] J.E. Halpert, V.J. Porter, J.P. Zimmer, M.G. Bawendi. Synthesis of CdSe/CdTe Nanobarells. *J. Amer. Chem. Soc.*, 128:12590–12591, 2006.
- [86] A.C. Arango, D.C. Oertel, Y. Xu, M.G. Bawendi, and V. Bulović. Heterojunction Photovoltaics Using Printed Colloidal Quantum Dots as a Photosensitive Layer. *Nano Lett.*, 9:860–863, 2009.
- [87] V.I. Klimov. *Semiconductor and Metal Nanocrystals*, chapter Charge Carrier Dynamics and Optical Gain in Nanocrystal Quantum Dots, pages 159–214. Marcel Dekker, 2004.

- [88] F. Garcia-Santamara, Y. Chen, J. Vela, R. D. Schaller, J. A. Hollingsworth, V. I. Klimov. Suppressed Auger Recombination in "Giant" Nanocrystals Boosts Optical Gain Performance. *Nano Lett.*, 9:3482–3488, 2009.